Applications and Development of Seismic Interferometry by Crosscorrelation and Multidimensional Deconvolution

Shohei Minato

相互相関型および多次元デコンボリューション型
地震波干渉法による地震波の再現とその応用

湊　翔平

Abstract

Seismic exploration and seismology has been developed to obtain the underground information of the earth. In these studies, many of the characteristics of the seismic wave are used to estimate the internal information of the medium. For example, seismic reflection or refraction response is employed to estimate the geological boundary and the propagating velocity. These studies use the theoretical relation of the wavefield with the specified source and receivers. Therefore we install dense source and receiver array (active seismic acquisition) or we observe the wavefield from naturally occurring sources (passive seismic acquisition). However, it is not always possible to install dense source and receiver array such as in the urban area. Furthermore, when we estimate the dynamic change of the underground, we must iteratively perform the seismic survey, which significantly increases the observation cost.

Seismic interferometry (SI) has a potential to overcome those limitations. SI is a technique to retrieve seismic wavefield from observed wavefield by using reciprocity theorem. SI creates new wavefield as if the source and receiver configuration is changed. Retrieving wavefield gives us the great advantages in the seismic acquisition. For example, since we can generate virtual source records, the passive seismic data can be converted into the active seismic data. Furthermore, since the retrieved wavefield has a different source-receiver configuration from original wavefield, the degree of freedom for the installation of sources is increased and the effect from complex structure such as weathering layers can be removed.

In this thesis, we apply the SI to the wide range of the field data to expand the applicability of SI. The field data ranges from the large scale crustal reflection, the dynamic change of the propagating velocity and the engineering scale borehole survey. Although the SI has many applications, it has been pointed out that the conventional crosscorrelation (CC) method has a limitation when the assumption of a homogeneous source distribution is violated. Since the local earthquakes used in this study violate this assumption, we must consider the improvement of the quality of retrieved wavefield. Furthermore, the SI based on the convolution-type reciprocity (MDD, multidimensional deconvolution) is proposed to overcome this problem. In this study, we apply the SI to the field data and discuss the improvement of retrieved wavefield. We show that choosing crosscorrelation traces by stationary-phase evaluation can be used to obtain high quality wavefield from local earthquakes. Furthermore, we introduce new solution method for the MDD method to discuss the source-receiver configuration and apply to crosswell reflection imaging.

We applied SI to Ocean Bottom Seismogram (OBS) records observing local earthquakes. SI is successfully applied to the teleseismic records to retrieve the large scale reflected waves such as the Moho reflections. On the other hand, the local earthquakes which have shorter raypath are expected to contain the higher frequency components and to detect more fine-scale structures by SI. However, such local earthquakes are usually inhomogeneously distributed. This violates the assumption of SI and the conventional SI processing (crosscorrelation and summation) yields to the deteriorated subsurface images. We used the stationary-phase interpretation to obtain the high-quality reflection imaging results under the localized source distribution. We estimated the raypath of two reflections events which are sea-surface P-wave reflection and sea-surface

multiple P-wave reflection. We show that choosing CC traces by stationary-phase evaluation improves the quality of the reflection from the upper oceanic crust boundary. This processing can be used to obtain higher-resolution reflection images under the insufficient source illumination.

We applied SI to ambient noise records. We show the feasibility for monitoring the dynamic change of the medium without controlled sources or natural earthquakes. We showed that the velocity of the crust changed during six months in the duration of the 2011 off the Pacific coast of Tohoku Earthquake in Japan. We retrieve scattered wave by autocorrelating ambient noise and track the small change of their waveform to obtain the dynamic change of the velocity in South Tohoku region. The velocity drop was observed corresponding to the Tohoku Earthquake and two after shocks with a large surface deformation. The change of the stress field or the change of the rock properties by strong motion is discussed for the cause of the velocity decrease. The spatial distribution of the velocity change shows a correlation to both the static strain change derived from GPS records and the spatial distribution of the peak particle velocity experienced during the earthquakes. The area which experienced compaction and strong motion showed velocity decrease. This result suggests that the velocity change of this study is affected by a strong motion at the near-surface, possibly corresponding to the damage to the near-surface rocks. On the other hand, the crossplot shows a correlation of velocity change to the strain change. These observations suggest that our velocity change also contains the deeper information possibly for the release of the enormous stress associated with the earthquakes.

SI by MDD which is based on a convolution-type reciprocity is an alternative method to the conventional CC method. Contrary to the CC method, MDD is valid for a dissipative medium and compensates for an irregular source distribution. Therefore the MDD method has a potential to retrieve higher-quality wavefield than the CC method. In this study , we discuss the effect of the source-receiver configuration for the MDD method. Since the MDD method includes inverse problem, there are several methods to achieve MDD. We first applied singular-value decomposition (SVD) for MDD and obtain the quantities representing the characteristics of the inverse problems. We show that the rank of kernel matrix of our inverse problem derived from SVD depends on the source-receiver configuration. This observation is crucial when we design the seismic experiments for MDD-based approach.

Furthermore, we applied SI by CC and MDD to the crosswell geometry. We retrieve a crosswell wavefield from a conventional VSP (vertical seismic profiling) data which is a wavefield in the borehole from a surface source. By starting from this source-receiver setting, we will have the advantages over conventional VSP processing and crosswell data, (1) the effects from the surface to the borehole receivers are removed, (2) the use of the surface sources significantly reduces the cost for crosswell survey which requires special borehole sources, and (3) the survey area can be expanded by using higher-energy surface sources. We introduce both SI by CC and MDD to retrieve crosswell wavefield using numerical modeling and field data. The retrieved images agree well with migrated data from a conventional crosswell seismic reflection survey and with P-wave velocities from well logs. The comparison of the retrieved reflected wavefields from the two methods with the reflected wavefields observed using borehole vibrators shows that both the MDD and CC methods retrieve up-going reflections very well, and the MDD method

retrieves down-going reflections with better amplitude preservation than the CC method. This indicates that the MDD method compensates for the effect of the irregular source distribution.

This study showed that the SI can retrieve various wavefield and subsurface information at relatively low cost. Furthermore, we discussed the practical problem for application of SI to the field data and high quality wavefield using new formulation of SI. One of the important feature of SI is to reduce the survey cost and the findings of the study are expected to contribute to the future application, especially for the monitoring technique.

要旨

石油や天然ガスなどの資源探査や地震防災などの分野では，地下構造に関する情報が必要不可欠である．地震学や物理探査学は媒質を伝播する波動場の様々な特徴を利用して地下構造の情報を推定する．例えば直接波や反射波，屈折波などは，地下の地質境界や伝播速度を推定することに利用される．こうした手法では，波動場を作り出す震源と，それを観測する受振点が必要であり，媒質の情報を推定するためにそれらの位置情報がしばしば用いられる．そのため，波動場を利用した地下構造推定には人工震源を利用した方法と，自然地震などの自然震源を利用した方法とに大別される．しかしながら前者は都市部などでは利用できる震源や密度に制約があり，モニタリングなどの繰り返し探査に多大なコストがかかる．一方後者は震源位置や発振時刻を事前に指定できないなどの制約を持つ．

地震波干渉法 (Seismic Interferometry, 以下 SI) を利用することにより，このような制約を解決できる可能性がある．SI とは相反定理に基づいて観測波動場から新しい波動場を抽出する手法であり，新しい波動場は新たな震源 – 受振点配置をもつ．この特徴により，例えば自然地震や常時微動などを観測するパッシヴデータはあたかも人工震源データのように扱うことができる．また，SI は震源配置が変化したデータを作り出すため，人工震源の設置個所の自由度が増加することや，伝播経路の変化によって SI を利用しない場合に比べて表層付近の風化層などの複雑な構造の影響を取り除くことができるなどの利点を持つ．本研究では SI の適用範囲を広げるために，様々なフィールドデータに対して SI を適用する．具体的には自然地震を利用した海洋地殻境界からの反射波の抽出，常時微動を利用した地下構造のモニタリング，および 2 つの坑井を利用した地下構造イメージングへ SI を適用する．SI は既に幅広く利用されているが，しばしば SI を適用する波動場に関する仮定が十分に満たされない場合が存在することが知られている．相互相関型相反定理に基づく SI においては，元となる波動場に震源が均質に分布する必要がある．しかしながら近地地震を利用する場合にはこの仮定が満たされないことが多く，精度よく目的の波動場を抽出するためには SI を改良する必要がある．さらに根本的に SI を改良するために，畳み込み積分型相反定理に基づく SI(多次元デコンボリューション, 以下 MDD) が新たに提案されている．本研究では様々なフィールドデータに対して SI を適用するとともに，SI を改良するための議論を行う．具体的には近地地震に対して停留位相の概念を利用して相互相関を行うトレースを選択することで目的の波動場を精度よく求める．また新しい SI である MDD に対して，新たな逆解析解法を導入することで震源 – 受振点配置の問題を議論し，また初めて 2 つの坑井を利用した地下構造イメージングへ適用する．

まず，相互相関型の SI を，南海トラフ域で近地地震を観測した OBS(海底地震計) データへ適用した．遠地地震を利用した SI はモホ面などの比較的大きな地質スケールをイメージングすることに成功している．一方で，高周波成分を含む近地地震を利用することで，より詳細な地下構造をイメージングできる可能性がある．しかしながら近地地震は OBS 配置に対して発生個所が偏在しているため，通常の処理による SI では目的の波動場が精度良く求まらない．そこで，相互相関型の SI を停留位相近似して得られる物理的解釈を利用する．具体的には，近地地震記録から反射波を抽出するとき，２つのイベント（本研究では海面反射 P 波と海面多重反射 P 波）が相互相関処理する一方の受振点へ到達するまで同一の伝播経路をもつときに限り目的の反射波を抽出することができる．震源位置から 2 つのイベントの伝播経路を推定することで，停留位相となることが推定される特定の

組み合わせの相互相関トレースのみを地下構造イメージングに利用する．これにより震源が偏在している条件のもとで，精度よく自然地震記録から反射境界構造をイメージングした．自然地震を模擬した数値計算と，南海トラフに設置された OBS データを用い，海洋地殻上面の反射境界をイメージングすることに成功した．この方法により震源偏在のもとで SI を利用できる可能性を示した．

次に常時微動を観測したデータに対して SI を適用した．常時微動を利用することで人工震源や自然地震を利用せずに媒質の変化をモニタリングできる．2011 年 3 月に東北沖で発生した Mw9.0 の地震 (2011 年東北地方太平洋沖地震) によって地殻の伝播速度が変化した可能性を SI によって示した．地震に伴う媒質変化は，人工震源や自然地震を利用した調査によって数多く研究されており，常時微動に SI を利用して地震にともなう変化を観測する事例は既にいくつか報告されているが，今後さらに多くなると予測される．Hi-net による振動観測網を用い，SI(自己相関) によって散乱波を抽出した．さらにその波形の時系列変化を推定することで，東北地方南部において，2011 年東北地方太平洋沖地震を含む 6ヶ月間の媒質の伝播速度の変化を推定した．この結果，東北沖地震と，大きな地表変動を伴う 2 つの余震に対応して，地殻の速度が低下する現象が確認された．これらを説明する理由として，地震に伴う応力変化と，地震動に伴う地表付近の地殻の速度変化（例えばクラックの増加）を議論した．GPS から推定した調査域の面積ひずみの変化と，Kik-net 観測網から推定した地表付近の強振粒子速度の分布を，SI によって推定した速度低下と比較した．圧縮を受け，大きな地震動を受けた地域が速度低下を示したことから，推定された速度低下は地震動に伴う地表付近の岩石の変化に影響されていることが推測された．一方で速度低下は面積ひずみ変化に対して相関を示したことから，推定された速度変化は，地表付近の岩石の速度低下と，応力解放に伴う深部の速度変化の両者の影響を含んでいると考えられる．

これまで一般的だった相互相関型の SI に変わり，新たに畳み込み積分型相反定理に基づく MDD が提案されている．MDD は従来の SI と異なり，減衰媒質で有効であり，震源の偏りを補正する．そのため特定の条件では従来の SI よりも高精度に目的の波動場を抽出できる可能性がある．本研究では MDD を適用するにあたり，震源の配置が MDD にどのように影響するか議論した．MDD は逆問題を解く手順を含むため，逆問題解法の種類によりバリエーションが考えられる．本研究では MDD の逆問題解法に初めて特異値分解 (SVD) を利用した．これに伴い，MDD の逆問題を評価できる量が SVD により得られる．本研究では SVD で得られたカーネル行列のランクが震源配置に依存することを示した．これにより，MDD を利用した実験において，事前にどのような震源配置が適切であるかを評価することができる．

さらに従来の SI，および MDD を，2 つの坑井を利用した地下構造イメージング (坑井間反射法) へ適用した．地表震源・坑内受振のデータ (VSP データ) を用いて坑井間の波動場を抽出することで，(1) 地表から坑内受振点までの速度構造を利用せずに坑井間の地質構造を推定できる,(2) 地表震源に高エネルギー震源を利用することで従来よりも探査範囲 (坑井間距離) を広げることができる,(3) 坑内震源を利用しないので調査コストが比較的低い, といった利点をもつ．また，特に MDD を坑井間波動場に適用した事例は本研究が初めてである．数値計算，およびフィールドデータを用いて VSP データから坑井間波動場を抽出し，地下構造をイメージングした．この結果，従来の SI および MDD はどちらも良

く坑井間の地下構造をイメージングした．一方で推定された坑井間波動場を比較すると，MDD は従来の SI よりも，特に下方反射波の振幅を精度良く抽出した．これは MDD が震源の偏在を補正する効果を持っていることを表している．

本研究では様々なフィールドデータに対して SI を適用することで，SI によって種々の地下情報が比較的低コストで得られることを示した．また，SI を適用するにあたって伴う問題点とその解決法の提案，および新しい SI による波動場推定の高精度化について議論した．SI の重要な特徴の１つは調査コストの低下であり，ここで得られた知見は今後，特にモニタリング技術への応用が期待される．

Contents

List of Figures

1 Introduction

1.1 Advantages of retrieval of seismic response

For oil/gas exploration and hazard mitigation, the underground information of the earth must be required. Seismic exploration and seismology has been developed to achieve this purpose. In these studies, many of the characteristics of the seismic wave are used to obtain the internal information of the medium. For example, seismic reflection or refraction response is employed to detect the geological boundary and estimate the propagating velocity. These studies use the theoretical relation of the wavefield with the specified source and receivers. Therefore we install dense source and receiver array (active seismic acquisition) or observe wavefield from naturally occurring sources (passive seismic acquisition).

However, it is not always possible to install dense source and receiver array such as in the urban area. Furthermore, when we estimate the dynamic change of the underground, we must iteratively perform the seismic survey, which significantly increases the observation cost.

Seismic interferometry is a technique to retrieve seismic wavefield from observed wavefield. Here we refer to 'retrieve' as we create new wavefield as if we change the source and receiver configuration based on a wave equation. For example, when we observe the wavefield using multiple receivers from a physical source, we can create a new wavefield as if the source position is specified at each of the receivers. We call this receiver position as 'virtual source' position since the wave is generated from this virtual source in the retrieved wavefield.

Retrieving wavefield gives us the great advantages in the seismic acquisition. For example, since we can generate virtual source records, the passive seismic data can be converted into the active seismic data. This indicates the possibility to perform the active seismic survey in the urban area and to monitor the dynamic change of the medium without using active sources. It is also useful for the active seismic survey. The retrieved wavefield has the different source position from the original wavefield. The vertical seismic profiling (VSP) data from surface sources are affected by the obstacles at near surface. By retrieving wavefield with the virtual source position in the borehole, such effect of the obstacles can be removed without any knowledge of the near surface and the higher resolution images are obtained. Retrieving surface wave is also employed to estimate and remove the surface waves. Furthermore, estimating multiple reflect waves and removing them has also similar basis of this technique.

1.2 Seismic Interferometry and New formulation

Seismic Interferometry (SI) can be defined as a process of generating new seismic data from the crosscorrelation of the wavefields. The possibility of this technique was first proposed by Claerbout (1968). He introduced that the reflection response of horizontally layered media can be retrieved from autocorrelation of the transmission responses. He called this technique as "Acoustic Daylight Imaging". Around the turn of the century, the literature of Interferometric techniques has grown spectacularly by several authors (Wapenaar, 2004; Wapenaar and Fokkema, 2006; Schuster et al., 2004; Snieder, 2004; Bakulin and Calvert, 2006). These theories use a crosscorrelation of the existing records.

SI is explained by the reciprocity theorem. A reciprocity theorem formulates the reciprocal relations between two wavefield with two independent conditions. The conventional SI by cross-correlation (CC) uses the correlation-type reciprocity. In this SI, we assume that the medium is lossless and the source distribution is homogeneous so that the integral is operated along the source position after crosscorrelation operation.

Recently, SI derived from the different type of the reciprocity was proposed. It is called multidimensional deconvolution (MDD) and uses the convolution-type reciprocity. Since we use the different assumptions to derive SI by MDD, it has different characteristics from SI by CC. For example, MDD compensates for the irregular source distribution and available for the dissipative medium. SI by MDD has several successful applications, for example, virtual source method (van der Neut et al., 2010), crosswell geometry (Minato et al., 2011), EM survey (Wapenaar et al., 2008a) and the surface wave retrieval (Wapenaar et al., 2010).

1.3 Outline of this thesis

In this thesis, we apply the SI to the wide range of the field data to expand the applicability of SI. The field data ranges from the large scale crustal reflection, the dynamic change of the propagating velocity and the engineering scale borehole survey. Furthermore, we improve the quality of the retrieved wavefield by introducing stationary phase approximation and recently proposed MDD method. We also investigate the effect of the source-receiver configuration for the MDD method to obtain the useful information of the survey design.

Chapter 2 gives the theory for SI. We show the two types of the reciprocity equations; correlation-type and convolution-type reciprocity. Since the reciprocity theorem contains the wavefield for both monopole and dipole sources, we approximate those relations so that it can be used to the actual applications. The approximated wavefield representation of the correlation-type reciprocity results in the SI by CC and that of the convolution-type reciprocity results in the SI by MDD.

Chapter 3 applies SI by CC to Ocean Bottom Seismogram (OBS) record which observe local earthquakes at Nankai trough. Retrieving reflection response from passive records has a great advantages for the monitoring structures. We try to use local earthquakes to retrieve reflection response. Since the local earthquakes contain higher frequencies it is expected to produce

higher-resolution images. However, insufficient illumination from sources violates the assumption of SI by CC. To overcome this, we try to use a stationary phase approximation. A calculated raypath is used to evaluate stationary phase pair of crosscorrelation traces. This procedure may be used to obtain higher-resolution reflection images under the insufficient source illumination.

Chapter 4 applies autocorrelation analysis to monitor the velocity change due to the earthquakes. The another possibility for monitoring by SI is to use the ambient noise since they are continuously observed. Retrieving scattered wave by correlating ambient noise and tracking the small perturbation of their waveform gives the dynamic change of the velocity of the medium. The earthquakes may cause the velocity change due to the change of the stress field or the change of the rock properties by strong motion. We used the Hi-net continuously recording data to detect the temporal change of the velocity. We analyzed the 6-month long data and obtained velocity change caused by the 2011 off the Pacific coast of Tohoku Earthquake and its aftershocks.

Chapter 5 investigates the inverse problem of MDD. SI by MDD is an alternative method to the conventional CC method. SI by MDD is superior to the CC method in several characteristics and its application is expanding. The source illumination is a most important factor for the application of SI. The source-receiver setting in the original wavefield dominates the amount of useful information for retrieval of desired wavefield. Therefore, evaluation of source illumination is crucial for the survey design of SI. The stationary phase approximation is a useful method for the conventional SI by CC. However, the method for SI by MDD has not been established. Therefore, we introduced the singular-value decomposition (SVD) to achieve MDD. Introducing SVD gives us the analytic method to evaluate the source-receiver settings by using quantities representing the characteristics of the inverse problems. We show the relation of the quantities derived from SVD and the source-receiver configuration.

Chapter 6 applies SI to the crosswell geometry. We retrieve a crosswell wavefield from a conventional VSP (vertical seismic profiling data) data which is the wavefield in the borehole from surface sources. By starting from this source-receiver setting, we will have the advantages over conventional VSP processing and crosswell data. For example, the effects from the surface to the borehole receivers are removed and higher-resolution images are obtained, the use of the surface sources significantly reduce the cost for crosswell survey which requires special borehole sources, and the survey area can be expanded by using higher-energy surface sources. We introduce both SI by CC and MDD to retrieve crosswell wavefield using numerical modeling and field data. We compare the result from SI by CC and MDD.

Chapter 7 gives summary and conclusions of various applications of SI. It also gives future prospects of the study.

2 Theory of Seismic Interferometry

2.1 Introduction

Seismic Interferometry (SI) refers to a series of processing to retrieve new seismic response from observed wavefield. This theory has been proven using various basis depending on the specific applications. In this thesis, we derive the relations for SI by a reciprocity theorem. A reciprocity theorem formulates the reciprocal relations between two wavefield with two independent conditions. The relation is appeared as a multiplication of two quantities in the frequency domain. Therefore this is corresponding to a time-convolution or time-correlation of the wavefield. We derive two types of the reciprocal relations from two-way wave equation, namely correlation-type reciprocity and convolution-type reciprocity by giving different configurations and assumptions. A correlation-type reciprocity is a basis of SI by crosscorrelation and a convolution-type reciprocity is a basis of SI by multidimensional deconvolution. By modifying and simplifying the reciprocal relations to be adaptable for actual experiment, we obtain the relations of SI for different formulations. We derive these relations by considering scalar wavefield or acoustic wavefield.

2.2 Reciprocity Theorems

We consider an arbitrary inhomogeneous 3D (dissipative or lossless) acoustic media in a domain $\mathbb{V}$ whose surface is defined as $\mathbb{S}$ (Figure 2.1). We define two states which have different medium quantities, source positions and boundary conditions. Integral of the "interaction quantity" followed by theorem of Gauss yields to a reciprocal relation between two states. We derive two types of reciprocity relations, correlation-type and convolution-type, by considering different assumptions.

We start from the equation of motion and the stress-strain relation,

$$j\omega\rho\hat{v}_i + \partial_i\hat{p} = \hat{f}_i, \tag{2.1}$$

$$j\omega\kappa\hat{p} + \partial_i\hat{v}_i = \hat{q}, \tag{2.2}$$

where Einstein's summation convention is applied for repeated lowercase subscripts. ∂_i is a partial derivative in the x_i direction. $\hat{p}$ is a acoustic pressure, $\hat{\mathbf{v}} = (\hat{v}_1, \hat{v}_2, \hat{v}_3)$ a particle velocity, $\rho(\mathbf{x})$ a mass density distribution of the medium, $\kappa(\mathbf{x})$ its compressibility, $\hat{\mathbf{f}} = (\hat{f}_1, \hat{f}_2, \hat{f}_3)$ a external volume force density, and $\hat{q}$ a volume injection rate respectively. The subscript $\hat{}$ denotes the

quantities are defined in the space-frequency domain. Now we define "interaction quantity" as follows,

$$\partial_i\{\hat{p}_A\hat{v}_{i,B} - \hat{v}_{i,A}\hat{p}_B\}, \tag{2.3}$$

where the subscripts A and B denote the two independent acoustic states which may have different medium parameters. Integrating equation 2.3 over the boundary $\mathbb{S}$ with the outward pointing normal vector $\mathbf{n} = (n_1, n_2, n_3)$ yields,

$$\oint_{\mathbb{S}}\{\hat{p}_A\hat{v}_{i,B} - \hat{v}_{i,A}\hat{p}_B\}n_i d^2\mathbf{x} = \int_{\mathbb{D}}\{\hat{p}_A\hat{q}_B - \hat{v}_{i,A}\hat{f}_{i,B} - \hat{q}_A\hat{p}_B + \hat{f}_{i,A}\hat{v}_{i,B}\}d^3\mathbf{x}, \tag{2.4}$$

where the theorem of Gauss was applied. This relation formulates the connection between two independent states A and B by multiplication of the quantities in frequency domain. Therefore, we call this relation as wave field reciprocity of convolution-type. If we ignore the external force $\hat{\mathbf{f}}$ we have,

$$\oint_{\mathbb{S}}\{\hat{p}_A\hat{v}_{i,B} - \hat{v}_{i,A}\hat{p}_B\}n_i d^2\mathbf{x} = \int_{\mathbb{D}}\{\hat{p}_A\hat{q}_B - \hat{q}_A\hat{p}_B\}d^3\mathbf{x}. \tag{2.5}$$

Secondary, we assume time-reversal invariance for lossless medium. A time-reversed function in space-frequency domain is represented as a complex conjugated function. When the source quantities are described as $\hat{\mathbf{f}}$ and $\hat{q}$, its solutions for the equation of motion and the stress-strain relation yield to $\hat{p}$ and $\hat{\mathbf{v}}$. For time-reversal invariance, $\hat{p}^*$ and $-\hat{\mathbf{v}}^*$ obey same equations with the source quantities of $\hat{\mathbf{f}}^*$ and $-\hat{q}^*$. In this case, the reciprocal relation of equation 2.4 is written as,

$$\oint_{\mathbb{S}}\{\hat{p}^*_A\hat{v}_{i,B} + \hat{v}^*_{i,A}\hat{p}_B\}n_i d^2\mathbf{x} = \int_{\mathbb{D}}\{\hat{p}^*_A\hat{q}_B + \hat{v}^*_{i,A}\hat{f}_{i,B} + \hat{q}^*_A\hat{p}_B + \hat{f}^*_{i,A}\hat{v}_{i,B}\}d^3\mathbf{x}. \tag{2.6}$$

A multiplication of complex-conjugated function corresponds to a crosscorrelation in time domain. Therefore we call this reciprocal relation as wave field reciprocity of correlation-type. Similar to convolution-type reciprocity, we ignore the external force and obtain,

$$\oint_{\mathbb{S}}\{\hat{p}^*_A\hat{v}_{i,B} + \hat{v}^*_{i,A}\hat{p}_B\}n_i d^2\mathbf{x} = \int_{\mathbb{D}}\{\hat{p}^*_A\hat{q}_B + \hat{q}^*_A\hat{p}_B\}d^3\mathbf{x}. \tag{2.7}$$

Note that the convolution-type reciprocity (equation 2.4 and 2.5) holds for inhomogeneous dissipative medium. On the other hand, the correlation-type reciprocity (equation 2.6 and 2.7) is only valid for inhomogeneous lossless medium.

2.3 Seismic Interferometry by Crosscorrelation Method

2.3.1 Correlation-type Green's function representation

The SI by crosscorrelation (CC) is derived from the reciprocity of correlation type (equation 2.7). We consider two different state A and B. These states are distinguished as "actual state" and "reference state". These two states may have different medium parameters and/or

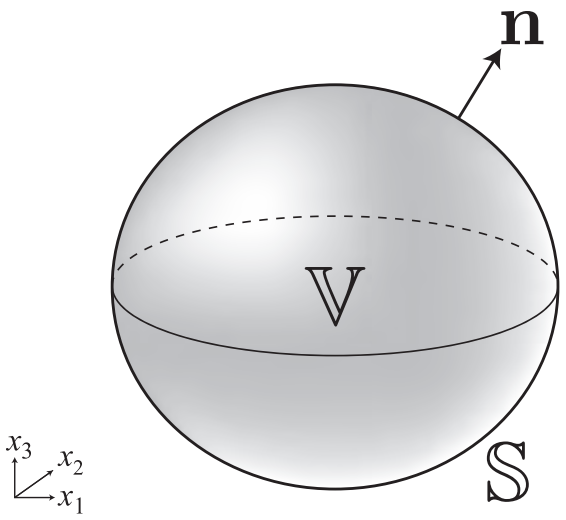

Figure. 2.1: An arbitrary inhomogeneous 3D (dissipative or lossless) acoustic media in a domain $\mathbb{V}$ whose surface is defined as $\mathbb{S}$. **n** is an outward pointing normal vector.

boundary conditions. Here we consider inhomogeneous lossless medium which has the identical medium parameters inside $\mathbb{V}$ for these two states. For both state, we put the impulsive source at inside $\mathbb{V}$.

$$\hat{q}_A(\mathbf{x},\omega) = \delta(\mathbf{x}-\mathbf{x}_A), \tag{2.8}$$

$$\hat{q}_B(\mathbf{x},\omega) = \delta(\mathbf{x}-\mathbf{x}_B), \tag{2.9}$$

where $\mathbf{x}_A$ and $\mathbf{x}_B$ indicate the source position for two states (Figure 2.2(a) and 2.2(b)). The wavefield for these impulsive sources are described as follows.

$$\hat{p}_A(\mathbf{x},\omega) = \hat{G}(\mathbf{x},\mathbf{x}_A,\omega), \tag{2.10}$$

$$\hat{v}_{i,A}(\mathbf{x},\omega) = -\frac{1}{j\omega\rho_A(\mathbf{x})}\partial_i\hat{G}(\mathbf{x},\mathbf{x}_A,\omega), \tag{2.11}$$

$$\hat{p}_B(\mathbf{x},\omega) = \hat{\tilde{G}}(\mathbf{x},\mathbf{x}_B,\omega), \tag{2.12}$$

$$\hat{v}_{i,B}(\mathbf{x},\omega) = -\frac{1}{j\omega\rho_B(\mathbf{x})}\partial_i\hat{\tilde{G}}(\mathbf{x},\mathbf{x}_B,\omega), \tag{2.13}$$

where $\hat{G}(\mathbf{x},\mathbf{x}_{A(B)},\omega)$ or $\hat{\tilde{G}}(\mathbf{x},\mathbf{x}_{A(B)},\omega)$ indicates the Green's function observed at $\mathbf{x}$ from the source at $\mathbf{x}_{A(B)}$. We introduced the notation $\hat{\tilde{G}}$ in addition to $\hat{G}$ in order to distinguish the wavefield for different conditions which have different medium parameters and/or boundary conditions. We substitute equation 2.10 to equation 2.13 into the reciprocity of correlation type (equation 2.7) and we obtain,

$$\begin{aligned}\hat{\tilde{G}}(\mathbf{x}_B,\mathbf{x}_A,\omega) + \hat{G}^*(\mathbf{x}_B,\mathbf{x}_A,\omega) &= -\oint_{\mathbb{S}}\frac{1}{j\omega\rho(\mathbf{x})}\Big(\partial_i\hat{\tilde{G}}(\mathbf{x}_B,\mathbf{x},\omega)\hat{G}^*(\mathbf{x}_A,\mathbf{x},\omega)\\ &\quad -\hat{\tilde{G}}(\mathbf{x}_B,\mathbf{x},\omega)\partial_i\hat{G}^*(\mathbf{x}_A,\mathbf{x},\omega)\Big)n_i d^2\mathbf{x},\end{aligned} \tag{2.14}$$

where we applied the source-receiver reciprocity (see Appendix). We rewrite the density distribution $\rho_{A(B)}(\mathbf{x})$ as $\rho(\mathbf{x})$ since they are defined to be identical inside the integral domain $\mathbb{V}$ and along the surface $\mathbb{S}$. Equation 2.14 indicates that integrating the products of the Green's function from the monopole and dipole sources over the boundary $\mathbb{S}$ produces causal and acausal part of the Green's function between $\mathbf{x}_A$ and $\mathbf{x}_B$. This equation is exact in any arbitrary inhomogeneous lossless media. This is the crosscorrelation-type Green's function representation and starting point for SI by crosscorrelation method.

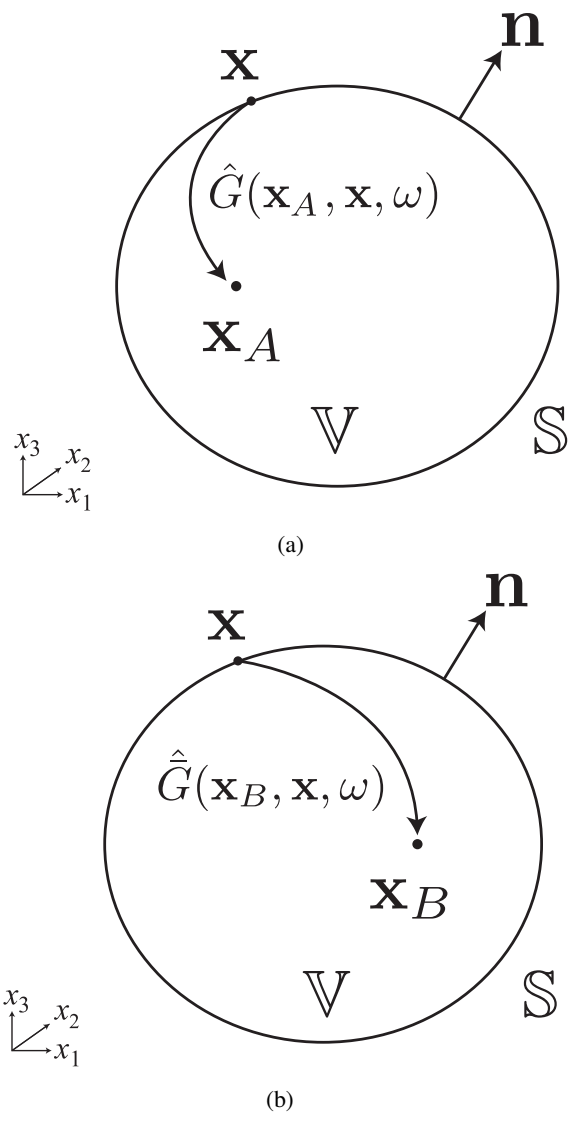

Figure. 2.2: Configuration for Correlation-type Green's function representation. (a) Impulsive source at $\mathbf{x}_A$ for actual state (state-A). (b) Impulsive source at $\mathbf{x}_B$ for reference state (state-B). $\hat{G}$ or $\hat{\hat{G}}$ indicates Green's function.

2.3.2 Simplification of the integral

In the field experiment it is usually difficult to obtain the spatial derivatives of the Green's function or the Green's function for two types of the sources. We consider the simplified form of the integral of the correlation-type Green's function representation (equation 2.14).

The source position $\mathbf{x}$ in the integrand of equation 2.14 is specified along the surface $\mathbb{S}$. We assume that the medium at and outside $\mathbb{S}$ is homogeneous for both state of A and B. Therefore, there is no difference between the wavefield for state A (actual state) and state B (reference state) and we rewrite $\hat{\tilde{G}}$ for reference state as $\hat{G}$.

We introduce far-field approximation. We assume that the observed point $\mathbf{x}_{A(B)}$ is located within the scattering body and the source position $\mathbf{x} \in \mathbb{S}$ is far from the scattering region. An incident wave will generate scattered radiation from the scattering body which can be represented as,

$$\hat{G}(\mathbf{x}_B, \mathbf{x}, \omega) \approx m(\phi, \theta)\frac{e^{-jkr}}{r}, \tag{2.15}$$

where k is a wave number and r is a length of vector $\mathbf{r}$ pointing from a point $\mathbf{x}_B$ to the source point $\mathbf{x}$ far from the scatterer such that $kr \gg 1$. $m(\phi, \theta)$ is a function of the angular coordinates only. In this case, the spatial derivatives in equation 2.14 become in the far-field approximation,

$$\begin{aligned} \sum_i n_i \partial_i \hat{G}(\mathbf{x}_B, \mathbf{x}, \omega) &\approx \frac{\partial \hat{G}}{\partial r} && (2.16)\\ &= -jk\hat{G} - \frac{\hat{G}}{r} && (2.17)\\ &\approx -jk\hat{G}. && (2.18) \end{aligned}$$

u Similarly, a complex-conjugated Green's function for $\mathbf{x}_A$ obeys,

$$\sum_i n_i \partial_i \hat{G}^*(\mathbf{x}_A, \mathbf{x}, \omega) \approx jk\hat{G}. \tag{2.19}$$

Substituting above approximations into equation 2.14 yields the far-field expression of Green's function representation,

$$\hat{G}(\mathbf{x}_B, \mathbf{x}_A, \omega) + \hat{G}^*(\mathbf{x}_B, \mathbf{x}_A, \omega) = \frac{2k}{\omega\rho}\oint\!\!\!\!\!\!\int_{\mathbb{S}_{src}} \hat{G}(\mathbf{x}_B, \mathbf{x}_S, \omega)\hat{G}^*(\mathbf{x}_A, \mathbf{x}_S, \omega) d^2\mathbf{x}_S. \tag{2.20}$$

This is the correlation-type Green's function representation with far-field approximation. We rewrite the notation $\mathbf{x}$ to $\mathbf{x}_S$ in order to explicitly express that we calculate integral of the cross-correlated wavefield from the sources along the closed surface $\mathbf{S}_{src}$. Equation 2.20 states that crosscorreating and integrating wavefield from sources along the closed surface yield to the Green's function between the two points (Figure 2.3). Note that the integral $\oint_{\mathbb{S}}$ can be exchanged as $\int_{\mathbb{S}_0}$ where $\mathbb{S}_0$ is a plane with the infinite length considering the sphere $\mathbb{V}$ with the infinite radius (Sommerfeld condition). This relation is used for SI by CC method and later section.

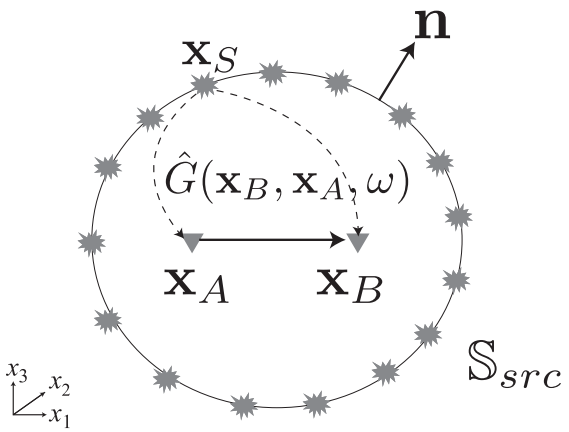

Figure. 2.3: Configuration for SI by CC. Objective function $\hat{G}(\mathbf{x}_B, \mathbf{x}_A, \omega)$ is obtained by the integral along the source surface.

2.4 Seismic Interferometry by Multidimensional Deconvolution Method

2.4.1 Convolution-type Green's function representation

The equation for SI by MDD is derived from the convolution-type reciprocity (Equation 2.5). We assume arbitrary inhomogeneous dissipative/lossless medium. We modify the configuration from that of the CC method so that the point source $\mathbf{x}_A$ (state A, actual state) is located outside $\mathbb{S}$ and $\mathbf{x}_B$ inside $\mathbb{V}$ (Figure 2.4(a) and 2.4(b)). We substitute the wavefield quantities (Equations 2.10 to 2.13) into the convolution-type reciprocity (Equation 2.5) and obtain,

$$\begin{aligned}\hat{G}(\mathbf{x}_B, \mathbf{x}_A, \omega) \quad = \quad & -\oint_{\mathbb{S}} \frac{1}{j\omega\rho(\mathbf{x})} \Big(\partial_i \hat{\tilde{G}}(\mathbf{x}_B, \mathbf{x}, \omega)\hat{G}(\mathbf{x}, \mathbf{x}_A, \omega) \\ & -\hat{\tilde{G}}(\mathbf{x}_B, \mathbf{x}, \omega)\partial_i \hat{G}(\mathbf{x}, \mathbf{x}_A, \omega)\Big) n_i d^2\mathbf{x}. \end{aligned} \tag{2.21}$$

This is the convolution-type Green's function representation and starting point of SI by MDD method.

2.4.2 Simplification of the integral

We approximate the two terms in the integral of equation 2.21 into single term using far-field approximation. We introduce the assumption that the medium for state B (reference state) is homogeneous at and outside $\mathbb{S}$. This leads to the wavefield $\hat{\tilde{G}}(\mathbf{x}, \mathbf{x}_B, \omega)$ containing only outward propagating wave from $\mathbb{S}$.

$$\hat{\tilde{G}}(\mathbf{x}, \mathbf{x}_B, \omega) = \hat{\tilde{G}}^{out}(\mathbf{x}, \mathbf{x}_B, \omega) \approx m(\phi, \theta)\frac{e^{-jkr}}{r}, \tag{2.22}$$

$$n_i \partial_i \hat{\tilde{G}} \approx -jk\hat{\tilde{G}}. \tag{2.23}$$

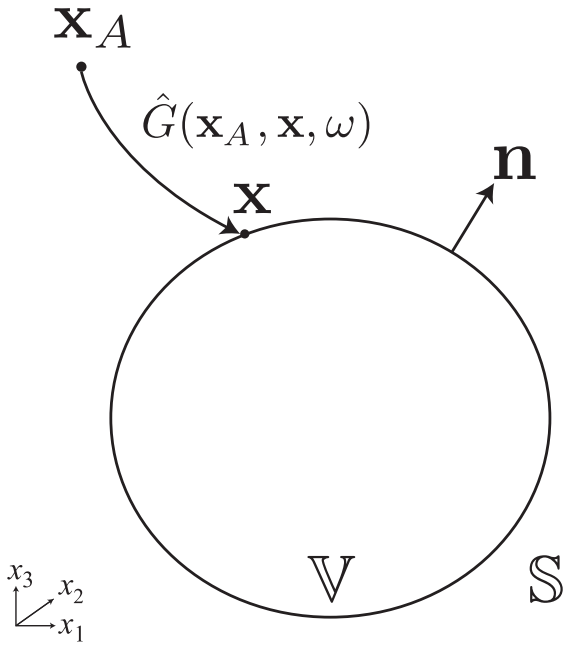

(a)

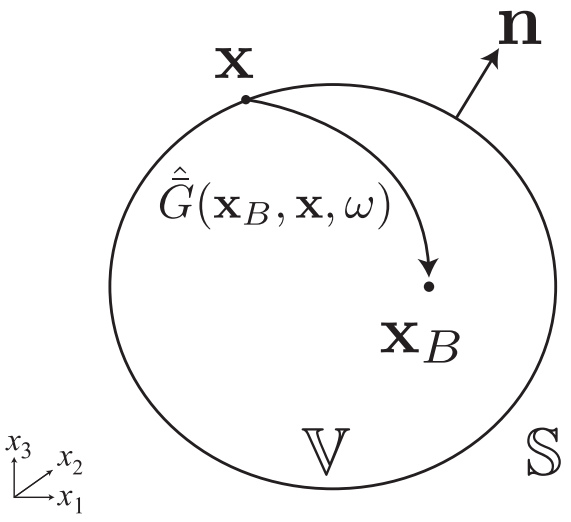

(b)

Figure. 2.4: Configuration for Convolution-type Green's function representation. (a) Impulsive source at $\mathbf{x}_A$ outside $\mathbb{S}$ for actual state (state-A). (b) Impulsive source at $\mathbf{x}_B$ inside $\mathbb{S}$ for reference state (state-B).

where we applied far-field approximation and r is again a length of vector $\mathbf{r}$ pointing from a point $\mathbf{x}_A$ to $\mathbf{x}$. The arbitrary inhomogeneity is assumed for state A (actual state) and we separate wavefield $\hat{G}(\mathbf{x}, \mathbf{x}_A, \omega)$ into inward- and outward-propagating part as,

$$\hat{G}^{in/out} \approx m^{in/out}(\phi, \theta)\frac{e^{\mp jkr}}{r}, \tag{2.24}$$

We rewrite the convolution-type Green's function representation (equation 2.21) by $\hat{G}^{in/out}$ as,

$$\begin{aligned}
\hat{G}(\mathbf{x}_B, \mathbf{x}_A, \omega) &= -\oint_{\mathbb{S}} \frac{1}{j\omega\rho(\mathbf{x})}\left(\partial_i\hat{\bar{G}}(\hat{G}^{in} + \hat{G}^{out}) - \hat{\bar{G}}\partial_i(\hat{G}^{in} + \hat{G}^{out})\right) d^2\mathbb{S} && (2.25)\\
&= -\oint_{\mathbb{S}} \frac{1}{j\omega\rho(\mathbf{x})}\left(\left(\partial_i\hat{\bar{G}}\hat{G}^{out} - \hat{\bar{G}}\partial_i\hat{G}^{out}\right)n_i + \right.\\
&\qquad \left.\left(\partial_i\hat{\bar{G}}\hat{G}^{in} - \hat{\bar{G}}\partial_i\hat{G}^{in}\right)n_i\right) d^2\mathbf{x}. && (2.26)
\end{aligned}$$

Similar to the derivation of the CC method, the operation $n_i\partial_i\hat{G}^{in/out}$ can be replaced as,

$$\begin{aligned}
n_i\partial_i\hat{G}^{in} &\approx jk\hat{G}^{in}, && (2.27)\\
n_i\partial_i\hat{G}^{out} &\approx -jk\hat{G}^{out}. && (2.28)
\end{aligned}$$

Note that sign accounts for the opposite pointing vector between $\mathbf{r}$ and $\mathbf{n}$. The first term of 2.26 reduces to zero and the two components of the second term have same value with opposite sign.

$$\begin{aligned}
n_i\partial_i\hat{\bar{G}}\hat{G}^{out} - \hat{\bar{G}}n_i\partial_i\hat{G}^{out} &= (-jk\hat{\bar{G}})\hat{G}^{out} - \hat{\bar{G}}(-jk\hat{G}^{out}) = 0 && (2.29)\\
n_i\partial_i\hat{\bar{G}}\hat{G}^{in} - \hat{\bar{G}}n_i\partial_i\hat{G}^{in} &= (-jk\hat{\bar{G}})\hat{G}^{in} - \hat{\bar{G}}(-jk\hat{G}^{in}) = -2jk\hat{\bar{G}}\hat{G}^{in} && (2.30)
\end{aligned}$$

We obtain the convolution-type Green's function representation assuming constant ρ along $\mathbb{S}$ as,

$$\hat{G}(\mathbf{x}_B, \mathbf{x}_A, \omega) = -\frac{1}{j\omega\rho}\oint_{\mathbb{S}}(-2jk\hat{\bar{G}}(\mathbf{x}_B, \mathbf{x}, \omega))\hat{G}^{in}(\mathbf{x}, \mathbf{x}_A, \omega)d^2\mathbf{x}, \tag{2.31}$$

Rewriting $\mathbf{x}_A$ as $\mathbf{x}_S$ indicating source position, $\mathbb{S}$ as $\mathbb{S}_{rec}$ and we obtain,

$$\hat{G}(\mathbf{x}_B, \mathbf{x}_S, \omega) = \oint_{\mathbb{S}_{rec}} \hat{\bar{G}}_d(\mathbf{x}_B, \mathbf{x}, \omega)\hat{G}^{in}(\mathbf{x}, \mathbf{x}_S)d^2\mathbf{x}. \tag{2.32}$$

$\hat{\bar{G}}_d(\mathbf{x}_B, \mathbf{x}, \omega)$ corresponds to the wavefield in the reference state (state B) as,

$$\begin{aligned}
\hat{\bar{G}}_d(\mathbf{x}_B, \mathbf{x}, \omega) &= -\frac{2}{j\omega\rho}(-jk\hat{\bar{G}}(\mathbf{x}_B, \mathbf{x}, \omega)) && (2.33)\\
&= -\frac{2}{j\omega\rho}n_i\partial_i\hat{\bar{G}}(\mathbf{x}_B, \mathbf{x}, \omega). && (2.34)
\end{aligned}$$

Equation 2.32 is the convolution-type Green's function representation with the far-field approximation. It states that the multiplication of inward-propagating wavefield in the actual state (state A) and the wavefield in the reference state (state B) and integrating along the receiver position in the actual state yield to the wavefield at $\mathbf{x}_B$ in the actual wavefield (Figure 2.5). Note that the position $\mathbf{x}_B$ was assumed to be inside $\mathbb{V}$ and $\mathbf{x}_S$ outside $\mathbb{V}$. $\oint_{\mathbb{S}}$ can be exchanged as $\int_{\mathbb{S}_0}$ considering Sommerfeld condition.

Contrary to the correlation-type Green's function representation (equation 2.20), the convolution-type Green's function representation (equation 2.32) is valid for the dissipative medium. Furthermore, it includes the reference wavefield (desired wavefield we want to estimate) in the integral along the closed surface. Therefore, we need to inversely solve the relation. The detail of the method to solve this relation is discussed in the Chapter 5 and Chapter 6. Note that the convolution-type Green's function representation can be derived using the one-way wavefield reciprocity (see Appendix). We used the relation derived from one-way wavefield reciprocity in Chapter 6. However, the form of the equation is identical to equation 2.32.

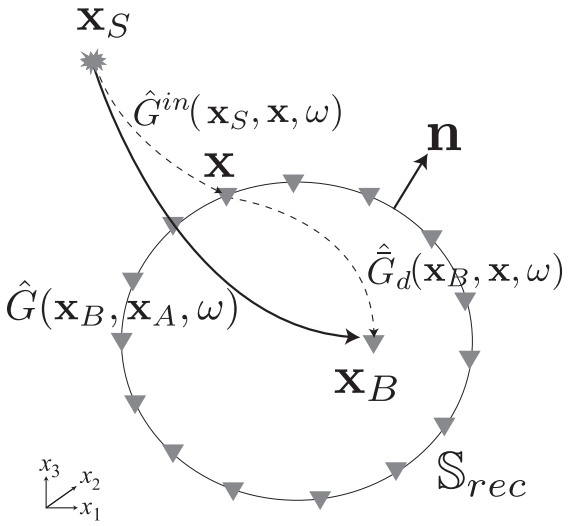

Figure. 2.5: Configuration for SI by MDD. Objective function $\hat{\hat{G}}_d(\mathbf{x}_B, \mathbf{x}, \omega)$ is formulated as a integral along the receiver surface.

3 Extracting reflected waves from upper oceanic crust boundary at Nankai Trough area by crosscorrelating stationary-phase records

3.1 Introduction

Seismic Interferometry (SI) retrieves Green's function between receivers by crosscorrelating wavefield. This theory requires the physical sources homogeneously distributed along the enclosed surface which surrounds the receivers (Wapenaar and Fokkema, 2006). SI is successfully applied to the teleseismic records (Tonegawa et al., 2009) to retrieve the large scale reflected waves such as the Moho reflections. The teleseismic events are suitable to SI processing since the most earthquakes are generated at the numerous plate boundaries in the world and consequently the teleseismic records contain the earthquakes propagating from the various directions. This can enable us to assume their source distribution is homogeneous. The teleseismic events usually have long propagating path and lose their higher frequency components. Consequently only the large scale structure can be detected. On the other hand, the local earthquakes which have shorter raypath are expected to contain the higher frequency components and to detect more fine-scale structures by SI. However, such local earthquakes are usually inhomogeneously distributed. This violates the assumption of SI and the conventional SI processing (crosscorrelation and summation) yields to the deteriorated subsurface images.

The physical interpretation of the condition to be posed on the SI can be explained by the stationary phase approximation (Schuster et al., 2004; Schuster, 2009). In this approximation, it explains that the dominant contribution of the retrieval of the Green's function comes from the crosscorrelation of the records from the physical source located at the stationary phase position (stationary phase source). In other words, when the stationary phase source does not exist in the localized distribution, the objective Green's function cannot be retrieved.

We usually have receiver array to observe wavefield from physical sources. Therefore, the number of combination of crosscorrelation is dependent on the number of receivers. Due to the above explanation, in the localized source distribution, only a part of the crosscorrelation pairs whose sources are the stationary phase sources have physical meaning. The other crosscorrelation traces will produce noise and deteriorate the quality of the imaging results.

We use the stationary phase interpretation to obtain high-quality imaging results in the localized source distribution. The important characteristic of the stationary phase sources is that it produces the same raypath between two receivers to be crosscorrelated. Therefore we identify the events which produce objective wavefield and estimate their raypath by ray-theory. Fur-

thermore, we choose the crosscorrelation traces which is produced by stationary phase sources using estimated raypath. We show the numerical modeling result to check the validity of this method. Furthermore, we use Ocean Bottom Seismogram (OBS) records which observe local earthquakes.

We use the OBS records as the field data. These OBS are installed at the Nankai trough area to detect the local earthquakes. We show the possibility to image the upper oceanic crust boundary by using locally distributed earthquakes. This processing has a possibility to monitor the Nankai trough area without using the active sources and to obtain the higher resolution images than using the teleseismic records.

3.2 Estimation of stationary-phase records using raypath calculation

3.2.1 Stationary phase approximation of Seismic interferometry

Seismic interferometry by crosscorrelation is written as,

$$\hat{G}(\mathbf{x}_B, \mathbf{x}_A, \omega) + \hat{G}^*(\mathbf{x}_B, \mathbf{x}_A, \omega) = \frac{2k}{\omega\rho} \oint_{\mathbb{S}_{src}} \hat{G}(\mathbf{x}_B, \mathbf{x}_S, \omega)\hat{G}^*(\mathbf{x}_A, \mathbf{x}_S, \omega) d^2\mathbf{x}_S \,. \tag{3.1}$$

where $\hat{G}(\mathbf{x}_A, \mathbf{x}_S, \omega)$ and $\hat{G}(\mathbf{x}_B, \mathbf{x}_S, \omega)$ are the observed wavefield from the sources $\mathbf{x}_S$ along the closed surface. $\hat{G}(\mathbf{x}_A, \mathbf{x}_B, \omega)$ is a Green's function between two receiver positions.

We assume that we retrieve the primary reflection by crosscorrelating a direct wave and a specular reflection from the physical sources (Figure 3.1(a)).

$$\hat{G}(\mathbf{x}_A, \mathbf{x}_S, \omega) = e^{i\omega\tau_{SA}}, \tag{3.2}$$

$$\hat{G}(\mathbf{x}_B, \mathbf{x}_S, \omega) = e^{i\omega\tau_{SyB}} \tag{3.3}$$

where τ_{SA} denotes a travel time of a direct wave from $\mathbf{x}_S$ to $\mathbf{x}_A$. τ_{SyB} denotes a travel time of a specular reflection from the source position $\mathbf{x}_S$ to the receiver position $\mathbf{x}_B$ through specular reflection point y. Note that the amplitudes of these wave are assumed to be normalized in equation 3.3. Substituting these waves into equation 3.1 and applying stationary phase approximation yields,

$$2\Re\hat{G}(\mathbf{x}_B, \mathbf{x}_A, \omega) \approx e^{i\omega\tau_{Ay_0B}} \oint_{\mathbb{S}} e^{i\omega(\tau_{SyB}-\tau_{SA}-\tau_{Ay_0B})} d^2\mathbf{x}_S \tag{3.4}$$

$$\approx \alpha e^{i\omega\tau_{Ay_0B}} \tag{3.5}$$

where τ_{Ay_0B} denotes a travel time of the specular reflection between two receiver position through its specular reflection point. α denotes a coefficient for stationary phase approximation. The integral of equation 3.5 has a stationary point at $\mathbf{x}_S = \mathbf{x}_S^*$ and the objective primary reflection is retrieved (Schuster, 2009). Furthermore in this stationary point, following relation is satisfied.

$$\tau_{S^*yB} - \tau_{S^*A} - \tau_{Ay_0B} = 0 \tag{3.6}$$

This relation states that for the stationary phase source position, the two events (direct wave and reflected wave in this case) have same raypath from the source position to the receiver position (Figure 3.1(b)). This corresponds to the fact that the crosscorrelation processing subtracts the travel times, cancels the common raypath and produces the traveltime of the objective reflection event between receivers.

Note that the amplitudes resulted from the crosscorrelation of the non stationary phase sources are cancelled after the summation of the homogeneously distributed sources along the enclosed surface. In the case of the local source distribution, the cancellation is insufficient and the unwanted amplitudes remain.

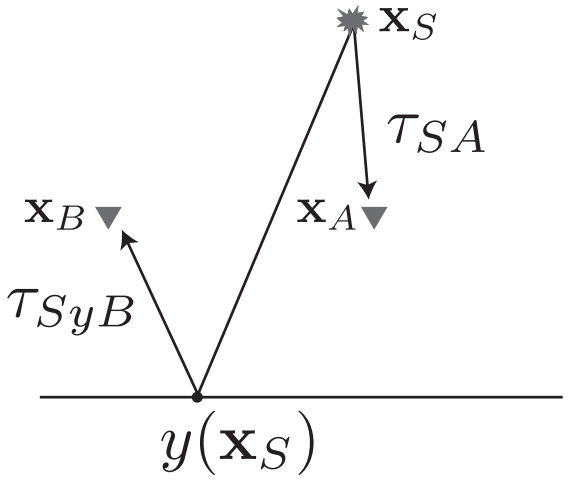

(a)

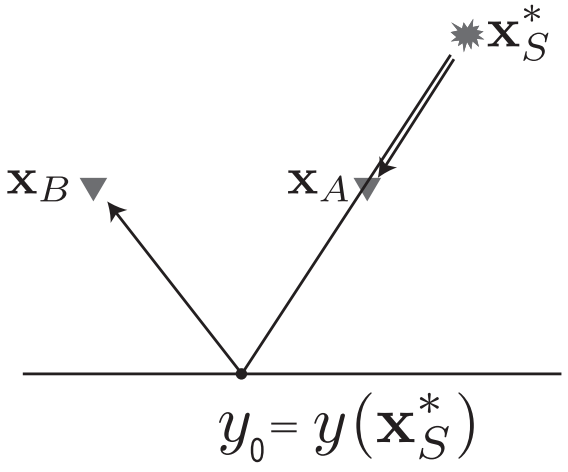

(b)

Figure. 3.1: (a) Receiver $\mathbf{x}_A$ observe direct wave with the travel time τ_{SA} and $\mathbf{x}_B$ observe reflected wave with τ_{SyB}. The specular reflect position $y(\mathbf{x}_S)$ varies with the source position $\mathbf{x}_S$. (b) When the source position $\mathbf{x}_S$ satisfies the stationary phase position $\mathbf{x}_S^*$, two events have common raypath between $\mathbf{x}_S$ and $\mathbf{x}_A$.

3.2.2 Selection of receivers by stationary-phase evaluation

When the physical sources widely distribute, the stationary phase sources effectively produce the objective reflection events. On the other hand, when the source distribution is localized, only the reflection events which have the stationary phase sources are retrieved. Therefore, we evaluate the crosscorrelation traces for the existence of the stationary phase source and remove those which do not have the stationary phase sources. We assume that we can estimate the raypath propagating from the source position to the two receivers. When these two raypaths have common pathway, we define that the crosscorrelated trace using these receivers contains objective reflections.

In order to evaluate the existence of the stationary phase sources, the raypaths for the direct waves and the arbitrary multiple reflected waves are needed to be estimated. We adapted the method developed by Tamagawa et al. (1997). This method geometrically calculates the raypath for arbitrary multiple reflections with given 3 dimensionally deviated structures assuming straight raypath (Figure 3.2). When we have two reflector plane, the method calculates the mirror point of the source position for the reflector planes ($M1 \rightarrow M2 \rightarrow M3$ in Figure 3.2). The arbitrary multiple reflection raypath can be derived by connecting those mirror points to the receive position ($R3 \rightarrow R2 \rightarrow R1$ in Figure 3.2). This method is simple and fast to calculate. We evaluate the stationary phase using these raypath. For example, we assume that the receiver $\mathbf{x}_A$ observe direct wave and two different receivers $\mathbf{x}_B$, $\mathbf{x}'_B$ observe reflected wave (Figure 3.3). The candidate for crosscorrelation processing is $\mathbf{x}_A - \mathbf{x}_B$ and $\mathbf{x}_A - \mathbf{x}'_B$. Stationary phase evaluation using raypath can give us the information that only the crosscorrelation of $\mathbf{x}_A - \mathbf{x}_B$ has a stationary phase source and contain the objective reflection event. By evaluating this procedure for all source position and receiver combination, we remove the crosscorrelation traces which do not have stationary sources for objective reflections.

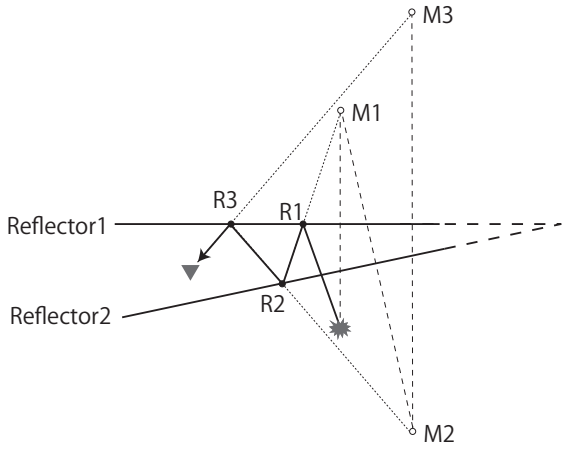

Figure. 3.2: Raypath calculation for multiple reflections.

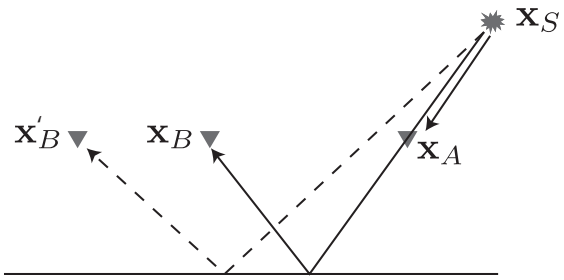

Figure. 3.3: Source $\mathbf{x}_S$ is a stationary source for the crosscorrelation pair $\mathbf{x}_A - \mathbf{x}_B$.

3.3 Numerical modeling results

We numerically simulate the wavefield with localized source distribution and evaluate the processing described above. We consider that we observe the local earthquakes with Ocean Bottom Seismogram (OBS) installed at the sea floor. The objective reflection events are assumed to be those generated from the upper oceanic crust boundary. We consider the only one physical source which is the most localized source distribution. The velocity model is a three-layer structure including sea water (Figure 3.4). The dipping structure is simulated as a upper oceanic crust boundary in Nankai trough area.

We define the two events which produce the objective reflection event for the stationary phase evaluation. In our source-receiver configuration, the source is located in the subsurface and the sea surface (modeled as a free-surface) expects to produce the strong down-propagating reflections. Therefore we assume that the sea-surface P-wave reflections (denoted as pP) and the sea-surface multiple P-wave reflections (pPp) produce the reflection events from upper oceanic crust boundary after crosscorrelation. There are other events to contribute to produce the objective reflection event, for example, the crosscorrelation of the direct P-wave and the multiple P-wave reflections. In this study we consider the crosscorrelation of these two event (pP and pPp) since they propagate with high energy and are easy to be separated from S-waves.

We numerically modeled the seismic wavefield with the one subsurface source. We used the 2 dimensional staggered grid method (Virieux, 1986). The subsurface source is installed at the 30 km depth. We simulate the earthquake by giving horizontal stress as a source and using a ricker wavelet with the central frequency of 5 Hz. The receiver array is installed at the sea floor. The length of receiver array is 50 km with 200 m intervals.

We show the calculated wavefield at the receiver array in Figure 3.5. The Figure 3.5 shows the vertical component of the wavefield. One can see that the sea-surface reflections (pP) and the sea-surface multiple reflections (pPp) are observed as well as the direct P-wave and direct S-wave. Since we consider only P-waves, we muted the amplitude below the travel time of the direct S-wave and apply crosscorrelation. We have 251 receivers and the total number of the crosscorrelation traces is ${}_{251}C_2$. We used all crosscorrelation traces for imaging (Figure 3.6). The figure 3.6 shows the result of PSDM. The dipping structure was appeared on the image. However, the signal-to-noise ratio at the near offset is low and the artifact dipping events are appeared. These artifacts are caused by the crosscorrelation traces which do not have a stationary

phase source for objective reflections.

We evaluate the stationary phase source to remove the unwanted crosscorrelation traces. We estimate the raypath of pP and pPp and compare their raypaths. We fix the receiver which observe pP (denoted as R_{pP})and calculate the raypath of pPp for all receivers R^i_{pPp}. We calculate the horizontal distance of the receiver R^{pP} and the point where pPp passes through the seafloor to a downward direction. We refer to the distance as an interferometric distance (Figure 3.4). The interferometric distance of zero indicates that the two events have the common raypath between the buried source to the receiver R^{pP}. Due to the receiver spacing, the interference distance of zero does not always exist (Figure 3.7). Therefore we define the threshold for the interferometric distance. The receivers R^i_{pPp} with the interferometric distance less than the threshold value are assumed to have the common raypath. This threshold could also compensate for the ambiguity of the raypath due to the curved raypath and the uncertainty of the given structure by stacking the coherent amplitudes with the scale of the wavelength in the case of the application to the field data. We iterate this procedure by changing the fixed receiver R_{pP} and evaluate all combination of crosscorrelation traces.

We removed the crosscorrelation traces which do not have a stationary phase source for objective reflections and apply PSDM. We used 2489 traces for PSDM. Figure shows the result of PSDM. One can see that the S/N at the near offset improved and the artifact events are suppressed. We conclude that evaluating stationary phase by raypath and removing unwanted crosscorrelation traces improve reflection images.

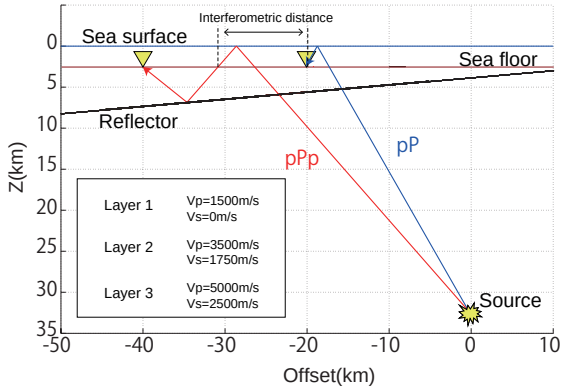

Figure. 3.4: Velocity model for the numerical modeling. pP and pPp denote the sea surface reflection and the sea surface multiple reflection respectively.

3.4 Extracting reflected waves of upper crust boundary from OBS records at Nankai Trough area

We apply this procedure to the field data. The field data consists of the OBS records installed at Nankai trough area to observe local earthquakes. This dataset was originally obtained by JAMSTEC for the earthquake observation in subduction zone (Obana et al., 2004, 2005). The

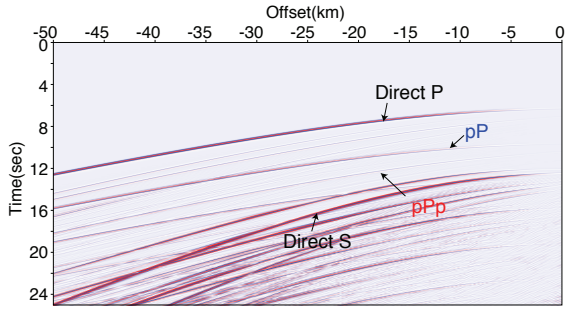

Figure. 3.5: Vertical component of the modeled seismic wavefield. Arrows show the dominated events.

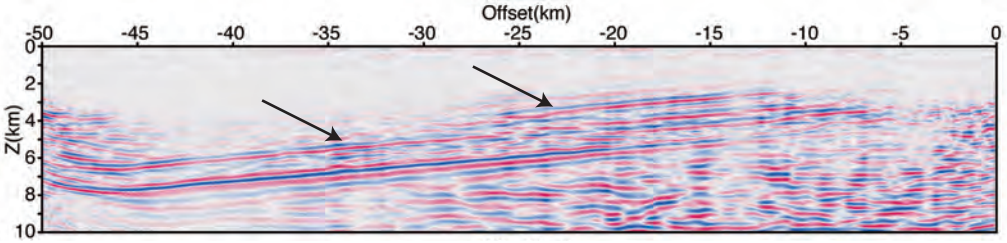

Figure. 3.6: PSDM imaging result using all CC traces. Arrows show the artifact events.

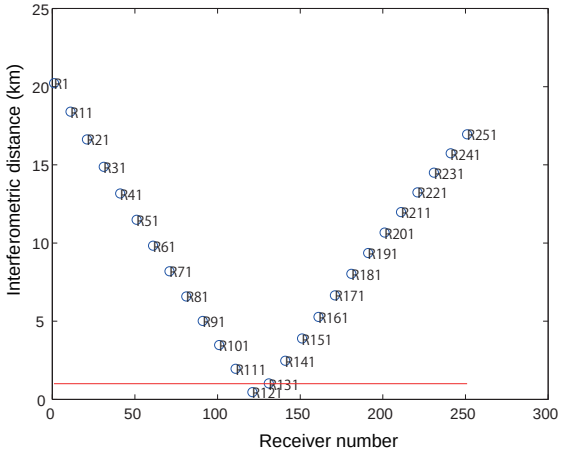

Figure. 3.7: Example of the interferometric distance for different R_{pPp} with the fixed R_{pP}. The receiver R_{pPp} with the interferometric distance less than the threshold value is defined as the stationary phase pair.

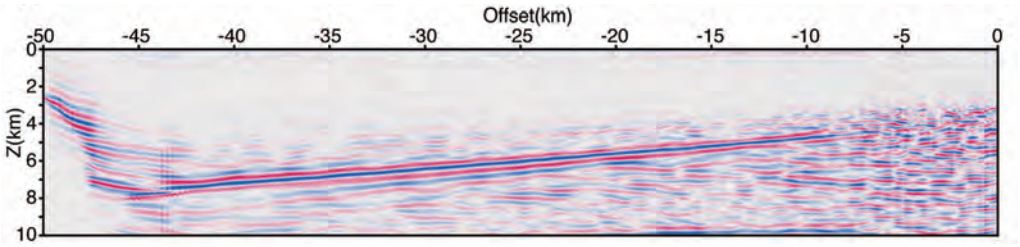

Figure. 3.8: PSDM imaging result using selected CC traces by stationary phase evaluation.

28 OBS are 3 dimensionally installed at the approximately 100km squared area for 12 days in March 2005 (Figure 3.9(a)). We extract the reflection events generated at the upper oceanic crust boundary using crosscorrelation. The 653 local earthquakes are detected. Within those earthquakes, we consider 6 earthquakes whose magnitudes are larger than 3.0 and their depth are larger than 20 km (Figure 3.9(b)). We expected that these earthquakes contain large energy, the P-wave energy is dominated in the vertical component of the records and the arrival time of S-waves are late enough to be separated from P-waves. One can see these earthquakes are localized at south-west of the survey area.

We show the 168 traces from the 6 events aligned by the epicentral distance and corrected origin time as the time of the earthquakes (Figure 3.10). The dominant frequency was 5Hz. One can see two events appearing with different propagating velocity. Since the first arrival is dominated in the vertical component, we assumed them as the P-waves and the second arrivals as the direct S-waves. We muted the amplitude at the travel time below second arrival to consider only P-wave events.

Figure 3.11(a) shows the reflection profile from the 3D multi-channel seismic survey (Moore et al., 2009). The red line (line IL) of Figure 3.9(a) shows its 2D crossline. The crossline runs approximately perpendicular to the trough axis. The upper oceanic crust boundary in this area is located 7 km below sea floor dipping toward north direction (Figure 3.11(a)). We assumed the northward-dipping structure with the angle of 5.5 degree from this figure. We extended this structure perpendicular to the 2D crossline in Figure 3.9(a) and obtain the 3D dipping structure used for raypath calculation (Figure 3.11(b)).

We estimated the raypahs of the sea-surface reflection (pP) and the sea-surface multiple reflection (pPp). To account for the difference of each elevation of OBS, we defined the interference distance as the distance between the receiver R_{pP} and the point where pPp passes through the horizontal plane constructed by the receiver R_{pP} to a downward direction. We defined the threshold of the interference distance as 5 km. We removed the crosscorrelation traces which do not have the stationary phase sources and obtained 55 crosscorrelation traces. Since we calculated the raypath, we can estimate the reflection point at the given structure (Figure 3.12). One can see that due to the source localization, only a part of combination of the receivers are selected.

We applied the 3D PSDM to the crosscorrelation traces. We extended the tomographic velocity by Nakanishi et al. (2002) perpendicular to its survey line (KR9806) and used it as a velocity

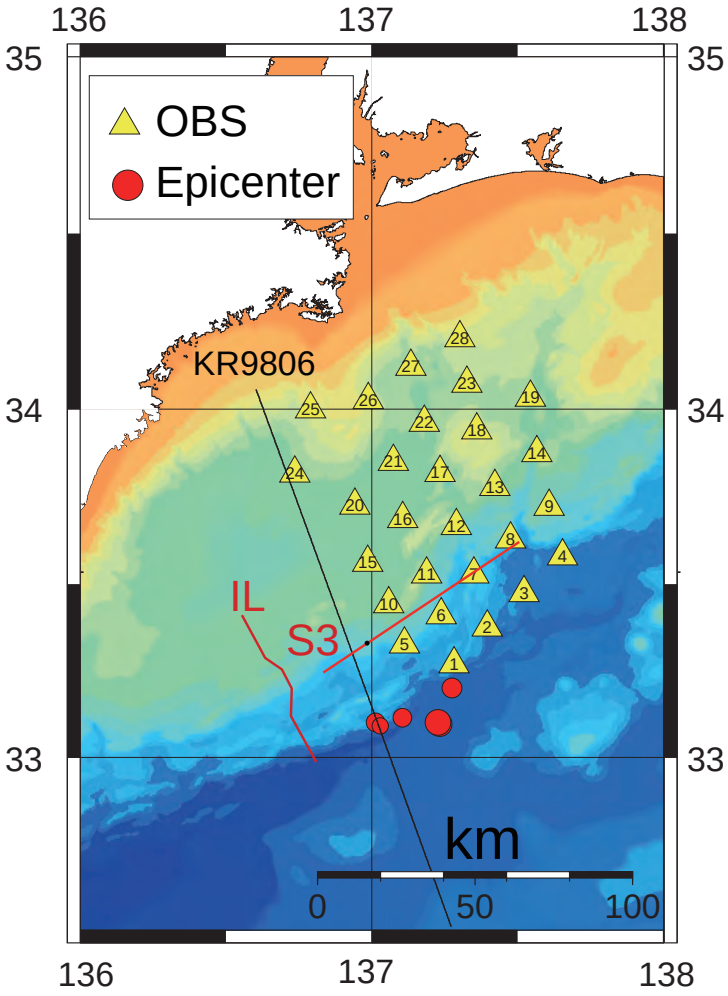

(a)

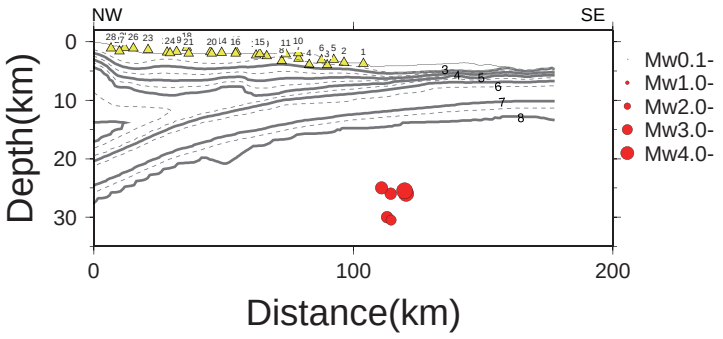

(b)

Figure. 3.9: (a) Survey area at Nankai trough. Three survey lines, KR9806, IL and S3 indicate those from Nakanishi et al. (2002), Moore et al. (2009), and Park et al. (2004) respectively.(b)The depth of OBS and earthquakes projected to the line KR9806. Background velocity contour is from refraction tomography (Nakanishi et al., 2002).

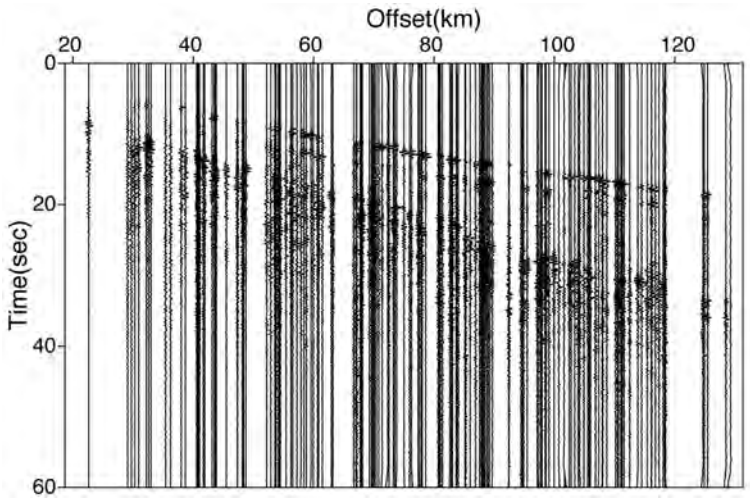

(a)

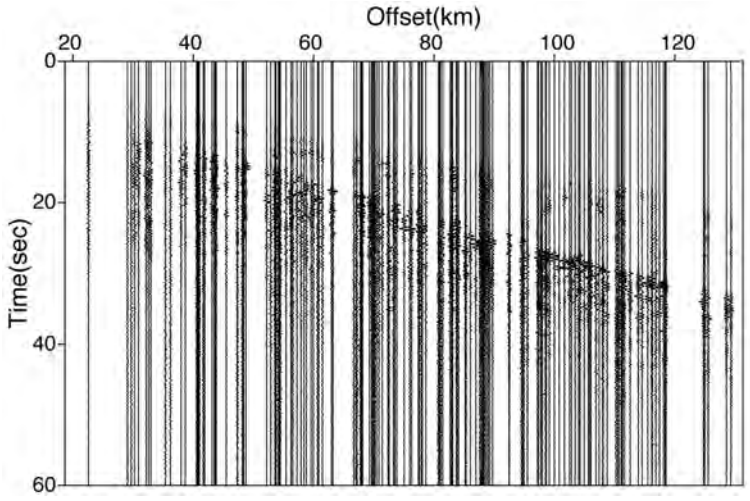

(b)

Figure. 3.10: Data of the 168 traces from the 6 events aligned by the epicentral distance after correcting the origin time as the time of the earthquakes. (a) Vertical component. (b) Horizontal component.

model for PSDM. The expected reflection points are sparsely distributed in the 3D region (Figure 3.12). Therefore, we spatially stacked the 3D imaging result and obtained the pseudo-2D profile.

We show the pseudo-2D profile stacked perpendicular to the line KR9806 in Figure 3.13(a). Furthermore, we overwraped the reflection profile (Moore et al., 2009). We only focus on the upper oceanic crust boundary and the result shows that the boundary at the same depth appeared in the section IL is imaged (arrows in Figure 3.13(a)). We show the pseudo-2D profile stacked perpendicular to the line S3 (Park et al., 2004). in Figure 3.13(b). This pseudo-2D profile runs parallel to the trough axis. We converted the depth axis of our imaging result to the time axis using the migration velocity model and overwraped by the reflection profile of line S3. One can see that it shows the dominated amplitudes at the same two-way time of upper oceanic crust boundary in the line S3 and also shows the local bulge of the upper oceanic crust boundary (arrows in Figure 3.13(b)). For a comparison, we show the PSDM result using all CC traces stacked perpendicular to the trough axis (Figure 3.13(c)). One can see that it is difficult to detect the upper oceanic crust boundary and stationary phase evaluation improves the quality of the imaging result.

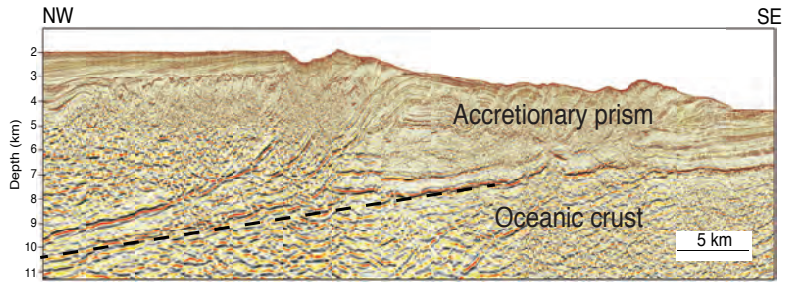

(a)

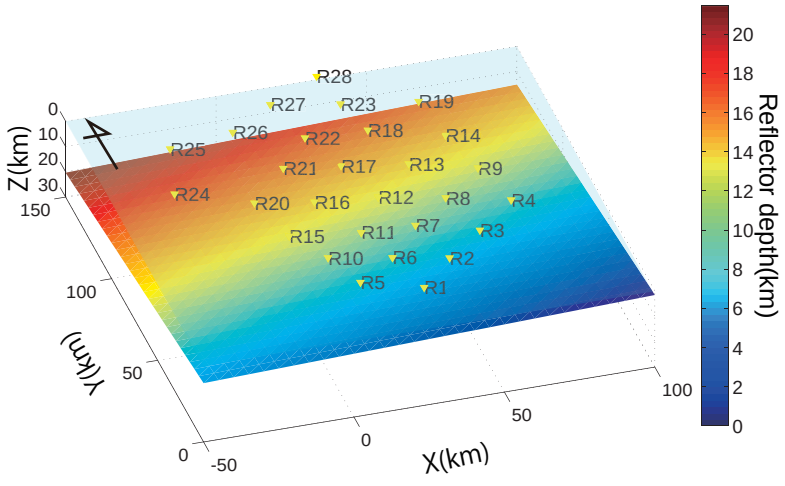

(b)

Figure. 3.11: (a)2D reflection profile (Moore et al., 2009). Dots show the angle of 5.5 degree. (b) Constructed 3D dipping structure for the raypath calculation.

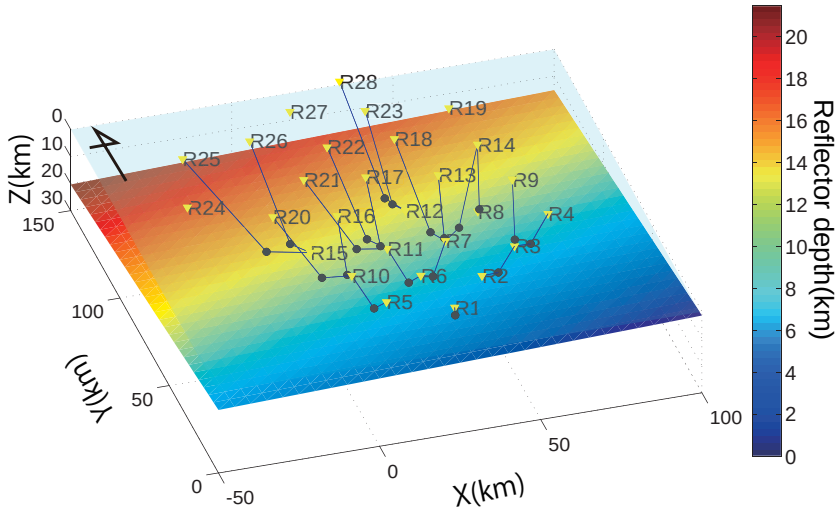

Figure. 3.12: Reflection points estimated by a raypath calculation (Black dots).

3.5 Conclusion

We use the stationary phase interpretation to obtain high-quality imaging results in the localized source distribution. We estimate the raypath of two reflection event which are sea-surface P-wave reflection and sea-surface multiple P-wave reflection. We choose the crosscorrelation traces which is expected to produce objective reflections due to the stationary phase sources using the estimated raypath. We show the numerical modeling result to check the validity of this method. Furthermore, we use Ocean Bottom Seismogram (OBS) records which observe local earthquakes. The OBS records contains 6 localized earthquakes. We show that choosing the CC traces by stationary-phase evaluation improves the quality of the imaged reflection boundary of the upper oceanic crust. This processing has a possibility to monitor the Nankai trough area without the active sources and higher resolution than using teleseismic records.

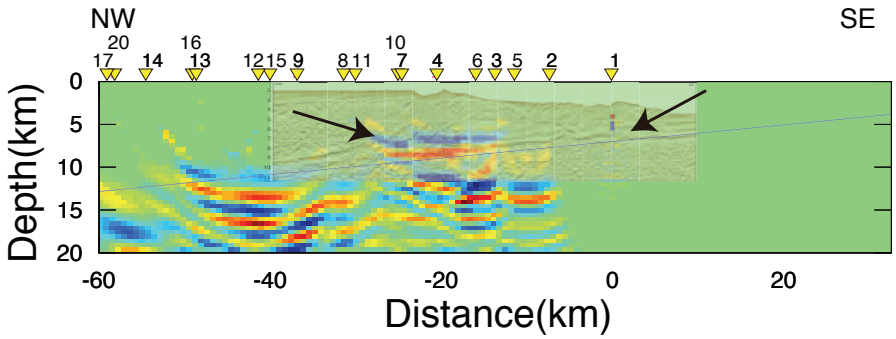

(a)

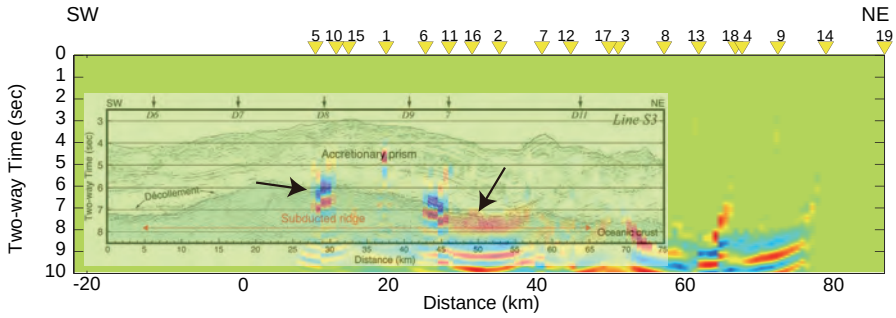

(b)

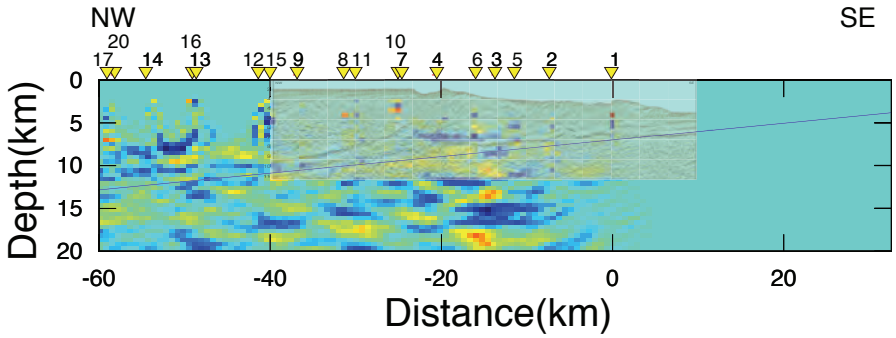

(c)

Figure. 3.13: PSDM imaging results. (a) Stacked perpendicular to Line KR9806. The seismic profile from Moore et al. (2009) is overwraped. Arrows show the imaged upper oceanic crust boundary. (b) Stacked perpendicular to Line S3. The seismic profile from Park et al. (2004) is overwraped.(c) Stacked perpendicular to Line KR9806 using all CC traces.

4 Monitoring seismic velocity change caused by The 2011 off the Pacific coast of Tohoku Earthquake from ambient noise records

4.1 Introduction

In order to observe the dynamic change of the medium, the repeatedly-produced impulse response or the Green's function is required. The classical method assumes that the signal from the earthquakes or the wavefield generated by the artificial sources is a bandpass filtered impulse response (e.g., Poupinet et al., 1984; Nishimura et al., 2000). These studies, however, have the limited applicability since the former study has the difficulty to repeatedly obtain the earthquakes at the similar position and focal mechanism with the fine time coordinate, and the latter is rather expensive and limited penetration. The seismic interferometry (SI) or reverse-time acoustics is employed to overcome these problems (e.g., Derode et al., 2003; Roux et al., 2005; Wapenaar and Fokkema, 2006; Larose et al., 2006). The SI retrieves the impulse response using crosscorrelation of the wavefield and it has gained popularity to obtain the impulse response using seismic ambient noise.

Using ambient noise to retrieve seismic response is suitable to monitor the dynamic change since they are continuously observed. There are successful applications of the SI using the ambient noise to retrieve the surface wave and estimate the group velocity distribution (Shapiro et al., 2005) or to retrieve the reflection response (Draganov et al., 2009). Furthermore, retrieving scattered wave is alternatively employed to detect the small change of the propagating velocity (Sens-Schönfelder and Wegler, 2006; Brenguier et al., 2008; Meier et al., 2010). The method is called 'passive image interferometry'. The autocorrelation of the ambient noise is interpreted as the source-receiver collocated seismic response (zero-offset response). Wegler and Sens-Schönfelder (2007) and Ohmi et al. (2008) used the autocorrelation function (ACF) to monitor the temporal change of the impulse response triggered by the earthquakes.

It became a well known phenomena that the earthquakes cause the velocity change of the crustal rocks by the several mechanism. There are widely studied researches that the velocity shows dependency to the static stress condition (e.g., Toksöz et al., 1976; Christensen and Wang, 1985; Tsuji et al., 2008). Several studies claim that the velocity change associated with the stress change due to the earthquakes are observed by using multiplet earthquakes (e.g., Poupinet et al., 1984) or controlled source experiments (e.g., Nishimura et al., 2000; Niu et al., 2008). The another possibility which causes the velocity change is known as a non-linear fast dynamics (NFD) and slow dynamics (SD) where the elastic properties evolve when the stress-strain conditions are beyond the assumption of the linear elasticity (e.g., Lyakhovsky et al., 1997; TenCate

et al., 2000; Johnson and Sutin, 2005). Recently it has been reported that the velocity change associated with those effects due to the strong ground motion of the earthquakes is observed using multiplet earthquakes (Schaff and Beroza, 2004; Rubinstein and Beroza, 2004; Peng and Ben-Zion, 2006) or controlled source experiments (Vidale and Li, 2003). There are few studies using passive image interferometry which detected the velocity change, possibly reflecting the effects for both the stress change and near surface damaging due to the strong shaking (e.g., Wegler and Sens-Schönfelder, 2007; Brenguier et al., 2008).

On 11 March, 2011 an Mw 9.0 earthquake occurred off the pacific coast of Tohoku region, Japan (Figure 4.1(a)). The GPS network observation revealed that the coseismic displacement shows eastward movement of up to 5.3 m and subsidence by up to 1.2m in the eastern Japanese island arc (Ozawa et al., 2011). The large displacement due to the Tohoku Earthquake caused enormous strain change in the Tohoku region (Takahashi, 2011). Furthermore, the strong ground motion due to the seismic wave was observed. Therefore, these phenomena may widely cause the change of the propagating velocity. We analyzed the continuously recorded seismic data to monitor the velocity change at the South Tohoku region.

4.2 Method

We analyzed the ambient seismic records from Hi-net in Japan. Seismic response can be retrieved using crosscorrelation of the wavefield (Wapenaar and Fokkema, 2006).

$$\hat{G}(\mathbf{x}_B, \mathbf{x}_A, \omega) + \hat{G}^*(\mathbf{x}_B, \mathbf{x}_A, \omega) = \frac{2k}{\omega\rho} \oint_{\mathbb{S}_{src}} \hat{G}(\mathbf{x}_B, \mathbf{x}_S, \omega)\hat{G}^*(\mathbf{x}_A, \mathbf{x}_S, \omega) d^2\mathbf{x}_S . \tag{4.1}$$

If the observed wavefield can be described as the simultaneous acting noise source,

$$\hat{p}^{obs}(\mathbf{x}_A, \omega) = \oint_{\mathbb{S}_{src}} \hat{G}(\mathbf{x}_A, \mathbf{x}_S, \omega)\hat{N}(\mathbf{x}_S, \omega) d^2\mathbf{x}_S , \tag{4.2}$$

$$\hat{p}^{obs}(\mathbf{x}_B, \omega) = \oint_{\mathbb{S}_{src}} \hat{G}(\mathbf{x}_B, \mathbf{x}_S^{'}, \omega)\hat{N}(\mathbf{x}_S^{'}, \omega) d^2\mathbf{x}_S^{'} . \tag{4.3}$$

where $\hat{p}^{obs}(\mathbf{x}, \omega)$ denotes the observed seismic wavefield in the frequency domain. Autocorrelation of the ambient noise records yields to the seismic response with the coincident source and receiver position.

$$< \hat{p}^{obs*}(\mathbf{x}_A, \omega)\hat{p}^{obs}(\mathbf{x}_A, \omega) > = \oint_{\mathbb{S}_{src}} \hat{G}(\mathbf{x}_A, \mathbf{x}_S, \omega)\hat{G}^*(\mathbf{x}_A, \mathbf{x}_S, \omega) d^2\mathbf{x}_S \tag{4.4}$$

$$= 2\Re\hat{G}(\mathbf{x}_A, \mathbf{x}_A, \omega)\hat{S}(\omega), \tag{4.5}$$

where we substitute $\mathbf{x}_B = \mathbf{x}_A$ since we only focus on the autocorrelation. The bracket <> stands for the ensemble averaging. This relation assumes the noise source $\hat{N}(\mathbf{x}_S, \omega)$ is mutually uncorrelated for the different source position as,

$$< \hat{N}^*(\mathbf{x}_S, \omega)\hat{N}(\mathbf{x}_S^{'}, \omega) >= \delta(\mathbf{x}_S - \mathbf{x}_S^{'})\hat{S}(\omega). \tag{4.6}$$

Thus, the phase of the noise source should be random. The earthquakes with the deterministic phases are unwanted event. We apply the running absolute amplitude normalization (Bensen et al., 2007) to suppress those earthquakes.

$$p_i^{norm} = p_i / w_i, \tag{4.7}$$

$$w_i = \frac{1}{2N+1} \sum_{j=i-N}^{i+N} |p_j|. \tag{4.8}$$

where p_i and w_i denote the i-th sampling value of the observed records and the weight function in the time domain. The window size $(2N+1)$ affects the weighting range to suppress the strong amplitudes. We found that the value of the window size significantly affects the travel time of the coherent events in the autocorrelation function (ACF). We carefully investigate the values and determined to use the window length of 25 s. Furthermore, we apply zero-phase amplitude whitening to balance the frequency component (Bensen et al., 2007; Meier et al., 2010). We use the moving averaged amplitude around the considering frequency for the amplitude whitening and the 5% of the maximum amplitude for the damping factor to stabilize the whitening.

In order to estimate the velocity perturbation due to the earthquakes, we apply the stretching interpolation technique (e.g., Sens-Schönfelder and Wegler, 2006; Hadziioannou et al., 2009). The produced ACF represents the zero-offset seismic response and contains the scattered wave with the traveltime perturbation evolving each day. The method elongates and interpolates the time axis of the calculated trace and searches for the best parameter which produces the similar waveform to the reference trace.

$$f_\epsilon^{cur}(t) = f^{cur}(t(1+\epsilon)), \tag{4.9}$$

$$C(\epsilon) = \frac{\int f_\epsilon^{cur}(t) f^{ref}(t) dt}{\left(\int (f_\epsilon^{cur}(t))^2 \, dt \int (f^{ref}(t))^2 \, dt \right)^{\frac{1}{2}}} \tag{4.10}$$

where ϵ is a stretching parameter. f^{ref} and f^{cur} represent the reference trace and the current trace respectively. $C(\epsilon)$ is a correlation coefficient between the reference trace and elongated trace. We search for ϵ which has the maximum value of C by equation 4.10. We adopted a grid search algorithm. Since a part of data suffers from the local maxima, we manually picked the local maxima which smoothly transitions to each day for such data. ϵ corresponds to a travel time perturbation of dominant event and we assume it relates to a velocity perturbation,

$$\epsilon = \frac{\Delta t}{t} = -\frac{\Delta v}{v} \tag{4.11}$$

Note that in this analysis we assume that (1) autocorrelated trace is dominated by the scattered wave generated from the subsurface and (2) the travel time perturbation directly corresponds to the velocity perturbation, which indicate the velocity perturbation is homogeneous in the medium, or is homogeneous at least in the region where the scattered waves propagate within the specified time window. Note that there is another method to estimate the small change of the velocity. The method calculates the phase difference between traces in the frequency domain with moving window. The velocity perturbation is estimated by the slopes of the phase

difference with various lapse time (e.g., Fréchet et al., 1989; Snieder et al., 2002). Hadziioannou et al. (2009) discussed their advantages and drawbacks.

4.3 Result

4.3.1 Survey area and Data

We show the survey area in Figure 4.1(b). We use the vertical component of the 58 Hi-net stations with the 6-month long continuous records from 9 January 2011 to 30 June 2011 which result in total 173 days. The sampling frequency is 100 Hz. These Hi-net stations are operated by NIED (National Research Institute for Earth Science and Disaster Prevention). Although the maximum depth of station is 3500 m, the most stations are distributed from 100m to 200m depth (Figure 4.1(b)). Survey area includes Fukushima and Ibaraki prefectures. In this duration, the survey area has experienced at least two aftershocks with a large surface deformation detected by the satellite observation (InSAR, Interferometric synthetic aperture radar) operated by Geospatial Information Authority of Japan (GSI, http://www.gsi.go.jp). They are (1) at North Ibaraki on 19 March with Mw 5.8 (10km depth) and (2) at South Fukushima on 11 April with Mw 6.7 (10km depth) respectively (Figure 4.1(b)).

We show the preprocessed vertical component of the data at station N.YBKH for 600 second at 20 January (Figure 4.2). These ambient noises are autocorrelated and produce the zero-offset seismic response.

4.3.2 ACF and temporal variation of the velocity perturbation

We autocorrelated each 1 day-long seismic data and obtained 173 autocorrelation function (ACF). We show the ACF at the station N.YBKH (Figure 4.3). The data for 2s-10s was shown after bandpass filtering between 2Hz to 5Hz. Since the data for the duration of 13-14 March was not available, the amplitudes of these traces are zero. One can see the coherent event appeared in the ACF (Figure 4.3) and its characteristics was changed after 11 March.

We show the temporal change of the velocity (travel time) perturbation (ϵ) at station N.YBKH in Figure 4.4. We stacked all ACF to obtain the reference trace for equation 4.9 and as a calculate trace we used each 1-day ACF after applying the 5-day long centering moving average window. We calculated $C(\epsilon)$ for a range of $-10\% \leq \epsilon \leq 10\%$ with $\Delta\epsilon = 0.1\%$ and picked the maximum values after spline interpolation. Here we use the ACF for a period of 2s-10s. Since the averaged waveform was defined as the zero percentage perturbation, ϵ starts from around -0.5%. The positive ϵ indicates that travel time was longer in the current trace than in the averaged trace, or that the velocity was slower. One can clearly see that the sudden change of ϵ at 11 March (The Tohoku Earthquake) and the velocity dropped 2%. Furthermore, the gradual healing of the velocity (e.g. Peng and Ben-Zion, 2006; Vidale and Li, 2003; Schaff and Beroza, 2004; Rubinstein and Beroza, 2004) was observed after the Tohoku Earthquake. We fit the logarithmic line as $\epsilon(d) = a \log_{10}(d) + b$ where d is a collapsed day and we obtain the healing rate of 0.53

(white line in Figure 4.4). The coseismic velocity perturbation remained around 1% at 100 days after the Tohoku Earthquake. This observation coincides to the earlier study focusing on the velocity change at the near surface due to the Tohoku Earthquake (Nakata and Snieder, 2011).

The stretching interpolation technique (Equation 4.9) assumes the homogeneous velocity change within the time window. However, the scattering events at the different travel time may propagate different region of the medium and consequently they may contain the information of the different depth. Therefore we conducted the stretch interpolation technique (equation 4.9) with the different time window. Figure 4.5 shows the calculated velocity perturbation with the time window of 2s-10s, 2s-6s and 6s-10s respectively. One can see that the coseismic jump at 11 March with the window of 2s-6s (approximately 3%) is larger than that with the window of 6s-10s (approximately 0.5%). This may indicate that the coherent events with longer travel time propagate carrying the information of deeper structures and the shallower subsurface experienced larger velocity reduction than deeper subsurface. The window size of 2s-10s shows averaged values for the other two time windows.

Figure 4.6 shows the temporal variation of the velocity change at station N.TWAH which locates far from the hypocenter of the Tohoku Earthquake than N.YBKH. One can see the same trend that the velocity jumps at 11 March and is gradually healed. However the degree of the change around 11 March is smaller than that of the station N.YBKH.

Figure 4.7 shows the result of the station N.THGH. This station is near the earthquake fault of the aftershock at North Ibaraki on 19 March with Mw 5.8 (Figure 4.1(b)). One can see that the day of the maximum velocity change is shifted rightward compared to Figure 4.4 and it shows the stepwise transition of the velocity caused by two earthquakes: the earthquake at 11 March caused 0.8% perturbation and that at 19 March caused further 1%. Interestingly, the velocity change at 11 March was smaller than that estimated in N.YBKH and the total change after 19 March show the almost same value to N.YBKH.

Figure 4.8(a) shows the result of the ACF at the station N.IWWH which is near the earthquake fault of the aftershock at South Fukushima on 11 April with Mw 6.8 (Figure 4.1(b)). Since the waveform in the preseismic duration (9 January - 11 March) are much different from the postseismic duration (12 March - 30 June), the correlation coefficient in the stretch analysis show lower values in the pre-seismic duration (Figure 4.8(b)). Consequently the velocity perturbation did not show the jump at 11 March (Figure 4.8(b)). This could be due to the effect of the strong near-surface deformation, the change of the seismicity which are insufficiently removed before autocorrelation and the change of the source characteristics of the ambient noise. Therefore we focused on the dominant event appeared around 2s-2.8s in Figure 4.8(a) and calculate ϵ using this small time window (blue line in Figure 4.8(b)). We could track these events for the duration of 20 February to 30 June. It shows the less stabilized values than the longer time window, however, it shows the velocity drop at 11 March and has the very similar values in the post-seismic duration to the result of the long time window (Figure 4.8(b)). The result clearly show the gradual evolution of the velocity reduction caused by two earthquakes: the Tohoku Earthquake at 11 March and South Fukushima at 11 April.

4.3.3 Spatial variation of the velocity change

The velocity change just after 11 March tends to be very large and the some of the stations stopped observation due to the strong shaking. Furthermore, the velocity is gradually healed as shown in Figure 4.4. In order to show the spatial distribution of the velocity change, therefore, we calculated the difference between the averaged velocity change of two different durations. Figure 4.10 shows the difference of the averaged velocity change for preseismic duration (9 January - 10 March) and postseismic duration (11 March - 30 June). Figure 4.10 is produced after a kriging interpolation. Figure 4.10 shows the trend that the eastern area close to the coast line has the larger velocity reduction than those in the western area. The maximum velocity change are approximately 1.5% in the eastern area. Almost all region show the velocity decrease. Although some area show small velocity increase, we believe these are within the uncertainties.

4.4 Discussion

We estimated the velocity change during 6 month in the duration of the Tohoku Earthquake using the scattered wave retrieved by autocorrelation of ambient noise. The earthquakes produce the enormous change of the stress field. The rock physics model predicts the velocity change depending on the change of the effective pressure due to the opening or closing of the crack (e.g., Toksöz et al., 1976). On the other hand, the strong motion of the seismic wave produced by earthquakes may cause the non-linear behaviour of the elastic properties (e.g., Beresnev and Wen, 1996; Vidale and Li, 2003; Schaff and Beroza, 2004; Peng and Ben-Zion, 2006). We discuss these two reasons for the velocity change estimated in this study.

We compare the estimated temporal change of the velocity to the displacement observed by GPS. The GPS network (GEONET) is operated by the Geospatial Information Authority of Japan (GSI). The displacement by GPS reflects the low frequency change of the stress field. We calculated the surface displacement at 3 GPS stations (Tamaki, Iwaki4 and Satomi, Figure 4.1(b)). The displacement is calculated for each day using 3 component of GPS records from GEONET F3 daily coordinate as the displacement from the reference position at 1 January, 2011. Figure 4.9(a) shows the surface displacement as a length of a displacement vector at Tamakawa. We also show the estimated velocity change at N.YBKH. The displacement shows a sudden change of 150 cm at 11 March and shows postseismic deformation. The time of the sudden displacement well corresponds to the change of the velocity at N.YBKH. If we assume the velocity change is produced by the change of the stress field, the gradual healing of the velocity after 11 March may be interpreted as the relaxation of the stress field after earthquakes (Brenguier et al., 2008). We show the displacement at Iwaki4 and Satomi in Figures 4.9(b) and 4.9(c). Figure 4.9(b) clearly shows the surface displacement by 2 earthquakes at 11 March (160cm) and 11 April (20 cm). They are corresponding to the stepwise transition of the velocity change observed at N.IWWH. The displacement at 19 March was very small (~3cm,Figure 4.9(c)), however, it also corresponds to the stepwise velocity change at N.THGH.

We calculate the static strain change for the survey duration using GPS records. The static strain is derived assuming the constant strain triangle element (e.g., Terada and Miyabe, 1929).

We calculate the strain using the horizontal displacement from the GPS. We show the estimated area strain change derived from the coordinate difference of 1 January 2011 and 29 June 2011 (Figure 4.11). Due to the Tohoku Earthquake, the almost whole survey region experienced dilatation (positive area strain change). The large dilatation are distributed close to the coast line. This is corresponding to the velocity change estimated by the ambient noise (Figure 4.10). The abnormal large dilatation area in Figure 4.11 is a result of the fault activities of two aftershocks at North Ibaraki (19 March) and South Fukushima (11 April). The velocity reduction also show the large value in this area (Figure 4.10).

We compare the estimated velocity change to the spatial distribution of the peak particle velocity recorded during the 3 earthquakes (Figure 4.12). The Kik-net operated by NIED is a strong-motion seismogram network with a vertical array. Almost all Hi-net stations have corresponding Kik-net station at the same depth (Figure 4.12). Since the maximum strain estimated from the acceleration is dependent to a frequency (Beresnev and Wen, 1996), we used the particle velocity as a measure of the maximum strain received during a strong motion of the seismic wave. Therefore, it may show the relative damage to the near-surface rocks due to the strong motion. The distribution of the peak particle particle velocity is obtained from the subsurface receivers of Kik-net after bandpass filtered by 0.1Hz to 10Hz. Figure 4.12 shows the cumulative value of the peak particle velocity recorded at 11 March, 19 March and 11 April in order to compare the averaged velocity change due to these earthquakes.

The spatial distribution of cumulative particle velocity (Figure 4.12) shows similar trend to both of the velocity change (Figure 4.10) and the area strain change (Figure 4.11); the large particle velocity are distributed near the coastline.

We show the crossplot of the averaged velocity change and the estimated area strain change at the near triangle element for the each Hi-net stations (Figure 4.13(a)). Similarly, we show the crossplot of the the velocity change and the observed cumulative peak particle velocity (Figure 4.13(b)). Note that the velocity healing is expected to be non-linear and some of the stations showed the unstabilized values of ϵ for few days after earthquakes. Therefore the comparison with the averaged velocity change including healing process might produce rather scattered distribution on the crossplot (4.13(b)). To compensate this, we choose the stations which showed the clear and stabilized velocity decrease for only the Tohoku Earthquake and compare picked ϵ and peak particle velocity at 11 March (Red dots in Figure 4.13(b)). Both figures (Figure 4.13(a) and 4.13(b)) show clear positive correlation of the velocity decrease (positive epsilon). The abnormal station (N.THGH, arrow in Figure 4.13(a)) show the velocity decrease even though these area experienced compaction (negative strain change). The compaction is a result of the fault activity of two aftershocks (Figure 4.11). On the other hand, the area near the station N.THGH experienced large particle velocity and it is distributed in the normal trend (arrow in Figure 4.13(b)).

This observation suggests that the velocity change estimated in this study is affected by the strong motion at the near-surface, possibly corresponding to the damage received at the near-surface rocks around 200m depth. However, the velocity change in this study is smaller than that from Nakata and Snieder (2011) who estimate the shear-surface velocity decrease ($\sim$ 5%) for

few hundred meter depth by crosscorrelating earthquakes observed at the vertical array of Kik-net. Furthermore, we show that the later arrival events has smaller velocity change (Figure 4.5) and the strain change shows a correlation to velocity change (Figure 4.13(b)). The fact that we focus on the scattered wave with the travel time of 2 s to 10 s indicates that the maximum raypath of scattered wave is approximately 25km considering the average P-wave velocity as 5000 m/s. These results, therefore, support that our velocity change contains the deeper information and the those due to the release of the enormous stress at the deep underground.

4.5 Conclusion

We estimated the velocity change during 6 month in the duration of the 2011 off the Pacific coast of Tohoku Earthquake (the Tohoku Earthquake) in Japan using scattered wave retrieved by autocorrelation. The survey area includes the Fukushima and Ibaraki prefectures where two large aftershocks with surface deformation are observed.

We produced autocorrelation function (ACF) of the noise data at 58 stations and estimate the velocity change. The estimated velocity decrease was up to 2% in the Fukushima prefecture where is close to the hypocenter of the Tohoku Earthquake. The estimated temporal change of the velocity shows the logarithmic healing after earthquake. The result correlates well to the temporal changes of the displacement by GPS network for two aftershocks as well as the Tohoku Earthquake. The spatial distribution of the velocity change shows a correlation to both the static strain change derived from GPS records and the spatial distribution of the peak particle velocity experienced during the earthquakes.

The area which experienced compaction and strong motion showed velocity decrease. This result suggests that the velocity change of this study is affected by a strong motion at the near-surface, possibly corresponding to the damage to the near-surface rocks. Our velocity change is smaller than those from the another study focusing on the near-surface, the later arrival event has smaller velocity change, and the crossplot shows a correlation of velocity change to the strain change. These observations suggest that our velocity change also contains the deeper information possibly for the release of the enormous stress associated with the earthquakes.

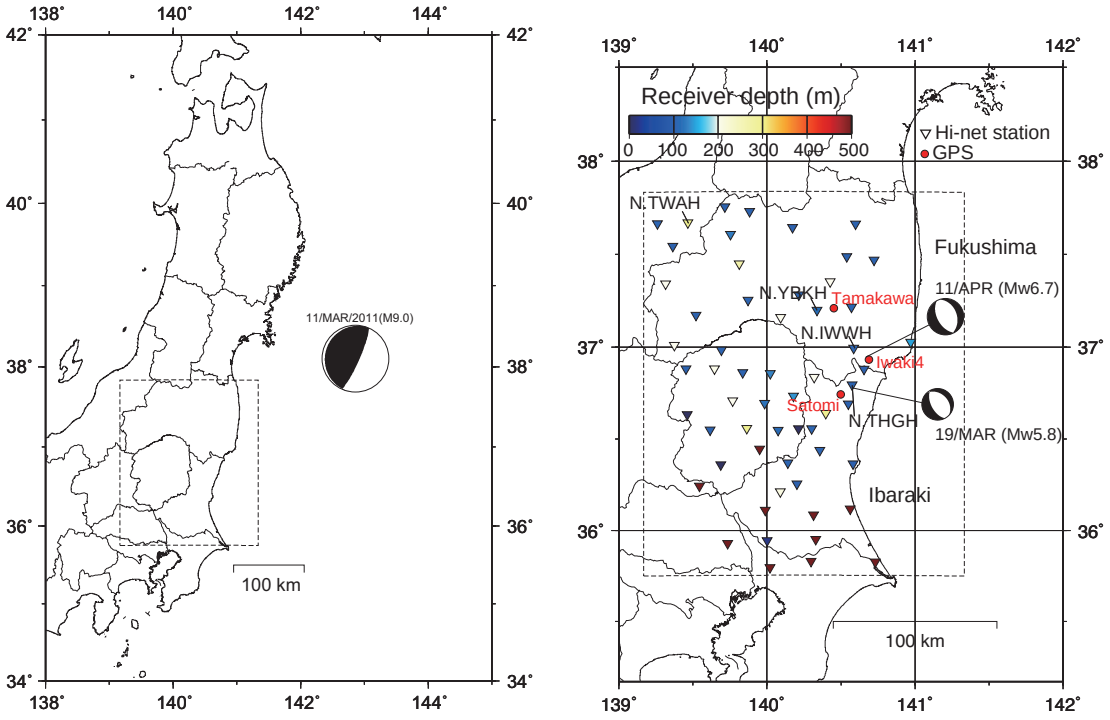

Figure. 4.1: (a) Eastern Japan and hypocenter of the Tohoku Earthquake on 11 March 2011. (b) Survey area. 58 Hi-net stations are distributed. Color of station shows the station depth clipped by 500m. Three GPS stations for the comparison with the surface deformation are indicated. Two aftershocks with surface deformation occurred at North Ibaraki (Mw 5.8, 19 March) and South Fukushima (Mw 6.7, 11 April).

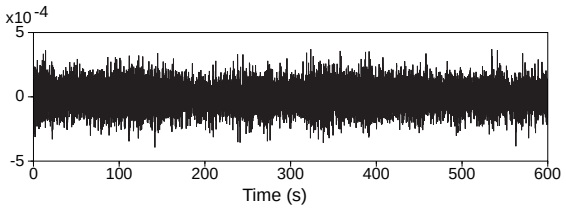

Figure. 4.2: Preprocessed vertical component of the data at the station N.YBKH.

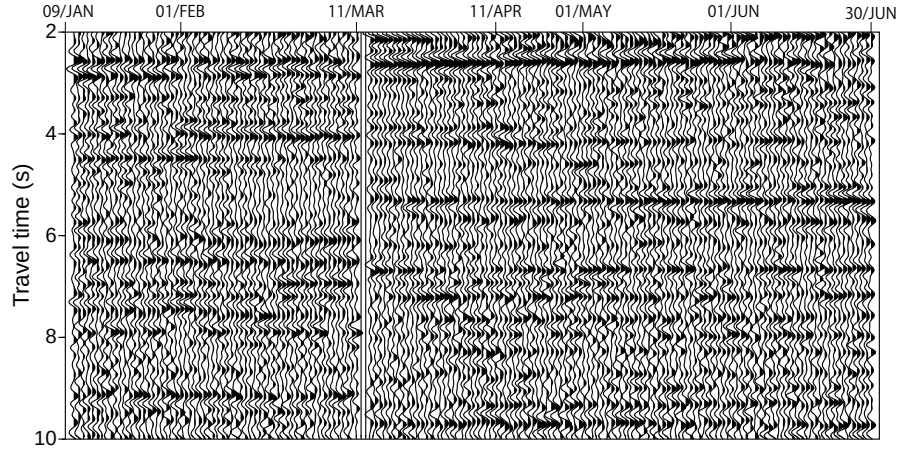

Figure. 4.3: ACF at the station N.YBKH after bandpass filtered for 2Hz-5Hz.

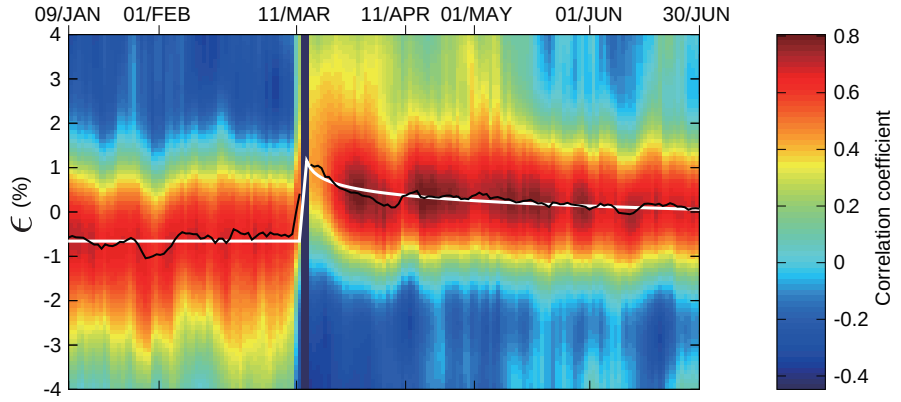

Figure. 4.4: Temporal variation of the velocity change (ϵ) and the correlation coefficient of stretching interpolation technique at the station N.YBKH.

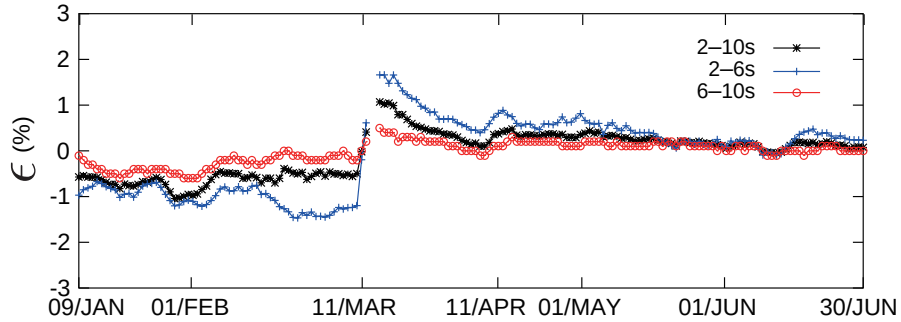

Figure. 4.5: Calculated velocity change at the station N.YBKH for the different time windows.

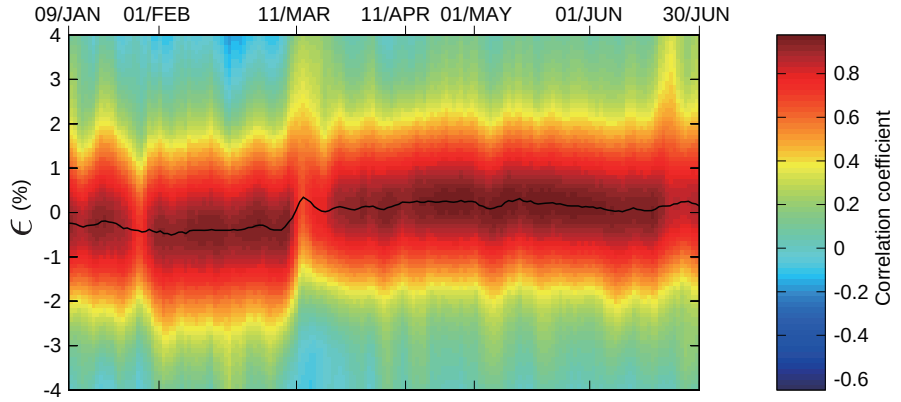

Figure. 4.6: Temporal variation of the velocity change (ϵ) and the correlation coefficient of stretching interpolation technique at the station N.TWAH.

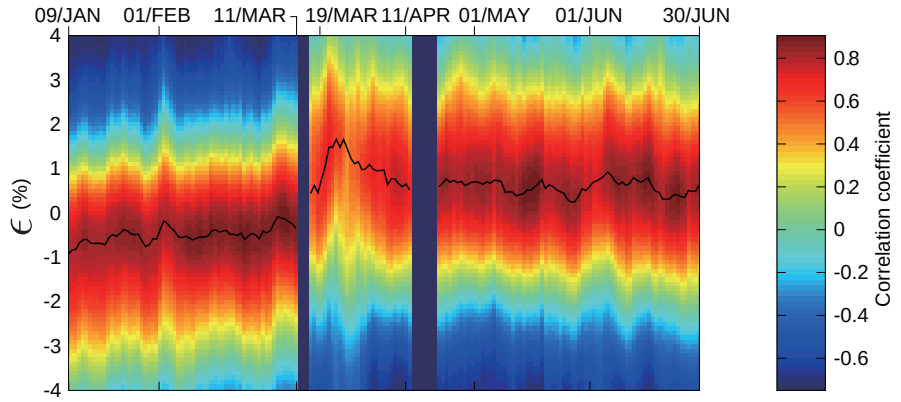

Figure. 4.7: Temporal variation of the velocity change (ϵ) and the correlation coefficient of stretching interpolation technique at the station N.THGH.

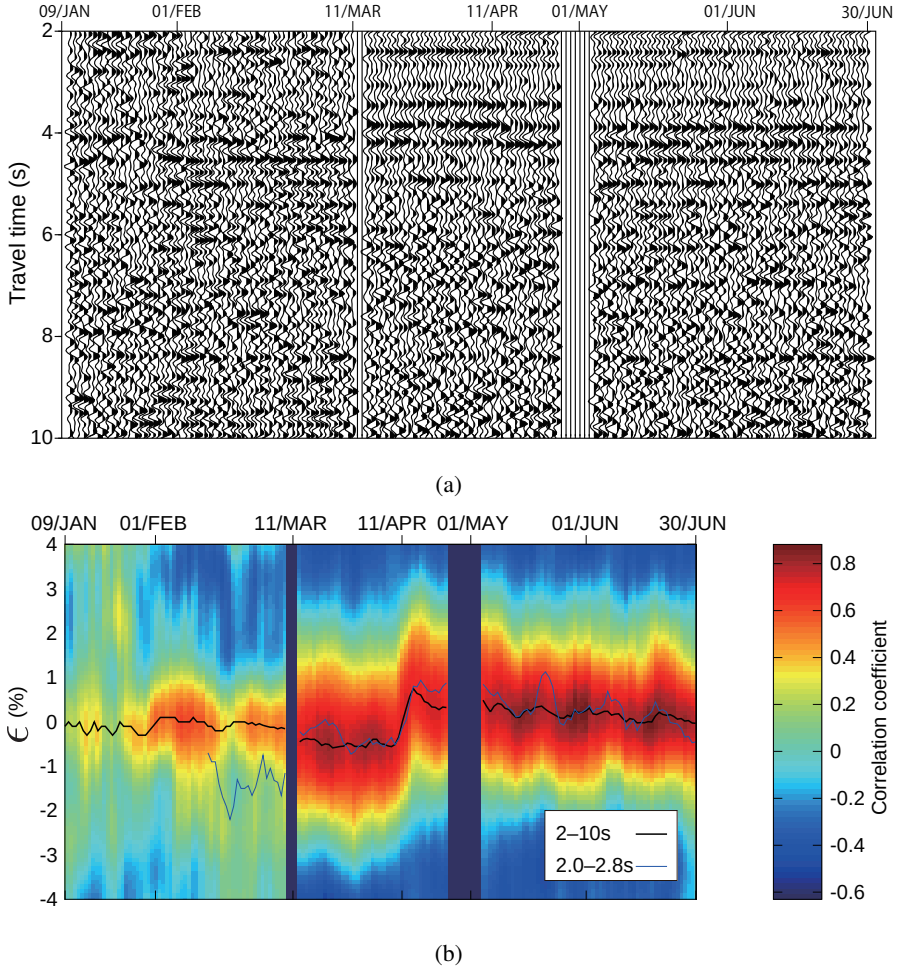

Figure. 4.8: (a) ACF at the station N.IWWH. (b) Temporal variation of the velocity change (ϵ) and the correlation coefficient of stretching interpolation technique at the station N.IWWH. Blue line shows the result using the smaller time window.

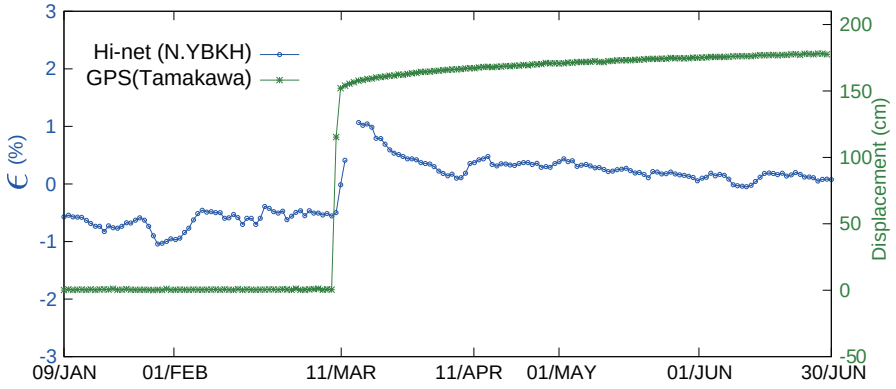

(a)

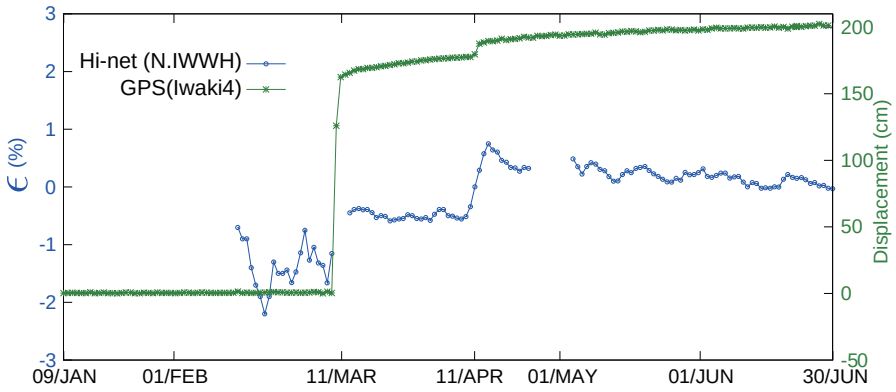

(b)

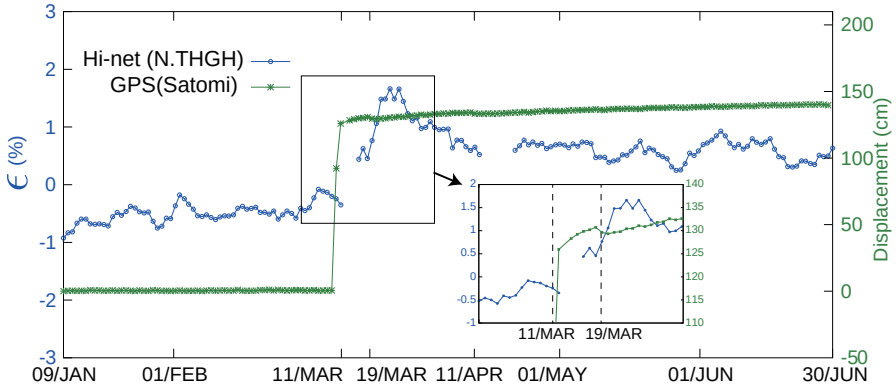

(c)

Figure. 4.9: Comparison of the velocity change and the displacement derived from GPS. (a) GPS at Tamakawa and Hi-net station N.YBKH. (b)GPS at Iwaki4 and Hi-net station N.IWWH. (c) GPS at Satomi and Hi-net station N.THGH.

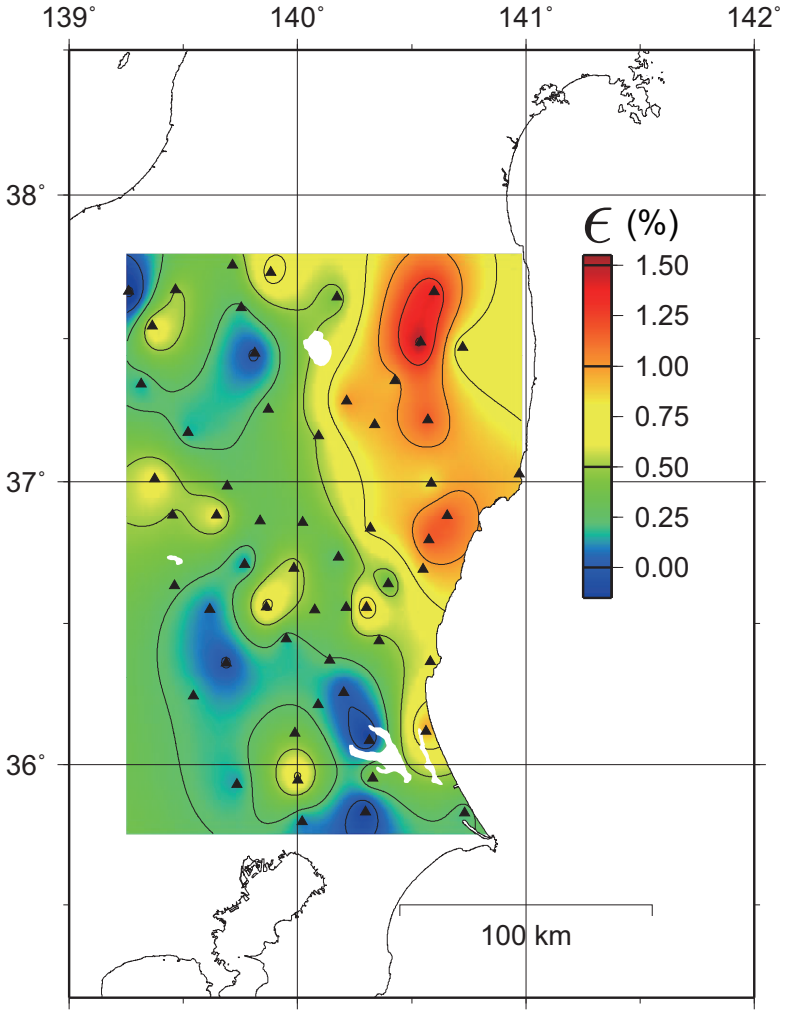

Figure. 4.10: Averaged spatial distribution of the velocity change between the pre-seismic (9 January to 10 March) and post-seismic (11 March to 30 June) duration.

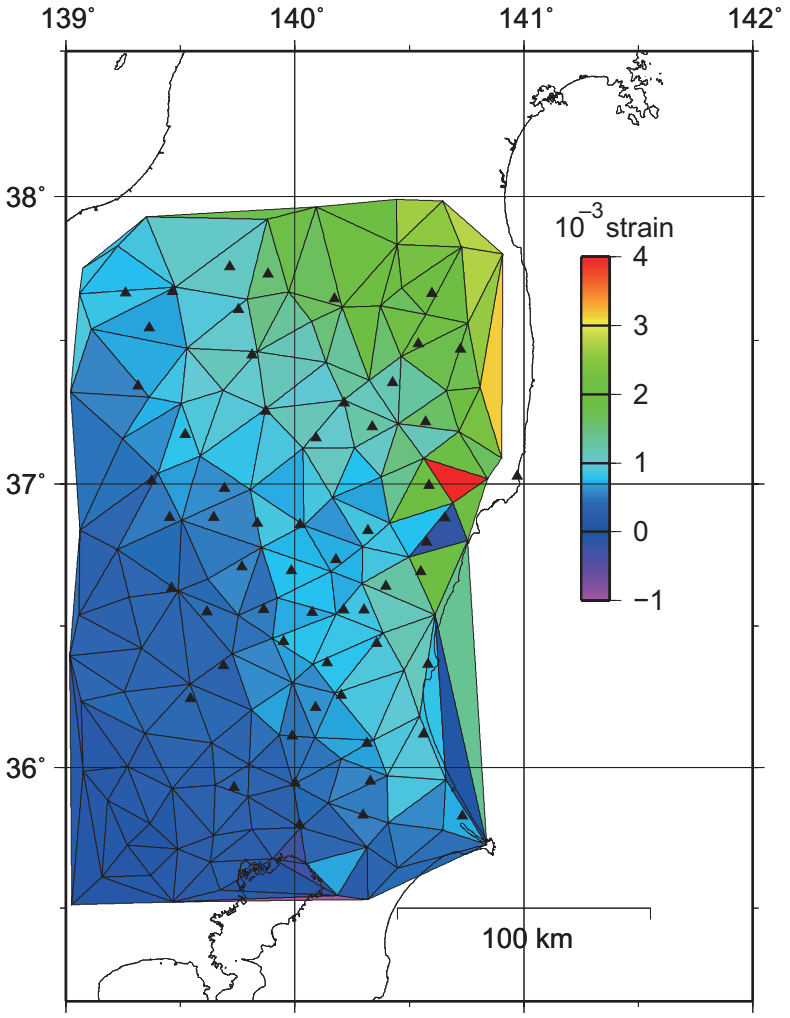

Figure. 4.11: Static area strain change derived from GPS records. Each apex of the triangle elements is GPS station. The strain is calculated from the coordinate difference of 1 January 2011 and 29 June 2011.

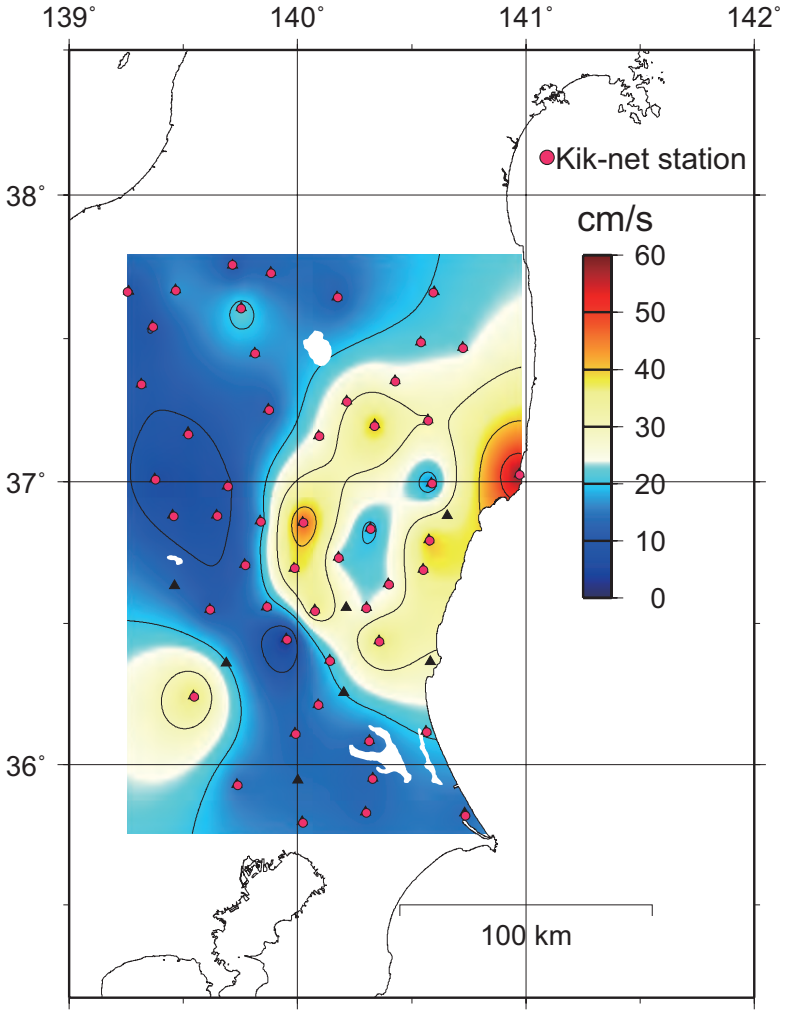

Figure. 4.12: Spatial distribution of the cumulative peak particle velocity observed for three earthquakes (11 March, 19 March and 11 April) by Kik-net seismic network.

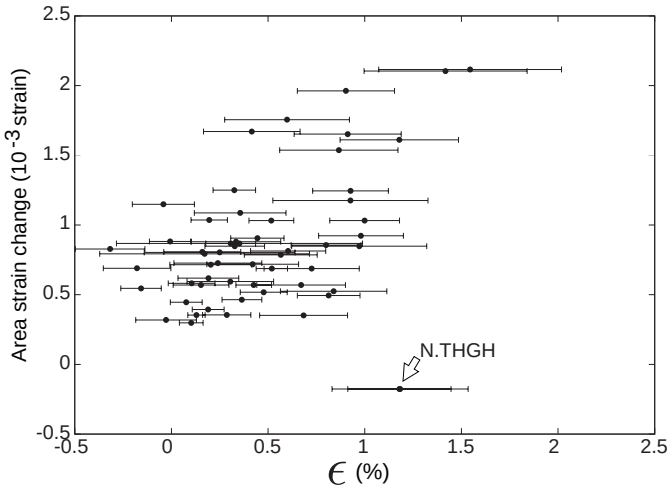

(a)

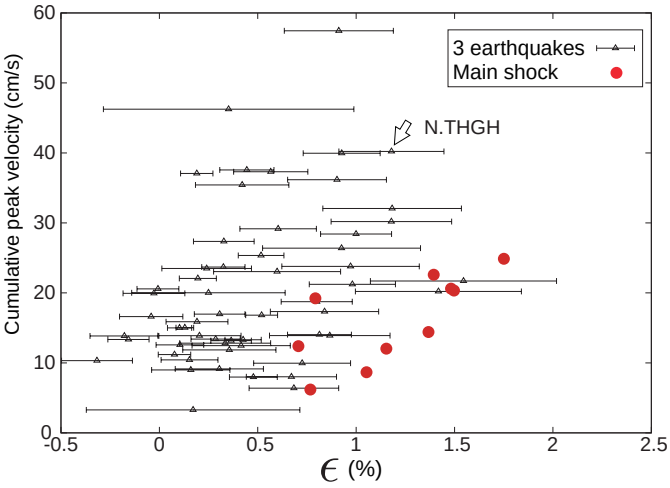

(b)

Figure. 4.13: (a) Crossplot for the averaged velocity change and the area strain change. (b)Crossplot for the averaged velocity change and the cumulative peak particle velocity recorded at three earthquakes. Red dots show the comparison of picked velocity change and the peak particle velocity for the Tohoku Earthquake. Arrows show station N.THGH. The standard deviation is calculated from the velocity change for pre-seismic and post-seismic duration.

5 Interpretation of the effect of source-receiver configuration for Seismic interferometry by Multidimensional deconvolution using singular-value decomposition

5.1 Introduction

Seismic interferometry (SI) retrieves new seismic wavefield from the crosscorrelation (CC) of observed wavefields (e.g. Curtis et al., 2006; Schuster, 2009). The source and receiver positions of retrieved wavefield are specified from receiver positions of observed wavefield. The multidimensional deconvolution (MDD) method (e.g. Wapenaar et al., 2011) is an alternative approach to CC method and is based on the convolution-type reciprocity. The MDD method is developed to overcome the limitations of CC method and is valid for dissipative medium, compensates for the difference of source spectrums and is valid for irregular source distributions. The MDD method is applied e.g., to the retrieval of surface waves (Wapenaar et al., 2010), electromagnetic surveys (Wapenaar et al., 2008a), and Virtual Source method (van der Neut et al., 2010). The MDD method contains the inverse problem which is represented by the convolution relation. We adopted singular-value decomposition (SVD) to stabilize the solution of inverse problems and successfully retrieved crosswell wavefield from VSP data observed at the two vertical wells (Minato et al., 2011). The source distribution becomes the most important factor for applications of SI and dominates the amount of useful information for retrieval of the new wavefield by SI in the observed data. Therefore, the evaluation of source distribution is crucial when we design the experiments. Here, we show that introducing SVD into MDD enables us to evaluate source-receiver distribution of the MDD using the quantity which represents the characteristics of inverse problems.

5.2 MDD using Singular-value decompition

The SI by MDD retrieves wavefield by solving inverse problems represented by convolution-type reciprocity. The convolution relation (Wapenaar and van der Neut, 2010) we used is represented as follows after Fourier transformation,

$$\hat{G}(\mathbf{x}_R, \mathbf{x}_S, \omega) = \int_{\mathbb{S}_0} \hat{\tilde{G}}_d(\mathbf{x}_R, \mathbf{x}, \omega)\hat{G}^{in}(\mathbf{x}, \mathbf{x}_S)d^2\mathbf{x}. \tag{5.1}$$

where $\hat{G}$ is a scalar Green' function. The left hand side of equation 5.1 indicates the response at $\mathbf{x}_R$ from the physical source at $\mathbf{x}_S$. The integrand of the right hand side is a multiplication of an objective wavefield $\hat{\tilde{G}}_d(\mathbf{x}_R, \mathbf{x}, \omega)$ and actual wavefield $\hat{G}^{in}(\mathbf{x}, \mathbf{x}_S)$ in the frequency domain. Virtual sources of the objective wavefield $\hat{\tilde{G}}_d(\mathbf{x}_R, \mathbf{x}, \omega)$ are along in the integration domain $\mathbb{S}_0$. Note that equation 5.1 is derived after several assumptions such as, Sommerfeld condition (the domain $\mathbb{S}_0$ has an infinite length), far-field assumption, and $\hat{G}^{in}$ represents only inward-propagating waves from sources (Wapenaar and van der Neut, 2010). The objective function has dipole source responses as $\hat{\tilde{G}}_d \approx \mathbf{n}\dot{\nabla}\hat{\tilde{G}}$. The equation 5.1 for the objective function $\hat{\tilde{G}}_d$ is hold for the different source positions $\mathbf{x}_S$. We consider multiple source positions and replace the integral by a summation over the regularly distributed receivers along $\mathbb{S}_0$ of the finite length. We obtain following matrix relation,

$$\mathbf{p}_A = \mathbf{P}_B\mathbf{G} \tag{5.2}$$

where $\mathbf{p}_A$ is a column vector containing observed wavefield $\hat{G}$ at $\mathbf{x}_R$ from multiple sources $\mathbf{x}_S$. A matrix $\mathbf{P}_B$ contains observed wavefield $\hat{G}^{in}$ at receivers on the integral surface $\mathbb{S}_0$ from multiple sources. A column vector $\mathbf{g}$ contains objective wavefield $\hat{\tilde{G}}_d$. The $\mathbf{P}_B$ matrix is formed by the observed wavefield and we call this matrix as the Incident Field Matrix (IFM). We estimate objective wavefield $\mathbf{g}$ by solving inverse problems represented in equation 5.2. Equation 5.2 implies that the stable and unique estimation of $\mathbf{g}$ requires observation from the sources that are sufficiently widely distributed. However for practical application, the number of sources and their distribution are limited. Therefore equation 5.2 becomes an ill-posed problem. In order to overcome these problems, we adopt Moore-Penrose pseudo-inverse (Golub and van Loan, 1983) as follows,

$$\mathbf{g}^{est} = \mathbf{P}_B^{+}\mathbf{p}_A \tag{5.3}$$

$$= \mathbf{V}\begin{pmatrix} \mathbf{\Delta}_r^{-1} & \mathbf{0} \\ \mathbf{0} & \mathbf{0} \end{pmatrix}\mathbf{U}^{*}. \tag{5.4}$$

The matrix $\mathbf{P}_B^{+}$ indicates Moore-Penrose pseudo-inverse of IFM, and matrices $\mathbf{V}$, $\mathbf{U}$ and $\mathbf{\Delta}$ can be obtained by applying SVD to IFM as,

$$\mathbf{P}_B = \mathbf{U}\begin{pmatrix} \mathbf{\Delta}_r & \mathbf{0} \\ \mathbf{0} & \mathbf{0} \end{pmatrix}\mathbf{V}^{*}, \tag{5.5}$$

where r indicates the number of rank of IFM.

The data resolution matrix and model resolution matrix (Menke, 1989) can be represented using SVD matrices as,

$$\mathbf{N} = \mathbf{U}\mathbf{U}^{*}, \tag{5.6}$$

$$\mathbf{R} = \mathbf{V}\mathbf{V}^{*} \tag{5.7}$$

5.3 Numerical modeling results

5.3.1 Source distribution and Rank of IFM

We numerically simulate wavefield and investigate the relation between the source distribution and rank of IFM. For brevity we consider two dimensional problems with homogeneous medium. The inverse problems of MDD are constructed at each frequency. Therefore we consider monochromatic response. The Green's function is given as,

$$G(d) = (8\pi kd)^{-0.5} e^{i(kd+\pi/4)} \tag{5.8}$$

where d indicates the distance from source and $k = \omega/c$. Hereafter we calculate the response at 50 Hz with 1500 m/s propagating velocity.

We install 101 sources $\mathbf{x}_S$ regularly distributed along horizontal line with the length of 400m at Z=0 (Figure 5.1(a)). We assume integral surface $\mathbb{S}_0$ as a line parallel to x-axis, and install 41 receivers regularly distributed along $\mathbb{S}_0$ with the length of 400m at Z=300m. These receiver positions will be VS positions after SI. Furthermore we install other 21 receivers $\mathbf{x}_R$ along vertical line with the length of 100m at X=0m. Note that installing multiple receivers $\mathbf{x}_R$ replaces the vectors appeared in equation 5.2 by the matrices whose columns correspond to the different receiver positions of $\mathbf{x}_R$. However this does not change the IFM. After constructing IFM, we apply SVD (complex value SVD in this case) and determine the rank of IFM from obtained singular-values. We defined the rank of IFM as the number of singular-values i that corresponds to 99% cumulative contribution as,

$$S_i = \frac{\sum_j^i \lambda_j}{\sum_j \lambda_j} * 100, \tag{5.9}$$

where λ_j indicates j-th singular-value. Estimated rank of IFM using equation 5.9 was 16 (Figure 5.2). We retrieve objective wavefield using equation 5.4. Figure 5.3 shows the comparison between true and retrieved wavefield (only phases are shown). One can see that the phases from the virtual sources near the center of $\mathbb{S}_0$ are better retrieved than the virtual sources at the edge of $\mathbb{S}_0$ (the domain enclosed by dashed white line in Figure 5.3(b)). This can indicate that in our source distribution, the receivers located around the center of $\mathbb{S}_0$ contain much raypath that correspond to the desired wavefield (gray hatched area in Figure 5.1(a)).

The fact that estimated rank of IFM was not full rank implies that the IFM constructed by the observed records can be represented using less number of data by basis conversion. In other words, the observed records at $\mathbb{S}_0$ contain redundant records. We investigate the density of source distribution assuming it as one of the reason of this data redundancy. We numerically model again using less number of sources.

We install the sources at the same spatial range of Figure 5.1(a) but reduce the number of sources to 18. We show the singular-values obtained from IFM that is constructed using this sparse source distribution (Figure 5.4(a)). Since the total energy in the observation system decreased, the absolute value of singular-values also decreased from that in the dense source case.

Furthermore, the maximum rank of IFM is 18 because of $r \leq min(m, n)$ where m and n indicate the number of sources and the number of receivers respectively. However, the structure of singular-values and estimated rank are almost identical to those of the dense source distribution. Furthermore, the retrieved wavefield (Figure 5.4(b)) does not change from the dense source distribution (Figure 5.3(b)). Therefore, the dense (101) sources can be replaced by the sparse (18) sources, suggesting that the more effective source distribution can be determined by investigating the rank of IFM using SVD.

Here, we choose the reduced number as 18 by calculating several source distribution as we keep the same length of the source array and change the increment of source position. When we reduced the number of sources as less than 15, the IFM is full rank matrix but retrieves inferior wavefield since the rank is less than 16. This result suggests that to retrieve better wavefield we find the source distribution for specified source length which shows maximum rank. These sources will be installed so that the receivers are well illuminated.

5.4 Effect of presence of scatterers

We use the observation system which has localized source distribution (Figure 5.1(b)). We install the 101 sources that are regularly distributed along the horizontal line of the length of 200m at Z=0m. The singular-values obtained from IFM (Figure 5.5(a)) show that the rank determined by the criteria of equation 5.9 is reduced from the wider source distribution (Figure 5.2). Furthermore, the wavefield retrieved by MDD (Figure 5.5(b)) show that only the domain enclosed by dashed white line in Figure 5.5(b) retrieves true response. These can be related to the narrower illuminated area from sources (gray hatched area in Figure 5.1(b)) as in the case of previous section.

We use same source distribution but now install the 301 point scatterers randomly distributed in the area at the right side of the model (dots in Figure 5.1(b)). These scatterers are located in the box of 100m x 100m. Since our wavelength is 30m, these scatterers produce strong reflection and are expected to increase the illumination of receivers from right side of the model. Here we simulate the wavefield as the summation of direct wave with background velocity and primary scattering wave without considering the interaction between scatterers. The result of MDD shows that the rank of IFM slightly increase (Figure 5.6(a)), and better retrieve wavefield indicated by white dashed line in Figure 5.6(b) than those without scatterers (Figure 5.5(b)). This indicates that the presence of scatterers improve the illumination of receivers and also improve the rank of IFM.

5.4.1 Evaluation of retrieved wavefield by SVD matrices

We consider the matrices obtained by SVD of IFM. The model resolution matrix which is the weight matrix applied to the true model is related to the SVD matrices (equation 5.7). If we have a sufficient observation which uniquely retrieves true wavefield $\mathbf{g}^{true}$, the estimated wavefield $\mathbf{g}^{est}$ conforms as $\mathbf{g}^{true}$. Therefore the model resolution matrix $\mathbf{R}$ is close to an identity matrix when

the estimated wavefield is close to the true wavefield. This can be inferred from the fact that the representation of the model resolution matrix is identical to the projection matrix between the data($\mathbf{p}_A$)-space and the model($\mathbf{g}$)-space (Lawson and Hansen, 1974).

We use the observation system which has localized source distribution (Figure 5.1(b)) without scatterers. Figure 5.7(a) shows absolute values of model-resolution matrix $\mathbf{R}$ calculated from equation 5.7. Figure 5.7(a) shows the sharpness around the diagonal component is smooth in the higher model number. This indicates that the wavefields whose virtual sources at the right side in Figure 5.1(b) are blurred. This also corresponds to the result that the estimated wavefield does not retrieve the virtual source located at the right side or higher model number (Figure 5.5(b)). Furthermore, the diagonal components of R (Figure 5.7(b)) show how much the true model is involved in the estimated model. This also shows the higher model number have lower contribution of true model. Note that the both ends in Figure 5.7(b) show large value, however, adequacy for the model at the both ends cannot be discussed because we assumed the finite length of $\mathbb{S}_0$.

5.5 Conclusion

We show that introducing SVD into MDD gives us the analytic method using the quantity which represents the characteristics of inverse problems such as the rank and resolution matrix. We numerically simulate two dimensional scalar wavefield and investigate the relation between the rank of the observation matrix (IFM) and the density of source distribution. The result shows that the sparse source distribution does not change the rank of IFM and also does not change the reliability of retrieved wavefield by MDD when the spatial length of the source array is identical. Therefore, the more effective source distribution can be determined by investigating the rank of IFM. We evaluate the projection matrix constructed by the matrices from SVD (model resolution matrix) using the data whose sources are spatially localized. The ambiguity of the model inferred from model resolution matrix showed the same trend with the discrepancy of the estimated wavefield from true wavefield. Therefore the evaluation of the reliability of the estimated model could be possible by evaluating matrices obtained from SVD. This information becomes crucial when we design the seismic experiments for MDD-based approach.

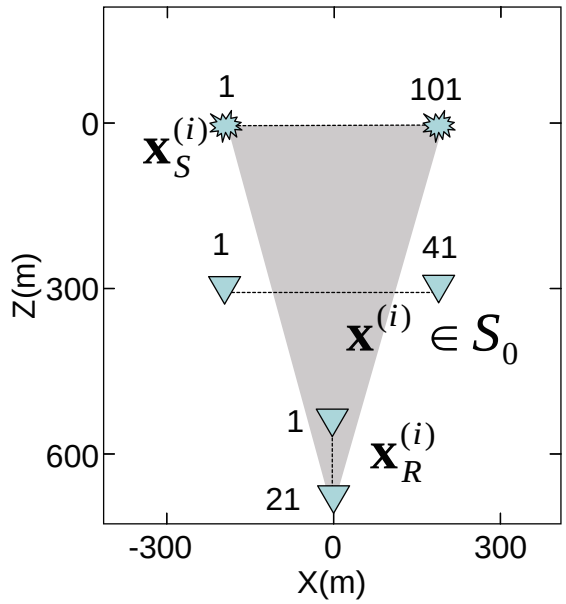

(a)

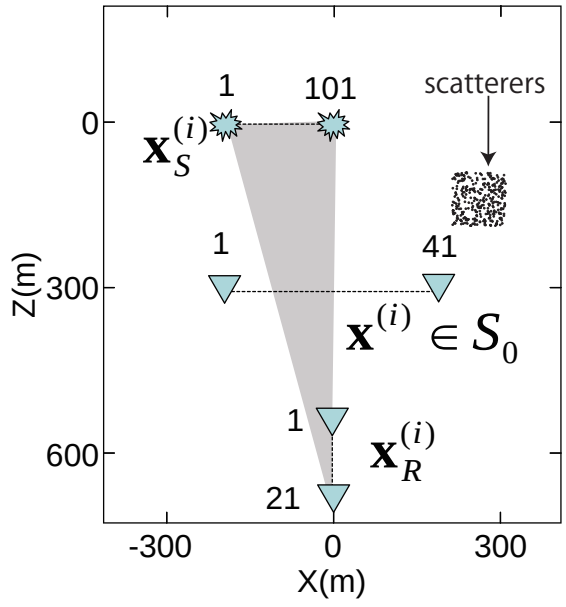

(b)

Figure. 5.1: (a) The source-receiver configuration for numerical modeling. (b) Localized source distribution. Dots show the point scatterers.

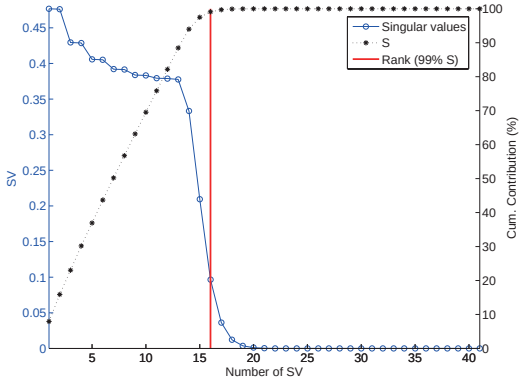

Figure. 5.2: Singular-values of IFM, cumulative contribution and determined rank.

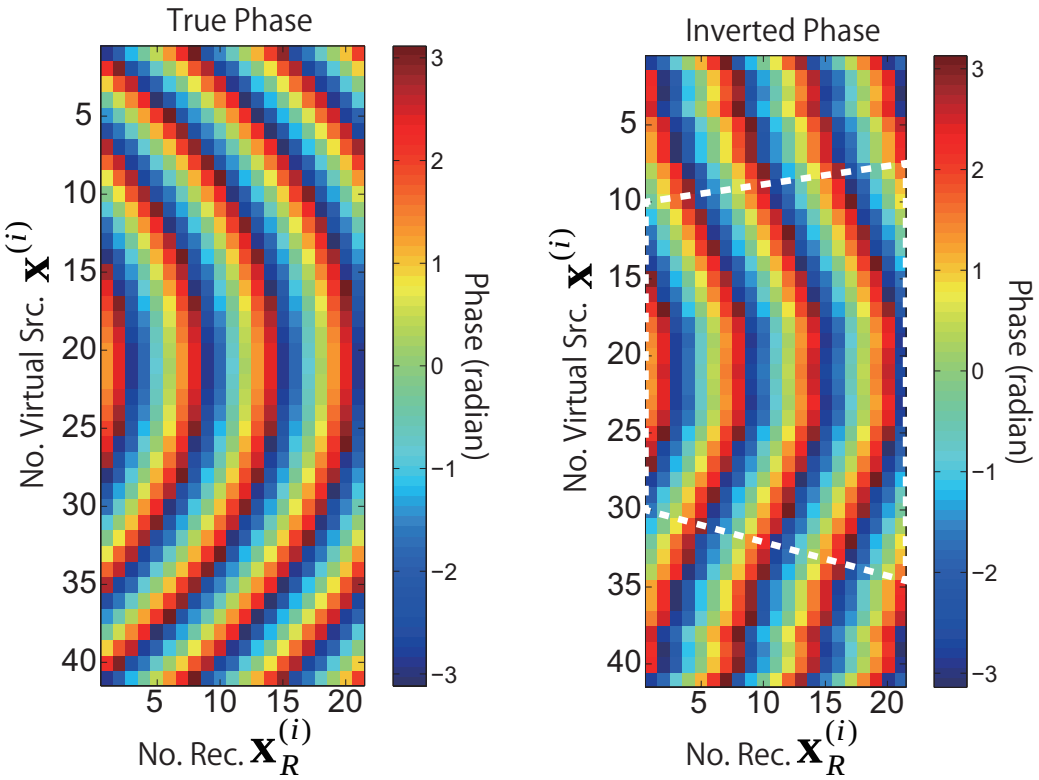

(a) (b)

Figure. 5.3: The phase from (a) true wavefield (b) retrieved wavefield by MDD. The row and the column indicate (virtual) source number and the receiver number respectively. The dashed white line indicates the area that the MDD better retrieved true phase.

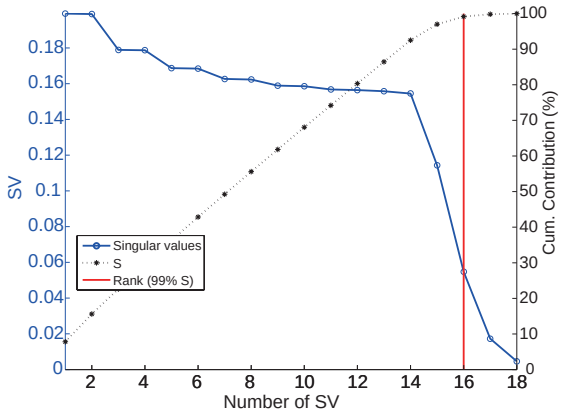

(a)

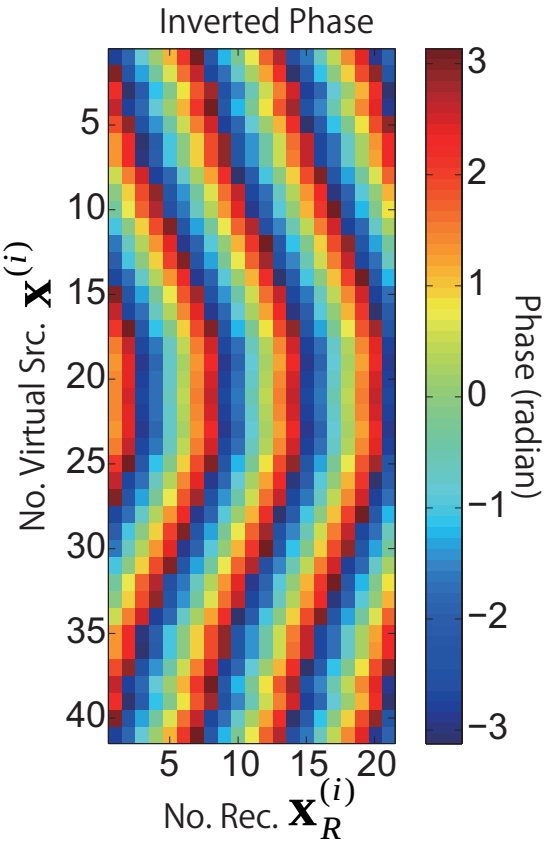

(b)

Figure. 5.4: (a) The singular-values, cumulative contribution and determined rank using sparse source distribution. (b) Estimated wavefield (phase) by MDD using sparse source distribution.

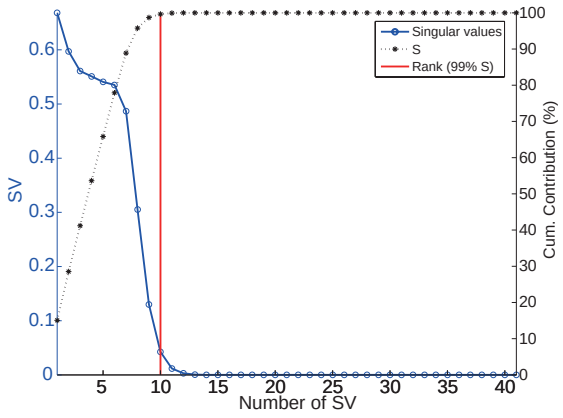

(a)

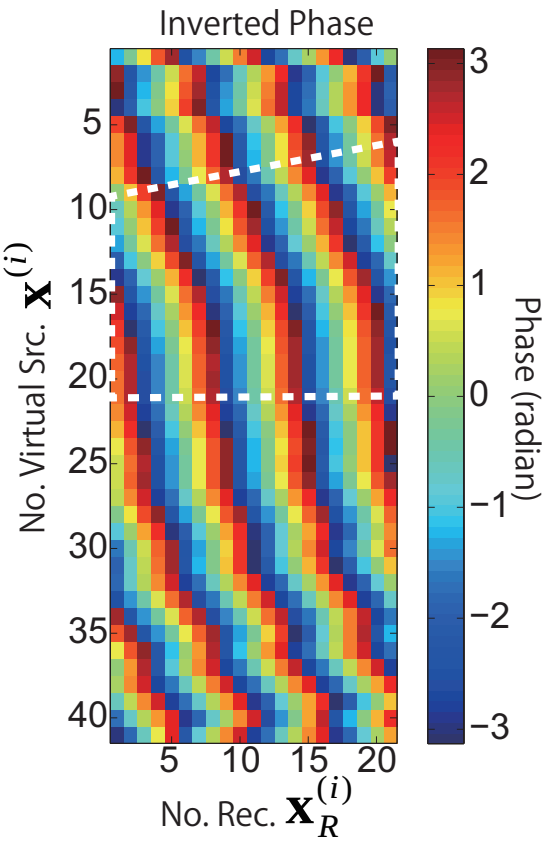

(b)

Figure. 5.5: (a) The results using localized source distribution without scatterers in Figure 5.1(b). (b) Estimated wavefield (phase) by MDD.

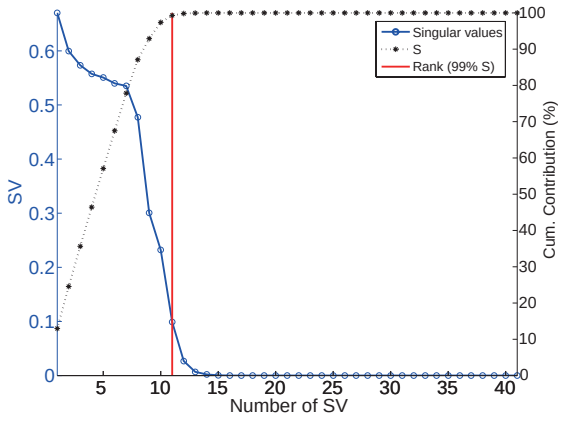

(a)

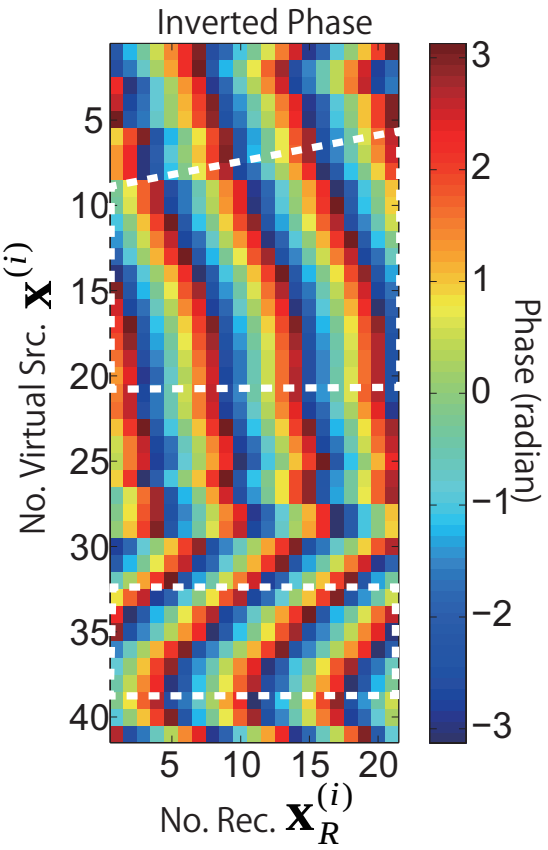

(b)

Figure. 5.6: (a) The results using localized source distribution with scatterers. (b) Estimated wavefield (phase) by MDD.

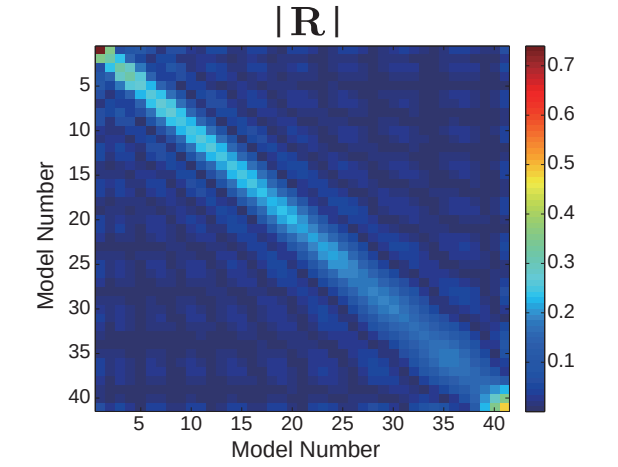

(a)

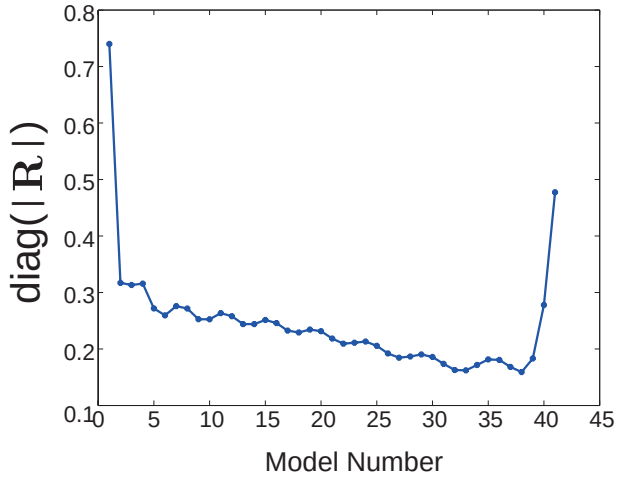

(b)

Figure. 5.7: (a) The absolute value of model resolution matrix $\mathbf{VV}^*$. (b) Its diagonal components. Model number corresponds to the numbered receiver positions at integral domain in Figure 5.1.

6 Seismic interferometry using multidimensional deconvolution and crosscorrelation for crosswell seismic reflection data without borehole sources

6.1 Introduction

Seismic interferometry (SI) can be used to retrieve pseudo seismic data between receivers. This is typically achieved by crosscorrelating observed wavefields. The concept of SI finds its origin in a paper from Claerbout (1968). He showed that for a horizontally layered earth, the autocorrelation of passive seismic data from a buried plane-wave source produces a plane-wave reflection response at the free-surface. Since the work of Claerbout, the understanding of this technique has grown remarkably. In the exploration community, Schuster (2001) and Schuster et al. (2004) showed that SI can be applicable not only for buried noise sources, but also for controlled sources. Snieder (2004) also discusses the details of SI by the stationary phase method for a scattering medium. Wapenaar et al. (2002) and Wapenaar (2004) use reciprocity theorems to prove that the crosscorrelation and summation yields the Green's function in 3D inhomogeneous media. Curtis et al. (2006), Larose et al. (2006) and Schuster (2009) give recent overviews of different applications of SI in both exploration and global seismology.

An important advantage of the application of interferometry to seismic exploration is that it allows flexibility of source and receiver configurations. To use SI for exploration, seismic receivers are placed in the vicinity of the exploration target and the wavefields generated by artificial or naturally occurring seismic sources are recorded. When these recorded data are crosscorrelated, one obtains new recordings at the receivers as if originating from one of the receivers that was turned into a virtual source. Since a few years, SI with naturally occurring noise sources has become a standard technique in the global and regional seismology. For example, Shapiro et al. (2005) retrieve surface waves from ambient seismic noise recorded by the USArray network in California and estimate their group velocity. In exploration seismology, where reflection information is desired, application of SI with noise sources has proven more difficult. Only recently, Draganov et al. (2009) retrieved reflection arrivals from ambient seismic noise in Libya and used the retrieved reflections to obtain a pseudo-3D image of the subsurface. SI with active sources has gained much popularity in exploration seismology. An example is the application for the retrieval of direct or scattered surface waves for their subsequent elimination from controlled-source reflection records (Dong et al., 2006; Halliday et al., 2007, 2010). As another example, applications to borehole seismic exploration methods, such as vertical seismic profiling (VSP), are studied (Yu and Schuster, 2006; Jiang, 2006) as well as inverse VSP data (Shiraishi et al., 2008). Furthermore, Bakulin and Calvert (2006) develop a technique to obtain

virtual wavefields whose virtual sources are inside a single deviated borehole by crosscorrelating wavefield observations from controlled sources on the ground surface. They show that this technique removes the effect of the overburden, for example, scattering noise generated in weathered layers. It has been shown that using this approach boundaries of salt domes can be imaged (Willis et al., 2006; Xiao et al., 2006; Hornby and Yu, 2007), and structures underlying complex overburden can be imaged with higher resolution (Bakulin and Calvert, 2006). Mehta et al. (2007) show that the results from this technique can be improved if the crosscorrelation is applied to separated up- and down-going fields.

SI has also been applied to crosswell seismic data for simulation case study (Shiraishi and Matsuoka, 2005; Shiraishi, 2007), laboratory experiment (Torii et al., 2006) and field experiment (Minato et al., 2007; Mehta et al., 2008a, 2010). The conventional crosswell seismic reflection method can produce high-resolution images of subsurface structures between two boreholes when both the seismic sources and receivers are installed in the boreholes (e.g., Harris et al., 1995). The advantages of crosswell seismic surveys over surface seismic surveys are that they provide higher resolution of the target structures, the data are free of surface waves, and the results are affected less by shallow, low-velocity weathered layers. However, conventional crosswell surveys require special downhole vibrator sources that do not damage the borehole walls, and because these borehole sources produce less energy, the width of the survey spread is restricted. SI allows subsurface structures to be imaged from two boreholes without using borehole sources.

Minato et al. (2007) place receiver arrays in two vertical boreholes and use observations of the wavefield generated by surface energy sources to image subsurface structures. In that study, they consider only active sources on the ground surface, as used for conventional VSP surveys. By installing surface sources, the recorded wavefields in the boreholes are dominated by the up-going reflections which are usually used for VSP reflection imaging (Oristaglio, 1985). In the following, we use surface sources because evaluation of the application of crosswell interferometry is simpler if controlled surface sources with known physical properties are used. Furthermore, the use of surface energy sources gives us operational advantages over conventional crosswell surveys. In particular, this method significantly reduces the cost of time-lapse crosswell surveys. Furthermore, the restriction of spread width (distance between boreholes) for the conventional crosswell reflection method using downhole sources can be overcome by using high-energy sources at the surface. There is a large range of potential applications of this technique for long-distance crosswell reflection surveys over vast areas. Nevertheless, the usage of surface sources would bring its inherited limitations, as discussed above, due to the extra propagation of the surface signals to the observation boreholes, especially when a strongly weathered layer is present.

Underlying assumptions for the retrieval of responses between two receivers using crosscorrelation are those of a lossless medium and a homogeneous illumination of the receivers. To overcome these restrictions, it was proposed to use crossconvolution instead of crosscorrelation (Slob et al., 2007; Halliday and Curtis, 2009) or trace deconvolution (Vasconcelos and Snieder, 2008a,b). Wapenaar et al. (2008b) propose a new approach to seismic interferometry that is

based on multidimensional deconvolution (MDD) instead of the conventional crosscorrelation (CC). Wapenaar et al. (2008a) demonstrate that this method is also useful for application to electromagnetic data. The differences between the CC and MDD methods are: (1) MDD is valid in dissipative media, (2) MDD compensates for the source spectrum, (3) MDD could compensate for irregular source arrays, and (4) MDD accounts for the effects of one-sided illumination. Because MDD compensates for the spectrum of the source wavelets, it could potentially result in higher-resolution images than the CC method. Even though the results from the CC method are normally deconvolved for the source spectra after correlation and summation, this deconvolution might not be trivial. Furthermore, when source arrays are irregular, wave amplitudes and traveltimes retrieved by the MDD method better represent the true wavefield than those from the CC method: the amplitudes of the wavefield retrieved by the CC method differ from the true wavefield and the integration of the crosscorrelation results from the irregular source array would result in lower signal-to-noise ratio of the retrieved results (e.g., Snieder et al., 2006; Mehta et al., 2008b; Wapenaar et al., 2008b). On the other hand, the MDD method has also several constraints: (1) MDD requires receiver arrays and therefore MDD cannot be applied to a single receiver configuration, (2) MDD tends to be more CPU intensive than the CC method by array operation, and (3) MDD is possibly unstable because the inversion problem may be ill-conditioned.

Here, we describe the theory of crosswell seismic interferometry by CC and MDD. This is the first application of MDD for crosswell seismic data. Furthermore, we introduce singular-value decomposition (SVD) to stabilize the MDD solution because the source-receiver configuration introduces an ill-posed problem for solving the MDD relationship. Introducing SVD inversion for MDD is a different approach from the damped-least-squares inversion for electromagnetic data (Wapenaar et al., 2008a) and that for seismic data with a surface receiver array (Wapenaar et al., 2008b). We apply the methods to both numerically modeled and field data. The reflection profiles that we retrieve show that the imaged reflection boundaries from CC and MDD agree well with the velocity model.

Seismic Interferometry

6.1.1 Seismic interferometry by crosscorrelation

The governing equation of SI by the CC method is derived from two-way wavefield reciprocity and the principle of time-reversal invariance (Wapenaar and Fokkema, 2006). It is described in the space-frequency domain as

$$2\Re\{\hat{G}(\mathbf{x}_A, \mathbf{x}_B, \omega)\} \approx \frac{2}{\rho c} \oint_{\partial\mathbb{D}} \hat{G}(\mathbf{x}_A, \mathbf{x}, \omega)\hat{G}^*(\mathbf{x}_B, \mathbf{x}, \omega)d^2\mathbf{x}, \tag{6.1}$$

where $\mathbf{x} = (x_1, x_2, x_3)$ is a position vector in Cartesian coordinates, $\hat{G}(\mathbf{x}_A, \mathbf{x}_B, \omega)$ represents the Green's function for a signal of angular frequency ω at receiver $\mathbf{x}_A$ from a source at $\mathbf{x}_B$ and $\hat{G}(\mathbf{x}_B, \mathbf{x}, \omega)$ represents the Green's function at receiver $\mathbf{x}_B$ from a monopole source at $\mathbf{x}$. The asterisk superscript indicates complex conjugation. Multiple sources $\mathbf{x}$ are distributed along an

arbitrarily shaped closed surface $\partial\mathbb{D}$ and integration along this boundary is evaluated. The multiplication of the complex-conjugated Green's function at $\mathbf{x}_B$ with the Green's function at $\mathbf{x}_A$ in the frequency domain, corresponds to a crosscorrelation in the time domain. Therefore, $\hat{G}(\mathbf{x}_A, \mathbf{x}_B, \omega)$ can be retrieved by integrating crosscorrelations of the wavefield observed at receivers $\mathbf{x}_A$ and $\mathbf{x}_B$ along the closed surface $\partial\mathbb{D}$ where sources exist. Note that the interferometric relation 6.1 was obtained from an exact relation after several approximations. Firstly, it was assumed that the medium along and outside $\partial\mathbb{D}$ is homogeneous. Secondly, a far-field approximation was applied to exchange dipole sources in the exact representation with monopole ones. In practical applications, these approximations might lead to (possibly significant) amplitude errors and spurious events.

For application of interferometry to crosswell seismic data, the energy sources that generate the wavefield can be either artificial active sources or natural passive sources. In this study, we consider only active sources on the ground surface, as used for conventional VSP surveys. The use of high-energy surface sources allows the crosswell reflection method to be used for widely separated boreholes. Furthermore, evaluation of the application of crosswell interferometry is simpler if controlled surface sources with known physical properties are used.

For our application of crosswell SI (equation 6.1), we use sources on the ground surface and receivers in the boreholes (Torii et al., 2006; Minato et al., 2007; Mehta et al., 2008a, 2010) as shown in Figure 6.1. Multiple surface sources are sequentially excited and the resultant wavefields are observed at all borehole receivers (Figure 6.1). Here, the Green's function on the left-hand side of equation 6.1 represents the virtual wavefield at well-1, assuming virtual sources at well-2; this is represented by $\hat{G}^L(\mathbf{x}_A, \mathbf{x}, \omega)$ in Figure 6.1. The two Green's functions on the right-hand side of equation 1 represent the observed wavefields at the boreholes. However, in the field we do not measure the Green's function, but measure the pressure field. Therefore, the two Green's functions on the right-hand side of equation 6.1 are changed to pressure fields $\hat{p}$ including the Fourier transform of the wavelet $\hat{S}(\omega)$ of the surface sources (in field measurements this wavelet should also account for the instrument response of the receivers) as

$$\hat{p}(\mathbf{x}_A, \mathbf{x}, \omega) = \hat{S}(\omega)\hat{G}(\mathbf{x}_A, \mathbf{x}, \omega), \tag{6.2}$$

$$\hat{p}(\mathbf{x}_B, \mathbf{x}, \omega) = \hat{S}(\omega)\hat{G}(\mathbf{x}_B, \mathbf{x}, \omega). \tag{6.3}$$

Consequently, we retrieve a response that is convolved with the autocorrelation of the surface source wavelet. Therefore, the Green's function on the left-hand side of equation 6.1 is exchanged for $\hat{C}$ representing a Green's function multiplied by the power spectrum of the surface source wavelet (i.e.,the Fourier transform of the autocorrelation):

$$2\Re\{\hat{C}(\mathbf{x}_A, \mathbf{x}_B, \omega)\} \approx \frac{2}{\rho c}|\hat{S}(\omega)|^2 \oint_{\partial\mathbb{D}} \hat{G}(\mathbf{x}_A, \mathbf{x}, \omega)\hat{G}^*(\mathbf{x}_B, \mathbf{x}, \omega)d^2\mathbf{x}. \tag{6.4}$$

In our case of crosswell geometry, the integration boundary of equation 6.4 does not take the form of a closed surface because the source distribution is localized only on the earth's surface.

The computation procedure can be described as follows. The wavefield $\hat{C}(\mathbf{x}_A, \mathbf{x}, \omega)$, which propagates from one receiver in well-2 ($\mathbf{x}$) to another receiver in well-1 ($\mathbf{x}_A$), can be retrieved

from

$$\hat{C}(\mathbf{x}_A, \mathbf{x}, \omega) \approx \sum_{k=1}^{N} \hat{p}(\mathbf{x}_A, \mathbf{x}_S^{(k)}, \omega)\hat{p}^*(\mathbf{x}, \mathbf{x}_S^{(k)}, \omega), \tag{6.5}$$

where $\hat{p}^*(\mathbf{x}, \mathbf{x}_S^{(k)}, \omega)$ is the complex-conjugated wavefield observed at $\mathbf{x}$ from the k-th surface source, and $\hat{p}(\mathbf{x}_A, \mathbf{x}_S^{(k)}, \omega)$ is the wavefield at $\mathbf{x}_A$ from the k-th surface source. Note that we changed the notations in equation 6.1 from the source position $\mathbf{x}$ in the integral to $\mathbf{x}_S^{(k)}$, and the receiver position $\mathbf{x}_B$ to $\mathbf{x}$. We also skipped the factor $2/\rho c$. To account for the integral of equation 6.4, the correlation products are stacked over the interval of the surface source array with the maximum number of elements N. In the examples that we are showing, we look only at the causal part of $\hat{C}$ in equation 6.5 because, due to the horizontally layered subsurface and ignoring back-scattering, the acausal part of $\hat{C}$ would be retrieved from surface sources to the left of well-1, which we do not have. Equation 6.5 is similar to the virtual source method of Bakulin and Calvert (2006), but in their work, they implement the crosscorrelation of the gated direct field in $\mathbf{x}$ with the full wavefield at $\mathbf{x}_A$ in order to improve the retrieved up-going events. Similarly, Mehta et al. (2007) show that correlation of separated down-going waves in $\mathbf{x}$ with separated up- or down-going waves at $\mathbf{x}_A$ improves the retrieval of events. Gating and/or separating wavefields before crosscorrelation can be regarded as an optional processing of equation 6.5 which is a crosscorrelation between total wavefields.

6.1.2 Seismic interferometry by multidimensional deconvolution

Seismic interferometry by the MDD method is based on one-way reciprocity theory (Wapenaar et al., 2008a). One-way reciprocity refers to the relationship between wavefields or diffusion fields that can be separated into up-going and down-going components. In this study, we consider one-way reciprocity of scalar fields $\hat{p}^+$ and $\hat{p}^-$, which represent down-going and up-going acoustic wavefields, respectively. The one-way reciprocity theorem of the convolution type is represented in the space-frequency domain as follows:

$$\int_{\partial\mathbb{D}_2} \{\hat{p}_A^+\hat{p}_B^- - \hat{p}_A^-\hat{p}_B^+\} d^2\mathbf{x} = \int_{\partial\mathbb{D}_1} \{\hat{p}_A^+\hat{p}_B^- - \hat{p}_A^-\hat{p}_B^+\} d^2\mathbf{x}, \tag{6.6}$$

where $\partial\mathbb{D}_2$ and $\partial\mathbb{D}_1$ represent horizontal boundaries of infinite extent ($\partial\mathbb{D}_1$ lies below $\partial\mathbb{D}_2$). Subscripts A and B in equation 6.6 indicate two independent states, i.e., state A and B could have different source positions and medium parameters. Two assumptions are required for equation 6.6: no sources should be located between the boundaries $\partial\mathbb{D}_2$ and $\partial\mathbb{D}_1$, and the physical parameters of the transmitting medium enclosed by the two boundaries should be identical for states A and B. Substituting the observed wavefield from the actual source-receiver configuration into one of these states, and the desired wavefield (as the unknown function) for the virtual source-receiver configuration into the other state, leads to a relationship that is solved in the MDD method.

For the crosswell geometry, the derivation of the MDD relationship can be accomplished by imagining the configuration described above as rotated over 90°. In this situation, the up-going and down-going waves can be regarded as right-going and left-going waves, respectively.

Furthermore, $\partial\mathbb{D}_2$ and $\partial\mathbb{D}_1$ in equation 6.6 become vertical boundaries. We then substitute the observed acoustic wavefield ($\hat{p}_B^+$ and $\hat{p}_B^-$, or $\hat{p}_B^L$ and $\hat{p}_B^R$ in the new configuration) from the surface sources into state B of equation 6.6, and the acoustic wavefield ($\hat{p}_A^+$ and $\hat{p}_A^-$, or $\hat{p}_A^L$ and $\hat{p}_A^R$ in the new configuration) of the desired crosswell wavefield into state A. Here, we place two receiver borehole positions to correspond with the vertical boundaries $\partial\mathbb{D}_2$ and $\partial\mathbb{D}_1$ (Figure 6.1). Thus, we obtain the following convolution relationship between the observed wavefields from surface sources and the crosswell wavefield that we want to estimate (see Appendix for detail):

$$\hat{p}^L(\mathbf{x}_A, \mathbf{x}_S, \omega) = \int_{\partial\mathbb{D}_2} \hat{G}^L(\mathbf{x}_A, \mathbf{x}, \omega)\hat{p}^L(\mathbf{x}, \mathbf{x}_S, \omega)d^2\mathbf{x}, \tag{6.7}$$

where $\hat{p}^L(\mathbf{x}_A, \mathbf{x}_S, \omega)$ is the acoustic wavefield observed at receiver position $\mathbf{x}_A$ in well-1 from a physical source at the surface at $\mathbf{x}_S$. Similarly, $\hat{p}^L(\mathbf{x}, \mathbf{x}_S, \omega)$ is the acoustic wavefield observed at receiver position $\mathbf{x}$ in well-2 from the same physical source at $\mathbf{x}_S$ (see Figure 6.1). The superscript L indicates decomposed leftword-propagating wavefields. $\hat{G}^L(\mathbf{x}_A, \mathbf{x}, \omega)$ is the function to be retrieved and represents the crosswell Green's function at receiver position $\mathbf{x}_A$ in well-1, assuming that receiver $\mathbf{x}$ in well-2 is the virtual source position. Note that $\partial\mathbb{D}_2$ of equation 6.7 is a 2D surface; however, in practice, our borehole represents 1D boundary in the vertical direction. Therefore we approximate $\partial\mathbb{D}_2$ as a 1D line in the vertical direction at the borehole positions.

MDD processing is usually done in the frequency domain, and an integral is evaluated along all receiver positions in well-2 (equation 6.7). Equation 6.7 states that integrating the product (in the frequency domain) of crosswell Green's functions and observed records at well-2 for all receiver positions ($\partial\mathbb{D}_2$) gives the observed records at well-1. This relationship is exact (assuming a 2D configuration) when the following three conditions are satisfied: (1) $\partial\mathbb{D}_2$ (length of the borehole array at well-2) is of infinite extent, (2) the space to the left of well-1 is non-reflecting (i.e., no wavefields, such as reflections, originate from left of well-1), and (3) the physical source $\mathbf{x}_S$ is located to the right of well-2 (see Appendix for detail). Contrary to the CC method (equation 6.5), MDD needs integration not over sources, but over receivers. This implies that the MDD method has the potential to be applied even for complex irregular source distributions.

Resolving $\hat{G}^L(\mathbf{x}_A, \mathbf{x}, \omega)$ from equation 6.7 requires MDD. If we consider one receiver position in well-1 ($\mathbf{x}_A$) and multiple source positions ($\mathbf{x}_S$) and if we replace the integral by a summation over the receivers of well-2 ($\partial\mathbb{D}_2$), equation 6.7 can be written in a matrix-vector notation as

$$\begin{aligned}\left(\hat{p}^L\left(\mathbf{x}_A, \mathbf{x}_S^{(1)}\right) \dots \hat{p}^L\left(\mathbf{x}_A, \mathbf{x}_S^{(N)}\right)\right) = \\ \left(\hat{G}^L\left(\mathbf{x}_A, \mathbf{x}_1\right) \cdots \hat{G}^L\left(\mathbf{x}_A, \mathbf{x}_M\right)\right)\begin{pmatrix} \hat{p}^L\left(\mathbf{x}_1, \mathbf{x}_S^{(1)}\right) & \dots & \hat{p}^L\left(\mathbf{x}_1, \mathbf{x}_S^{(N)}\right) \\ \vdots & \ddots & \vdots \\ \hat{p}^L\left(\mathbf{x}_M, \mathbf{x}_S^{(1)}\right) & \dots & \hat{p}^L\left(\mathbf{x}_M, \mathbf{x}_S^{(N)}\right)\end{pmatrix},\end{aligned} \tag{6.8}$$

where we made use of Berkhout (1982) matrix-vector notation and the frequency dependency was omitted for brevity. We can rewrite this equation as

$$\hat{\mathbf{p}}_A^L = \hat{\mathbf{g}}^L\hat{\mathbf{P}}_B^L. \tag{6.9}$$

For N sources on the ground surface and M receivers in well-2, $\hat{\mathbf{P}}_B^L$ forms an $M \times N$ matrix whose columns contain $\hat{p}^L(\mathbf{x}, \mathbf{x}_S, \omega)$ for a fixed source position ($\mathbf{x}_S$) and variable receiver positions ($\mathbf{x}$) in well-2 (i.e., this becomes a shot gather), and whose rows contain $\hat{p}^L(\mathbf{x}, \mathbf{x}_S, \omega)$ for a fixed receiver position ($\mathbf{x}$) and variable source positions ($\mathbf{x}_S$) (i.e., a receiver gather). Hereafter, we call the $\hat{\mathbf{P}}_B^L$ matrix the incident field matrix. On the other hand, $\hat{\mathbf{p}}_A^L$ is a $1 \times N$ row vector containing $\hat{p}^L(\mathbf{x}_A, \mathbf{x}_S, \omega)$ for a fixed receiver position ($\mathbf{x}_A$) and variable source positions ($\mathbf{x}_S$). Similarly, $\hat{\mathbf{g}}^L$ is a $1 \times M$ row vector containing $\hat{G}^L(\mathbf{x}_A, \mathbf{x}, \omega)$ for a fixed receiver position ($\mathbf{x}_A$) and variable borehole source positions ($\mathbf{x}$), which is the Green's function that we wish to retrieve.

To estimate the unknown wavefield $\hat{\mathbf{g}}^L$ from equation 6.9, we use matrix inversion so that

$$\hat{\mathbf{g}}^L = \hat{\mathbf{p}}_A^L \left(\hat{\mathbf{P}}_B^L\right)^{-1}, \tag{6.10}$$

where $\left(\hat{\mathbf{P}}_B^L\right)^{-1}$ is the generalized inverse of $\hat{\mathbf{P}}_B^L$ (Menke, 1989). Equation 6.10 shows that if surface sources have different wavelets at different positions, e.g.,

$$\hat{p}^L(\mathbf{x}_A, \mathbf{x}_S^{(k)}, \omega) = \hat{S}(\mathbf{x}_S^{(k)}, \omega)\hat{G}^L(\mathbf{x}_A, \mathbf{x}_S^{(k)}, \omega), \tag{6.11}$$

MDD implicitly accounts for them and retrieves the Green's function. Equation 6.7 implies that stable estimation of $\hat{G}^L(\mathbf{x}_A, \mathbf{x}, \omega)$ requires observation of $\hat{p}^L(\mathbf{x}_A, \mathbf{x}_S, \omega)$ and $\hat{p}^L(\mathbf{x}, \mathbf{x}_S, \omega)$ from sources that are sufficiently widely spread. However, for practical application the number of sources is finite and their distribution is limited, so equation 6.10 could become an ill-posed problem and make it difficult to estimate $\hat{\mathbf{g}}^L$ uniquely. Therefore, Wapenaar et al. (2008b) stabilize the generalized inverse $\left(\hat{\mathbf{P}}_B^L\right)^{-1}$ by using damped-least-squares inversion as follows:

$$\left(\hat{\mathbf{P}}_B^L\right)^{-1} = \left(\hat{\mathbf{P}}_B^L\right)^{\dagger} \left[\hat{\mathbf{P}}_B^L \left(\hat{\mathbf{P}}_B^L\right)^{\dagger} + \epsilon^2 \mathbf{I}\right]^{-1}, \tag{6.12}$$

where ϵ is Tikhonov's regularization parameter (Morozov et al., 1984), which stabilizes the inverse matrix on the right-hand side of equation 6.12, and $\mathbf{I}$ is a unit matrix. The dagger symbol $\dagger$ indicates Hermitian conjugation. Because equation 6.12 is evaluated for all frequencies, the appropriate value of ϵ will be frequency dependent. When ϵ is too small, the solution of equation 6.12 is unstable and gives rise to artifacts. When ϵ is too large, the solution of equation 6.12 is over-damped and its resolution is low. Therefore, to obtain a high-quality Green's wavefield, it is essential to estimate a suitable value of ϵ at every frequency. Because ϵ may depend on both source-receiver configurations and data acquisition noise, it is difficult to specify an optimal value. Here, we propose a different approach, as discussed below.

To obtain a stable solution for equation 6.9, we adopt a singular-value decomposition (SVD) scheme. SVD is a powerful tool for the solution of ill-posed linear inverse problems (Klema and Laub, 1980). Because the least-squares method using SVD requires the division of singular values, it is easy to evaluate how the retrieved wavefield $\hat{\mathbf{g}}^L$ will be unstably estimated. When the rank of the incident field matrix $\hat{\mathbf{P}}_B^L$ is $r = rank(\hat{\mathbf{P}}_B^L) \leq min(N, M)$, we can use SVD to decompose $\hat{\mathbf{P}}_B^L$ as follows:

$$\hat{\mathbf{P}}_B^L = \mathbf{V}_r \mathbf{\Delta}_r \mathbf{U}_r^{\dagger}, \tag{6.13}$$

where $\mathbf{\Delta}_r$ is an $r \times r$ diagonal matrix whose diagonal components are non-zero singular values. $\mathbf{V}_r$ is an $M \times r$ matrix, the columns of which are composed of the r- eigenvectors of $\hat{\mathbf{P}}_B^L(\hat{\mathbf{P}}_B^L)^\dagger$ having non-zero eigenvalues. $\mathbf{U}_r$ is an $N \times r$ matrix, the columns of which are composed of the r- eigenvectors of $(\hat{\mathbf{P}}_B^L)^\dagger\hat{\mathbf{P}}_B^L$ having non-zero eigenvalues. Now that we have the pseudoinverse of $\hat{\mathbf{P}}_B^L$ as

$$\left(\hat{\mathbf{P}}_B^L\right)^{-1} = \mathbf{U}_r\mathbf{\Delta}_r^{-1}\mathbf{V}_r^\dagger \tag{6.14}$$

and the solution of equation 6.9 becomes

$$\hat{\mathbf{g}}_{est}^L = \hat{\mathbf{p}}_A^L\mathbf{U}_r\mathbf{\Delta}_r^{-1}\mathbf{V}_r^\dagger. \tag{6.15}$$

By evaluating equation 6.15 for all frequencies, we retrieve new spectra of the crosswell Green's function $\hat{G}^L(\mathbf{x}_A, \mathbf{x}, \omega)$ as a common-receiver gather.

An incident field matrix is constructed for each frequency, and the maximum singular values differ for each frequency. The magnitude of the singular value corresponds to the energy of the system and the maximum singular value at each frequency is assumed to be proportional to the magnitude of the energy of the observed data. As previously mentioned, MDD commonly becomes an ill-posed problem when applied to field data, but this is also the case for synthetic data, so the incident field matrix $\hat{\mathbf{P}}_B^L$ will not be a full-rank matrix. Hence, several singular values that are zero or very small compared to the maximum value are typically excluded (e.g., Klema and Laub, 1980; Ursin and Zheng, 1985; Freire and Ulrych, 1988). Also, for MDD it is better to exclude singular values that are small compared to the maximum value for all frequencies.

6.2 Application to modeled data

6.2.1 Model description

We apply the CC method (equation 6.5) and the MDD method (equation 6.15) to modeled data and compare the results. The velocity model we use to model the data is based on the logged P-wave velocity of the field data discussed in the following section. Two vertical boreholes are used, each with 72 receivers installed at intervals of 2 m between 28 m and 170 m depth. These receiver arrays are used to record wavefields from surface energy sources. With interferometry we retrieve crosswell wavefields whose virtual sources are chosen to be in well-2. The distribution of surface sources is important for both the CC and MDD methods. We use the same surface source distribution for the CC and MDD methods to facilitate comparison of the two methods.

As we aim at retrieval of responses at well-1 from virtual sources in well-2 using the MDD method, we place our surface sources only to the right of well-2 (Figure 6.1). Since the velocity model is 1D in the vertical direction, all wavefields recorded in the boreholes from surface sources, lying to the right of well-2, are left propagating. Therefore, we do not need to apply wavefield separation and we can use the total wavefield for MDD. Note that for conventional VSP or crosswell processing, the up-down wavefield separation is performed, while left-right separation is not common. It would be difficult to see prominent left- or right-propagating

waves unless a prominent vertical or steeply dipping reflector is present. Nevertheless, a layered subsurface without strong changes of the seismic parameters in the horizontal direction would effectively give rise to left- or right-propagating fields from a smart choice of surface sources; this would be very beneficial for the application of SI by MDD.

The appropriateness of this one-sided source distribution for the CC method can be explained as follows. Stationary-phase theory for the CC method (e.g. Schuster et al., 2004; Snieder, 2004; Snieder et al., 2006) allows us to consider a hypothetical reflection raypath that propagates from the receiver position in well-2 to the receiver position in well-1. If this hypothetical raypath originates at a surface source, then it can be said that this source lies at the stationary-phase point (is a stationary source) with respect to the retrieval of crosswell reflections. In our velocity model (1D in the vertical direction, Figure 6.1) the stationary sources that produce causal crosswell reflections are all to the right of well-2. Therefore, it is reasonable to install surface sources at the right side of well-2. Surface sources lying to the left of well-1 would produce acausal reflections. Sources lying between the boreholes would contribute to the destructive interference of crosscorrelations (Snieder et al., 2006; Mehta et al., 2008b; Schuster, 2009).

We model 51 surface sources placed at 2 m intervals in a line starting 1 m from well-2 and extending 101 m to the right. Wavefields are modeled using an acoustic finite-difference time domain (FDTD) method (Virieux, 1986). The modeled record length is 0.4 s and the sample interval is 0.2 ms. The source wavelet is a Ricker wavelet with a central frequency of 80 Hz. Gaussian noise is added to the modeled data. The modeled shot gather recorded at well-1 from the surface source 1 m from well-2 (Figure 6.2) shows that there are both direct waves and reflections that originate from subsurface layers.

6.2.2 Characteristic of the rank of the incident field matrix

We construct the matrix and vectors in equation 6.9 for the numerically modeled data by Fourier transformation and apply SVD to the incident field matrix $\hat{\mathbf{P}}_B^L$ for all frequencies (Figure 6.3(a)). For each frequency, $r = rank(\hat{\mathbf{P}}_B^L) \leq min(N, M)$, so Figure 6.3(a) shows 51 singular values, which is the number of sources ($N = 51$). The magnitudes of the singular values shown in Figure 6.3(a) are the diagonal components of $\mathbf{\Delta}_r$ ordered in descending magnitude. The frequency interval for this calculation is 2.5 Hz and the Nyquist frequency is 2500 Hz. However, the singular values are evaluated only up to a frequency of 300 Hz because we consider there would be very little signal above 300 Hz as can be expected for a 80Hz of Ricker wavelet. Therefore, the data at frequencies above 300 Hz are not used for the MDD calculation.

The singular values at 100 Hz (Figure 6.3(b)) show that they decay approximately linearly, but with two different slopes. At the beginning, from first singular value to seventh singular value the slope is steep and these singular values rapidly diminish in amplitude. After about the 44 singular values, the slope is less steep, but the amplitudes are already too low in comparison to the maximum amplitude. This indicates that our problem is ill-posed and the incident field matrix is not a full-rank matrix.

If the wavefield sources were both at the surface and in the subsurface, the available rank

of $\hat{\mathbf{P}}_B^L$ would increase. To confirm this, we model wavefield data from subsurface sources and apply SVD to these data. For this modeling, we use the same receiver configuration as for the surface-source simulation (Figure 6.1) and place 51 sources at 2 m depth intervals from 0 to 100 m in a vertical well 50 m to the right of well-2. The presence of the free-surface would effectively mean a doubling of the source aperture in the direction above the sources due to the interpretation of the free-surface reflections as wavefields from mirrored sources. Because the recording times, though, are still kept the same, 0.4 s, the aperture would not increase so dramatically. We calculate wavefields for this source-receiver configuration and add the same Gaussian noise as that used for the surface-source simulation. Hereafter, we refer to this dataset as the subsurface-source record. We calculate the singular values of the incident field matrix for this subsurface-source record (Figure 6.4(a)). Even though the sources are in the subsurface, the incident field matrix is still not full rank, possibly because of the sparse distribution of sources. However, the subsurface-source record (Figure 6.4(a)) has a higher number of singular values with an amplitude of 5% or more of the global maximum singular value than is the case for the surface-source record (Figure 6.3(a)).

For the subsurface-source record, the singular values at 100 Hz (Figure 6.4(b)) do not reduce linearly, as they do for the surface-source record (Figure 6.3(b)), and the first 11 singular values are larger than those of the surface-source record (Figure 6.3(b)). Therefore, the contributions of these singular values to the pseudoinverse calculation are larger than for the surface-source record because the strength of the correlation of the incident field matrix is decreased by the source distribution.

That $\hat{\mathbf{P}}_B^L$ is not a full-rank matrix can be confirmed from the crosscorrelation matrices $\hat{\mathbf{P}}_B^L(\hat{\mathbf{P}}_B^L)^\dagger$ and $(\hat{\mathbf{P}}_B^L)^\dagger\hat{\mathbf{P}}_B^L$. High values of these crosscorrelations in the off-diagonal elements indicate linear dependence of the rows or columns of the $\hat{\mathbf{P}}_B^L$ matrix, which reduces the rank of $\hat{\mathbf{P}}_B^L$. Because the $\hat{\mathbf{P}}_B^L$ matrix is formed from observed data, the two crosscorrelation matrices $\hat{\mathbf{P}}_B^L(\hat{\mathbf{P}}_B^L)^\dagger$ and $(\hat{\mathbf{P}}_B^L)^\dagger\hat{\mathbf{P}}_B^L$ provide measures of the correlation between receiver gathers and between shot gathers, respectively. Therefore, the strength of the correlation of $\hat{\mathbf{P}}_B^L$ (and the rank of $\hat{\mathbf{P}}_B^L$) may depend on the source or receiver distributions. In other words, the lower rank of the matrix means that the available sources do not illuminate sufficiently the receiver array.

To determine the strength of the correlation of the column components of the incident field matrix (crosscorrelation between shot gathers in well-2 from different sources) we calculate the crosscorrelation matrix $(\hat{\mathbf{P}}_B^L)^\dagger\hat{\mathbf{P}}_B^L$ and scale it to represent the crosscorrelation coefficient as,

$$\mathbf{R}(i,j) = \frac{\mathbf{V}(i,j)}{\sqrt{\mathbf{V}(i,i)\mathbf{V}(j,j)}}, \tag{6.16}$$

where $\mathbf{V}$ is a variance-covariance matrix of shot gathers (variance and covariance of the column components of $\hat{\mathbf{P}}_B^L$) and $\mathbf{R}$ represents the coherence matrix, which is a crosscorrelation coefficient matrix scaled by the standard deviations of each shot gather. The ith-row and jth-column components of Figure 6.5(a) indicate the absolute values of the coherence ($\mathbf{R}(i,j)$) for shot gathers in well-2 whose (surface or subsurface) sources are at $\mathbf{x}_S^{(i)}$ and $\mathbf{x}_S^{(j)}$. Therefore, the diagonal components of the crosscorrelations (Figure 6.5(a)) are all equal to 1. If there are many components with large coherence in the off-diagonal elements, the observed data resemble each other and

the available rank of the incident field matrix is low. The coherence of the incident field matrix for the surface-source record (Figure 6.5(a)) show a strong correlation along the vicinity of the diagonal components (warm colored area). This indicates that the shot gathers from adjacent surface sources correlate well, possibly because of the simple velocity model we used. We also show the coherence matrix of the incident field matrix for the subsurface-source record (Figure 6.5(b)). Here, the gridded structure appearing in Figure 6.5(b) comes from the interference of events reflected with positive and negative reflection coefficients. The strongest contributor to this structure is the free-surface, whose reflection coefficient is -1. In Figure 6.5(a) this gridding is not visible because the sources are located at the free-surface in this situation. The coherence matrix of the incident field matrix for the subsurface-source record (Figure 6.5(b)) show a narrower diagonal correlated area than that of the surface-source record (Figure 6.5(a)). This indicates that the shot gathers from vertically adjacent sources are less well correlated. There are 401 components of the surface-source record with coherence that exceed 0.9, whereas only 119 components of the subsurface-source record are in that category (Figure 6.5(a) and 6.5(b), respectively).

The above observations confirm that subsurface sources provide a higher-ranked incident field matrix than surface sources, and thus provide a larger amount of data that contributes to retrieved crosswell wavefields. The simple horizontally layered velocity structure we use in this study contributes to the strong correlation of the surface-source record. The strength of the correlation of observed data would be dependent on the velocity model. Therefore, for a more complex velocity model, the rank of the incident field matrix would increase because the strength of the correlations between data is reduced by the complex raypaths that result from surface sources. The multiple scattering from the subsurface complexities would increase the receivers' illumination from different directions and effectively would add extra secondary sources in the subsurface. However, for a more complex velocity model, separation of the left-going wavefield, which is a condition for MDD, might be required. Furthermore, complexity might introduce common stationary noise, e.g., scattering from a point-like scatterer (in relation to the dominant wavelength) would introduce energy that illuminates the receivers from the same direction irrespective of the position of the surface sources. Such case, though, would not be frequent.

6.2.3 Imaging results from crosscorrelation and multidimensional deconvolution

We retrieve crosswell reflection wavefields from surface source records using the CC and MDD methods. We use as surface source records the acoustically modeled data inside two boreholes, each with 72 receivers installed at intervals of 2 m between 28 m and 170m depth. We model 51 surface sources placed at 2 m intervals in a line starting 1 m from well-2 and extending 101 m to the right. For our retrieval using the MDD algorithm, the rank of the incident field matrix $\hat{\mathbf{P}}_B^L$ is determined taking into account only those values that are larger than 5% of the maximum value (Figure 6.3(a)). We estimate the crosswell Green's function $\hat{G}^L(\mathbf{x}_A, \mathbf{x}, \omega)$ as a receiver gather from equation 6.15. Figure 6.6(a) shows the crosswell common-receiver gather retrieved by MDD in the time domain for the receiver at 106 m depth in well-1. For

comparison, we also retrieve the crosswell common-receiver gather by using the CC method (Figure 6.6(b)) with equation 6.5. The receiver gather retrieved by the CC method (Figure 6.6(b)) is wavelet-deconvolved after crosscorrelation and summation (equation 6.5). We also directly model a wavefield for a receiver placed at 106 m depth in well-1 and sources placed at 2 m depth intervals from 28 m to 170 m in well-2 (Figure 6.6(c)). The responses in Figure 6.6(c) are also wavelet-deconvolved. Each of the three receiver gathers shows a free-surface reflection (r1, down-going reflection), a reflection from the boundary at 160 m depth (r2, up-going reflection), and a reflection from the boundary at 40 m depth (r3, down-going reflection). Here, by up-going (or down-going) reflections we mean reflected waves that propagate upward (or downward) from the acoustic impedance boundary that causes their reflection. The direct arrivals below around 100m were not retrieved in either the MDD (Figure 6.6(a)) or CC (Figure 6.6(b)) results. This is because there are no up-going waves contributing to the retrieval of those direct arrivals.

The CC result is dominated by up-going waves, whereas the MDD result contains both (up and down) events with better relative amplitudes. For example, the down-going waves (r1 and r3) are appearing in the MDD results with better amplitudes than in the CC results. Since the CC result is dominated by up-going waves, r3 is covered by down-going events and can not be recognized in Figure 6.6(b). The up-going events (r2) are retrieved well in both the MDD and CC results. The MDD result (Figure 6.6(a)) and CC result (Figure 6.6(b)) exhibit comparable resolution because MDD directly retrieves Green's functions, whereas the CC result is deconvolved by a wavelet that is the autocorrelation of the original wavelet of the surface sources.

The fact that we use sources only at the surface means that we create a preferred direction of illumination at the receiver arrays from above, that is, for up-going reflections. For the retrieval of down-going reflections, we rely on contributions from waves that have reflected at subsurface layers, and thus act as secondary Huygens sources, before being recorded by the receivers in well-2. Such waves are at least second-order reflections of relatively low energy. Furthermore, equation 6.1 is obtained after a far-field approximation. For secondary sources close to the receivers this approximation is not valid anymore and might result in significant amplitude errors. The above reasons could explain why the CC result in Figure 6.6(b) exhibits mainly up-going retrieved events. On the other hand, the MDD method would treat the amplitudes of both up- (r2) and down-going reflections (r1 and r3) more accurately and would give better results (Figure 6.6(a)). This happens because the MDD method is more robust with respect to the source distribution than the CC method as shown in Wapenaar et al. (2008b).

We image the subsurface structure using retrieved crosswell wavefields. We retrieve all the crosswell wavefields (i.e., all crosswell receiver gathers). Because there are 72 receivers in well-1, we apply MDD (equation 6.15) 72 times. The total crosswell wavefields retrieved from MDD contain 72×72 traces. For imaging, retrieved crosswell data are decomposed into up- and down-going reflections. Up-going reflections are used for imaging of the deep structures and down-going reflections are used for imaging of the shallow structures (Lazaratos et al., 1993). We decompose the crosswell wavefield using an $f - k$ filter and apply Kirchhoff prestack depth migration (Figure 6.7). In the direct modeling result (Figure 6.7(c)), the images from 0 m to 90 m are produced from down-going reflections while the images below 90 m are produced from up-

going reflections. In the SI results (Figures 6.7(a) and 6.7(b)), we change this cut-off depth to 55 m because it produced better signal-to-noise ratio (S/N). This possibly comes from the fact that in the SI the effective propagation direction is dominated by up-going waves. The amplitudes of these images are normalized with the amplitude at 40 m depth for the shallow structure (from down-going reflections) and with the amplitude at 160 m depth for the deep structures (from up-going reflections). The MDD and CC results (Figures 6.7(a) and 6.7(b)) agree well with the direct modeling result (Figure 6.7(c)) and the velocity model (Figure 6.7(d)). However, the images from 0 m to 55 m (from down-going reflections) are relatively noisy. We show the migrated signals halfway between the two boreholes in Figure 6.8. The MDD and CC results (Figures 6.8(a) and 6.8(b)) are noisier than the direct modeling result (Figure 6.8(c)). However, the peak amplitudes below 55 m compare well with the direct modeling result (Figure 6.8(c)) and the reflection coefficients (Figure 6.8(d)). The amplitudes from 0 m to 55 m show the correct amplitude peaks around 20 m and 40 m depth, however, the phases between 20 m and 40 m are not correctly imaged. This is possibly caused by the insufficient retrieval of down-going reflections and the smearing effects of migration. Comparing the two SI results with the direct modeling result, we can also see that for the shallow reflectors the MDD result in Figure 6.8(a) is better resolved than the CC result in Figure 6.8(b) and resembles more the direct modeling result in Figure 6.8(c). This could be because the MDD method treats the amplitude of down-going wave better than the CC method. For the deeper layers, both the MDD and CC methods resolved subsurface layers very well.

6.3 Application to field data

6.3.1 Field data acquisition

We compare the results of seismic interferometry applied to field data by the CC (equation 6.5) and the MDD (equation 6.15) methods. The field data are recorded in Aomori Prefecture, north-east Japan. The upper 200 m of the survey area is composed mainly of horizontal alternating layers of sandstone and tuff. The distance between the two boreholes and the receiver configuration are identical to those of the numerical modeling (Figure 6.1). We use two boreholes, each with 72 borehole hydrophones installed between 28 m and 170 m depth with an interval of 2 m. The horizontal distance between the boreholes is 50 m. Also, we install explosive surface sources to the right of well-2. Because the area available for this experiment is limited, only 13 sources are placed (at 5 m intervals) on the right side of well-2. A 24-channel hydrophone (2 m interval) cable is used 3 times in the borehole to provide coverage from 28 m to 170 m depth. The temporal recording length is 0.4 s at a sampling rate of 0.25 ms, as is the case for the modeled data. To verify the crosswell wavefields retrieved from surface-source records, we also acquire crosswell wavefields using a downhole non-explosive OYO Wappa source (OWS; OYO Corporation, Tsukuba, Japan) (Takahashi et al., 2001; Ogura et al., 1992) and 3-component geophones. OWS is a borehole source that generates compressional waves in a fluid with a bandwidth of up to several thousand Hertz. We install 72 subsurface sources from 28 m to 170 m depth at 2 m intervals. Note that for the field experiment (a 3D configuration), the source

boundary for CC ($\partial\mathbb{D}$ in equation 6.4) and the receiver boundary for MDD ($\partial\mathbb{D}_2$ in equation 6.7) should be a 2D surface. However, we still approximate them as 1D lines, as was the case for the numerical modeling, assuming that there are no significant velocity changes along the crossline direction for the boreholes.

To isolate the P-waves in the surface-source record, we remove S-waves and tube-waves by using an $f-k$ filter. The so-obtained P-waves are normalized to rms amplitudes (Figure 6.9). Both reflected waves and direct waves can be seen in Figure 6.9. Horizontal geological layers are predominant in this area, so we regarded the observed wavefields as leftward propagating and did not need to isolate them from right-propagating wavefields before MDD.

6.3.2 Results

We evaluate singular values of the incident field matrix $\hat{\mathbf{P}}_B^L$ at all frequencies (Figure 6.10(a)). The frequency interval for this calculation is 2.5 Hz and the Nyquist frequency is 2000 Hz. We consider that signals are within the range from 0 to 400 Hz, and calculate the singular values up to 400 Hz. At 100 Hz, singular values beyond the 8th-largest value are much smaller than the maximum singular value (Figure 6.10(b)). Small singular values indicate that the incident field matrix is not full rank as was the case for the numerical modeling, so these small singular values must be truncated. We use singular values which exceed 5% of the maximum singular value (Figure 6.10(a)).

We apply the MDD method to retrieve the crosswell wavefield as a receiver gather (Figure 6.11(a)). We also retrieve the equivalent receiver gather using the CC method (Figure 6.11(b)). The result by the CC method (Figure 6.11(b)) is wavelet-deconvolved after crosscorrelation and summation (equation 6.5). The direct arrivals below approximately 100m were not retrieved in either the MDD (Figure 6.11(a)) or CC (Figure 6.11(b)) results because of the location of the sources. Comparison of these wavefields reveals that the resolution of the MDD method and the CC method is almost the same. However, the MDD result for the field data contains both down-going and up-going events, as was also demonstrated with the modeled data. In contrast, the CC result is dominated by up-going events. For comparison, the receiver-gather data for the downhole source is also shown (Figure 6.11(c)). Here, the horizontal displacements of the 3-component geophone records are shown. Because the interferometric results (Figures 6.11(a) and 6.11(b)) are shown as acoustic hydrophone wavefield, they differ both in phase and amplitude from the wavefields recorded by the geophone. For our comparison, therefore, we focus on the traveltimes of the retrieved reflections. We can see that the traveltimes of several reflections in the wavefields retrieved by interferometry are the same as those recorded from downhole sources (Figure 6.11(c)).

We apply prestack depth migration to the total crosswell wavefields (72×72 traces) derived by MDD (Figure 6.12(a)), by CC (Figure 6.12(b)), and from a downhole source (Figure 6.12(c)). The images from 0 m to 90 m depth are produced from down-going reflections and the images below 90 m depth are produced from up-going reflections. The amplitudes are normalized by that of 25 m depth for shallow structures (from down-going reflections) and by that of 180 m

depth for deep structures (from up-going reflections). The dominant frequency of the wavefields generated by the OWS downhole source is much higher than that for the borehole records from surface sources (Figure 6.13). Further, the resolution of the reflection boundaries using the downhole sources (Figure 6.12(c)) is higher than the resolution obtained from interferometry. This can be explained by the very different bandwidths of the OWS and surface sources. The resolution of the wavefield retrieved from interferometry could be improved by using large-bandwidth surface sources. Nevertheless, the reflection boundaries, for example at 25 m, 100 m and 180 m depth (arrows in Figure 6.12) are imaged in both the MDD and the CC result. Furthermore, these images agree well with the P-wave velocity log from well-2 (Figure 6.12(d)).

6.4 Discussion

We show that application of SI by MDD and by CC to crosswell data from impulsive sources at the surface can retrieve the reflection response between the two boreholes as if there were sources in one of the boreholes. Comparing the retrieved results in Figures 6.6(a), 6.6(b) and Figures 6.11(a), 6.11(b) to results from an actual source in borehole well-2 (Figures 6.6(c) and 6.11(c), respectively), we can interpret several retrieved reflections. On the other hand, in the Figures 6(a,b) and 11(a,b) we can also see different arrivals that are not present in Figures 6.6(c) and 6.11(c). For example, in Figures 6(a,b) there are arrivals close in time to r2 that are parallel to this reflection or which even cross it. Such arrivals are not present in Figure 6.6(c). These are non-physical (ghost) arrivals that appear in the retrieved results due to insufficient illumination by the active sources.

We show that the MDD and CC methods, applied to surface-source records, retrieve up-going reflection wavefields very well. Furthermore, the MDD method retrieves down-going reflections with more accurate amplitudes than the CC method. However, the MDD problem for surface-source records is ill-posed, so the rank of the incident field matrix must be determined with care in this case. Because the CC method does not need a rank determination, it is simpler to achieve stable results than with the MDD method.

In order to compare the computational costs of the CC method and the MDD method, we measure the computation time to retrieve 72 crosswell receiver gathers using the dataset of the numerical-modeling section. The computation time for the CC method is 30 s whereas that for the MDD method is 68 s using Intel Core i7 (2.93GHz) with 12GB memory. The MDD method takes longer time than the CC method because the MDD method requires SVD and a construction of the pseudoinverse matrices.

We assume a horizontally layered structure to avoid left-right decomposition for the MDD method. If the subsurface structure is more complex, the rank of the incident field matrix may be improved because the degree of correlation of the data is reduced by the complex reflection raypaths generated by surface sources. For this case, however, complexity might introduce stationary noise and, most importantly, also it would be necessary to separate the wavefields before the application of MDD into left- and right-propagating wavefields.

In our field experiment, the bandwidth and resolution of the crosswell wavefield observed

when using a downhole source are superior to those of the wavefields retrieved by interferometry. This is because the bandwidth of the actual wavefield is much larger than that of the surface-source record (Figure 6.13). Note further that the radiation pattern of the retrieved downhole virtual sources is limited by the surface-source aperture and cannot match the radiation pattern of the actual downhole sources, which emits in all directions. The results from the CC method are more sensitive to the surface-source wavelet because the dependence on the wavelet needs to be eliminated with wavelet deconvolution after the crosscorrelation. In this way, differences in the wavelets from the different surface sources and from different receiver responses might not be optimally accounted for. Contrary to this, the MDD method accounts implicitly for differences in the source wavelets during the retrieval process and this might in other applications result in a better retrieval of the higher frequencies within the band of the energy emitted by the surface sources. On the other hand, for the MDD method, we do not use the high-frequency components of the seismic signal because their amplitudes are too low and get lost within the noise. Therefore, the bandwidth for our MDD results is narrow and lacks high-frequency components. One of the reasons the wavefields recorded with the OWS downhole sources in our field survey have a larger bandwidth than the surface-source records is that the OWS sources have a larger bandwidth than the surface sources. In another application, Mehta et al. (2008a, 2010) show that the conventional crosswell data contains much higher frequencies than the virtual crosswell data because the source-type of the virtual crosswell data is a vibroseis whereas for conventional crosswell data the source is a downhole high-frequency exciter. Another important reason for the relatively narrow bandwidth is that the high-frequency components of the crosswell wavefields generated by downhole sources are likely to be attenuated less than those generated by the surface sources because the former have shorter raypaths. For the source-receiver configuration we use, the raypaths for surface-source records will always be longer than the crosswell raypaths. Therefore, even if both the surface and the downhole sources were to have identical bandwidth, the bandwidth of a crosswell wavefield retrieved by interferometry would be lower than that of a wavefield generated by a downhole source because of additional attenuation along the longer raypaths. The bandwidth of the retrieved wavefield can possibly be improved by using surface sources with larger bandwidth. However, the fact that the crosswell SI contains lower frequencies than the conventional crosswell method suggests that the combination of these two methods would give us a larger bandwidth than that from each method alone.

The source-receiver configuration of our crosswell SI is identical to the conventional VSP survey but with two boreholes. The advantage of crosswell SI over VSP imaging is that crosswell SI does not require the velocity of the weathered near-surface layers to image deep structures. This has the potential to image the detailed structures below a complex overburden or obstacles. Furthermore, by using crosswell SI, down-going reflections can be easily utilized for imaging because the down-going multiple reflections in VSP data are transformed into down-going primary reflections in the retrieved crosswell data.

6.5 Conclusions

We compare the application of the multidimensional deconvolution (MDD) and crosscorrelation (CC) seismic interferometry methods to numerically modeled and field data to retrieve crosswell seismic reflection wavefields. Our results demonstrate the feasibility of obtaining crosswell seismic reflection data by using widely separated boreholes without using downhole energy sources. Because MDD solutions require stabilization, we use a singular value decomposition (SVD) pseudoinverse solution to achieve MDD.

Our numerical modeling shows that because the data recorded from surface sources are correlated, the incident field matrix is not of full rank and the MDD problem is therefore ill-posed. Furthermore, the numerical modeling shows that the use of subsurface sources improves the rank of the incident field matrix, which indicates that a wider source distribution could be used to increase the amount of data that contributes to the retrieval of crosswell wavefields.

We apply the CC and the MDD methods to field data to retrieve the crosswell wavefields and then migrate the retrieved reflections. The retrieved images agree well with migrated data from a conventional crosswell seismic reflection survey and with P-wave velocities from well logs. The comparison of the retrieved reflected wavefields from the two methods with the reflected wavefields observed using borehole vibrators shows that both the MDD and CC methods retrieve up-going reflections very well, and the MDD method retrieves down-going reflections with better amplitude preservation than the CC method.

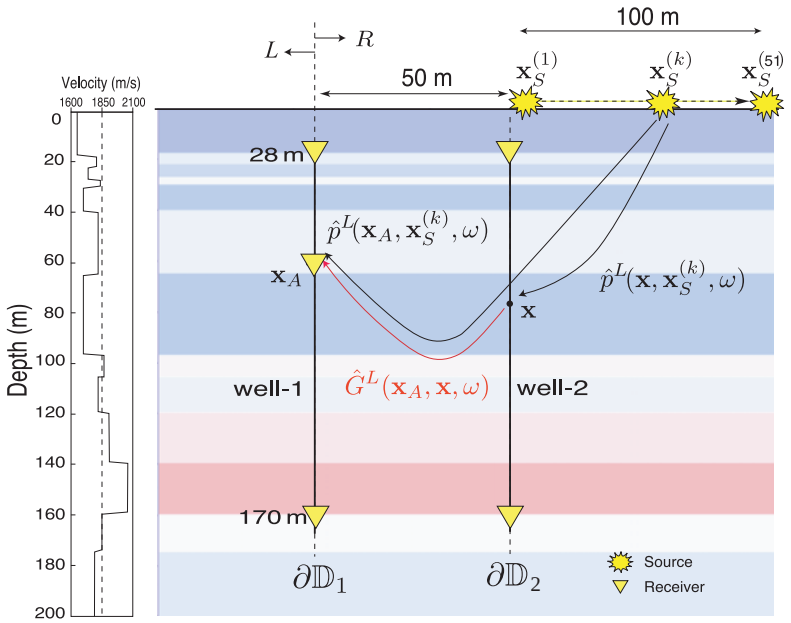

Figure. 6.1: Velocity model and source-receiver configuration used for numerical modeling. There are 72 receivers at 2 m interval in each borehole and 51 sources ($\mathbf{x}_S^{(1)}$ to $\mathbf{x}_S^{(51)}$) at the surface. $\mathbf{x}_S^{(k)}$, $\mathbf{x}$, and $\mathbf{x}_A$ represent the source and the two observation locations as used in equations 6.5 and 6.7, while $\partial\mathbb{D}_1$ and $\partial\mathbb{D}_2$ indicate the chosen position of the boundaries from equation 6.6. $\hat{p}^L(\mathbf{x}_A, \mathbf{x}_S^{(k)}, \omega)$ is the acoustic wavefield observed at receiver position $\mathbf{x}_A$ in well-1 from a physical source at the surface at $\mathbf{x}_S^{(k)}$. $\hat{p}^L(\mathbf{x}, \mathbf{x}_S^{(k)}, \omega)$ is the acoustic wavefield observed at receiver position $\mathbf{x}$ in well-2 from the same physical source at $\mathbf{x}_S^{(k)}$. $\hat{G}^L(\mathbf{x}_A, \mathbf{x}, \omega)$ represents the crosswell Green's function at receiver position $\mathbf{x}_A$ in well-1, assuming that receiver $\mathbf{x}$ in well-2 is the virtual source position.

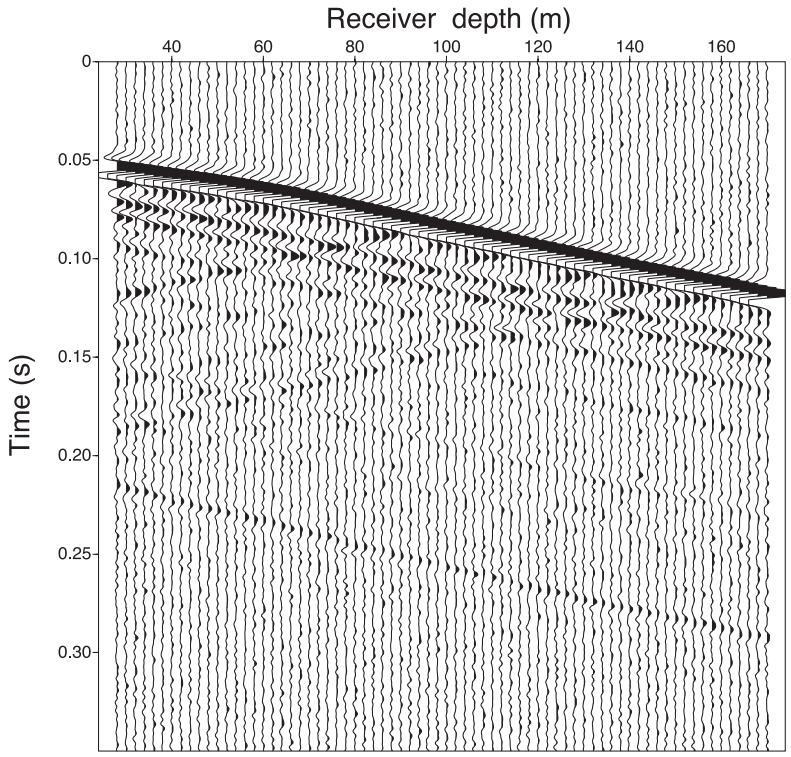

Figure. 6.2: Example of data modeled using a finite-difference time domain method. The data for this shot gather are recorded in well-1 from the first surface source to the right of well-2. Gaussian noise is added to the modeled data after normalization to rms amplitude. The signal-to-noise ratio is set to 40.

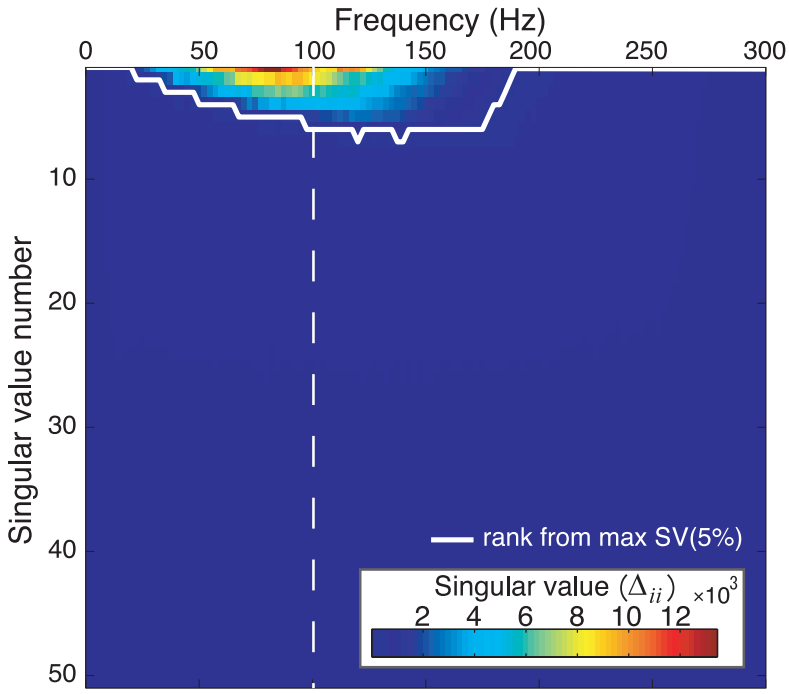

(a)

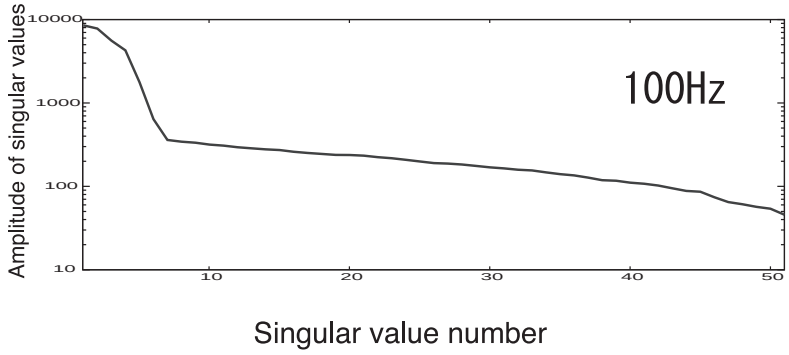

(b)

Figure. 6.3: Singular values Δ_{ii} of the incident field matrix $\hat{\mathbf{P}}_B^L$ from surface-source data. (a) Singular values of $\hat{\mathbf{P}}_B^L$ at each frequency. The solid white line shows the rank determined from the 5% criteria of the global maximum. (b) Singular values of $\hat{\mathbf{P}}_B^L$ at 100 Hz as indicated by the dashed line in (a).

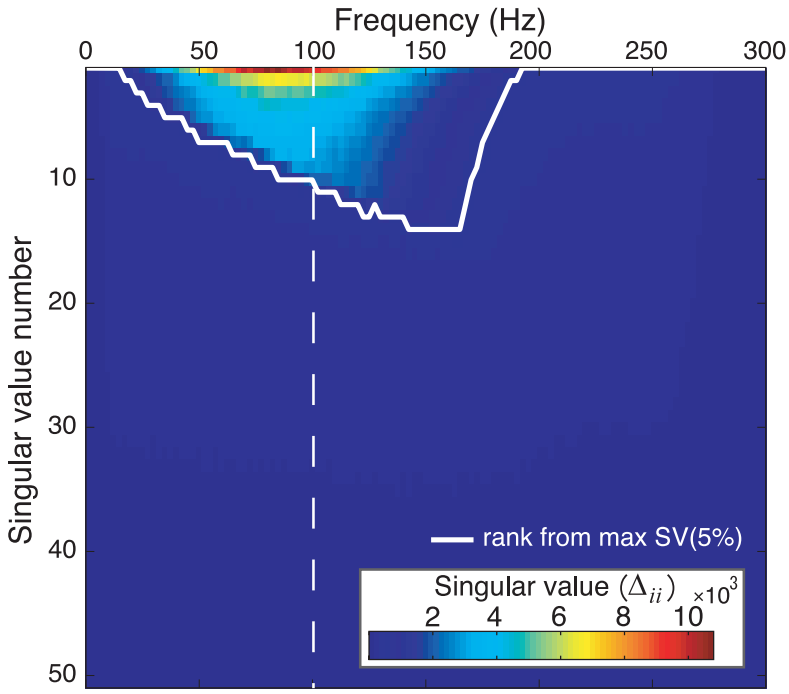

(a)

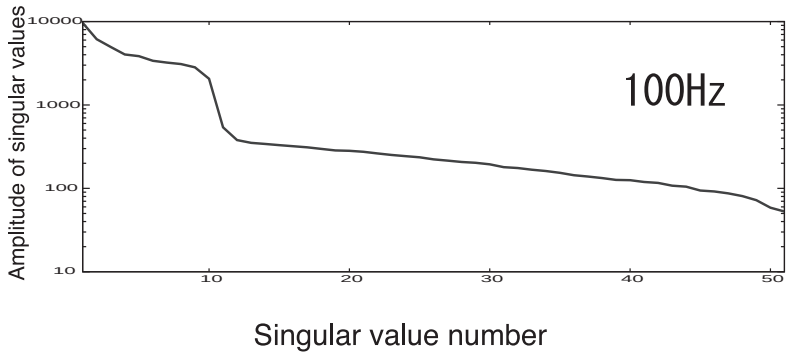

(b)

Figure. 6.4: Singular values Δ_{ii} of the incident field matrix $\hat{\mathbf{P}}_B^L$ from subsurface-source data. (a) Singular values of $\hat{\mathbf{P}}_B^L$ at each frequency. The white solid line shows the rank determined from the 5% criteria of the global maximum. (b) Singular values of $\hat{\mathbf{P}}_B^L$ at 100 Hz as indicated by the dashed line in (a).

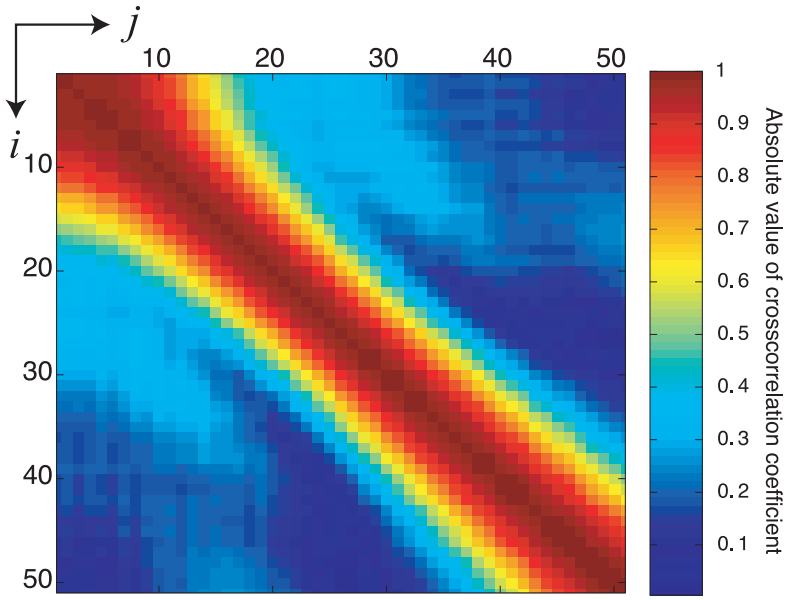

(a)

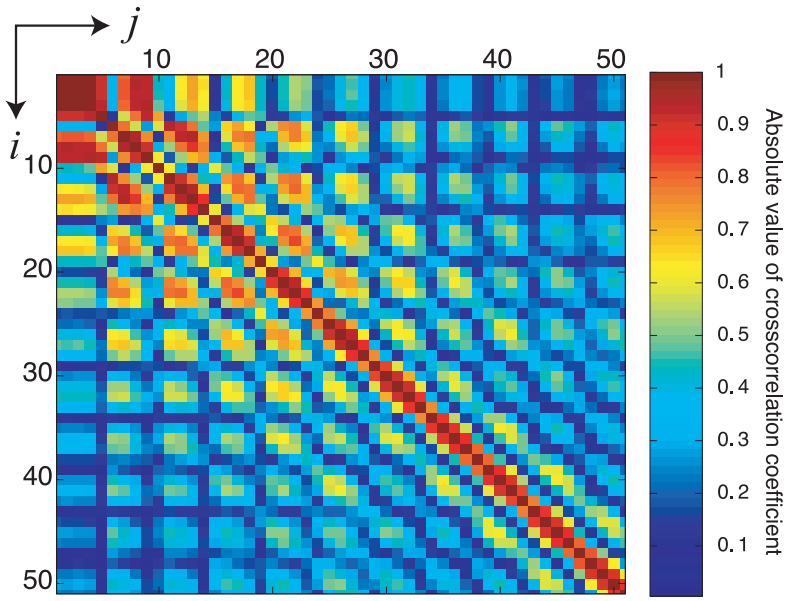

(b)

Figure. 6.5: Absolute value of the coherence matrix of the incident field matrix. Scaled $(\hat{\mathbf{P}}_B^L)^\dagger \hat{\mathbf{P}}_B^L$ for 100 Hz from (a) surface-source data and (b) subsurface-source data. The indices i and j indicate the coherence of the observed shot gather from the sources at positions $\mathbf{x}_S^{(i)}$ and $\mathbf{x}_S^{(j)}$ for 100 Hz.

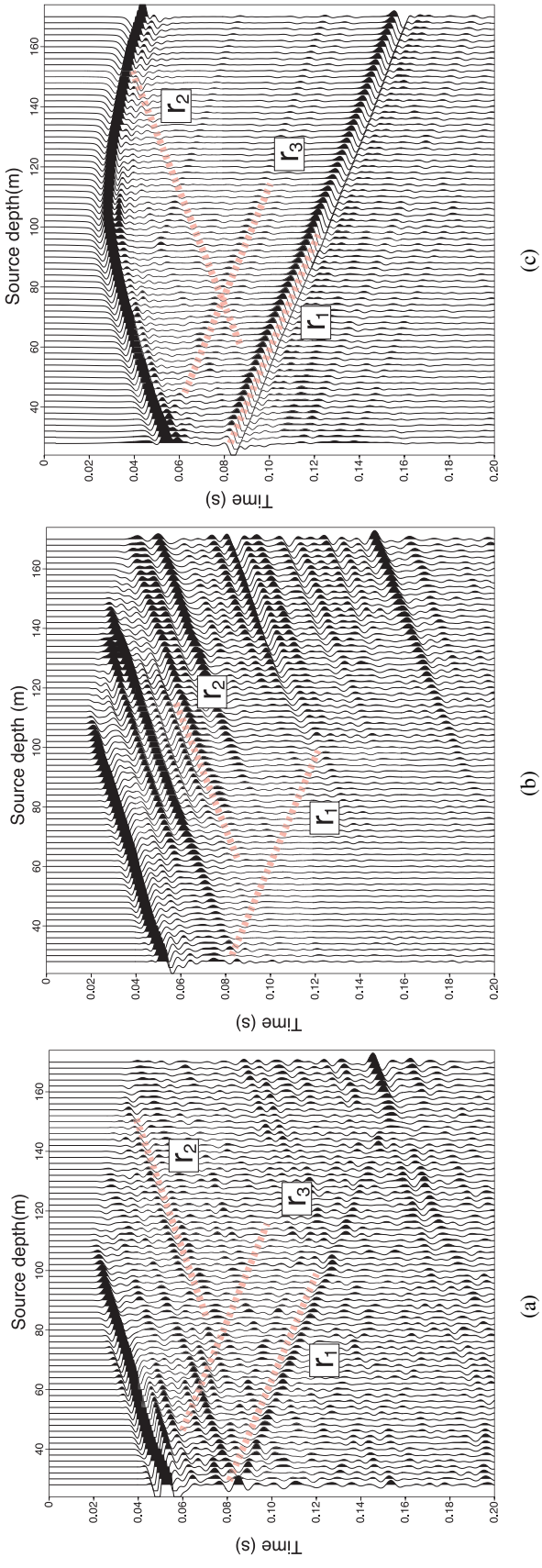

Figure. 6.6: Synthetic Crosswell receiver gather retrieved from surface sources and constructed in the time domain for a receiver at 106 m depth in well-1 from (a) multidimensional deconvolution, (b) Wavelet-deconvolved crosscorrelation, (c) wavelet-deconvolved direct modeling of the same receiver gather with downhole sources at 2 m depth intervals from 28 m to 170 m in well-2. The pink dotted lines indicate a free-surface reflection (r1, down-going wave), a reflection from the boundary at 160 m depth (r2, up-going wave), and a reflection from the boundary at 40 m depth (r3, down-going wave). Events at times earlier than the direct arrival have been muted in panels (a) and (b).

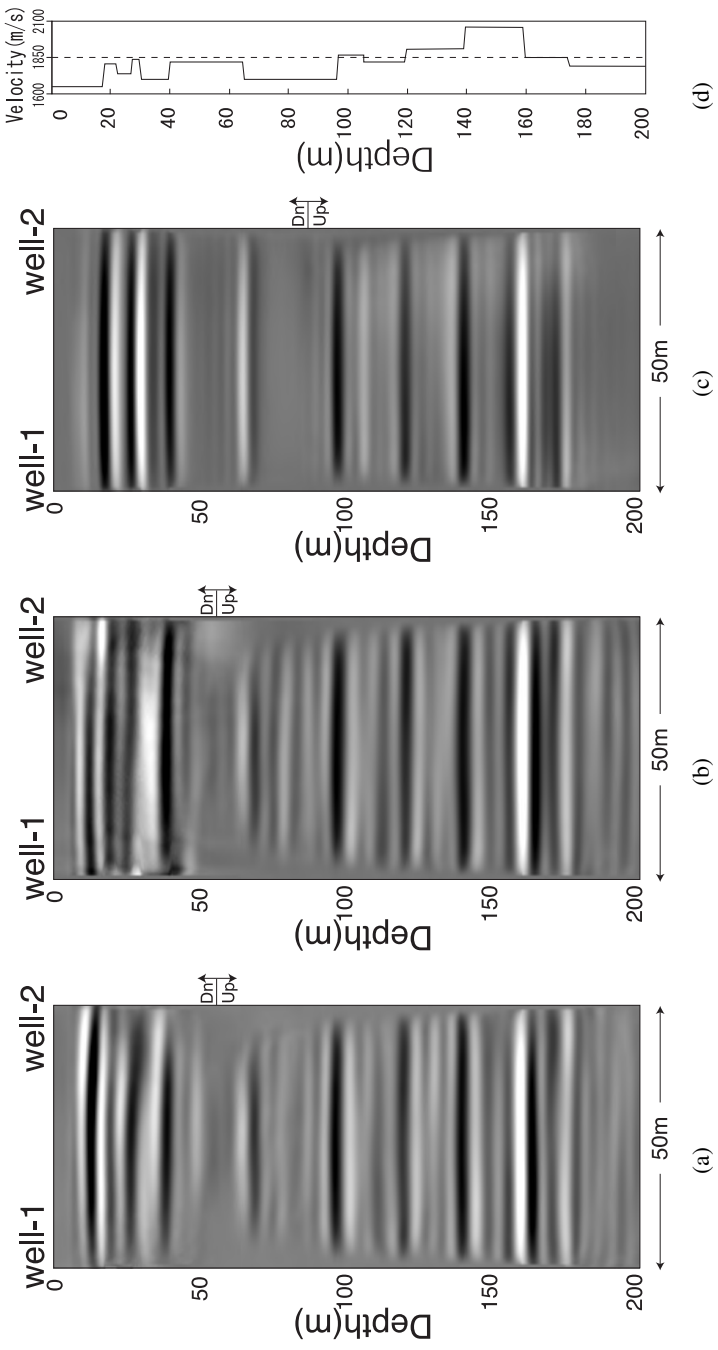

Figure. 6.7: Results of Kirchhoff prestack migration obtained from (a) multidimensional deconvolution, (b) wavelet-deconvolved crosscorrelation and (c) wavelet-deconvolved direct modeling. (d) The velocity model used for migration.

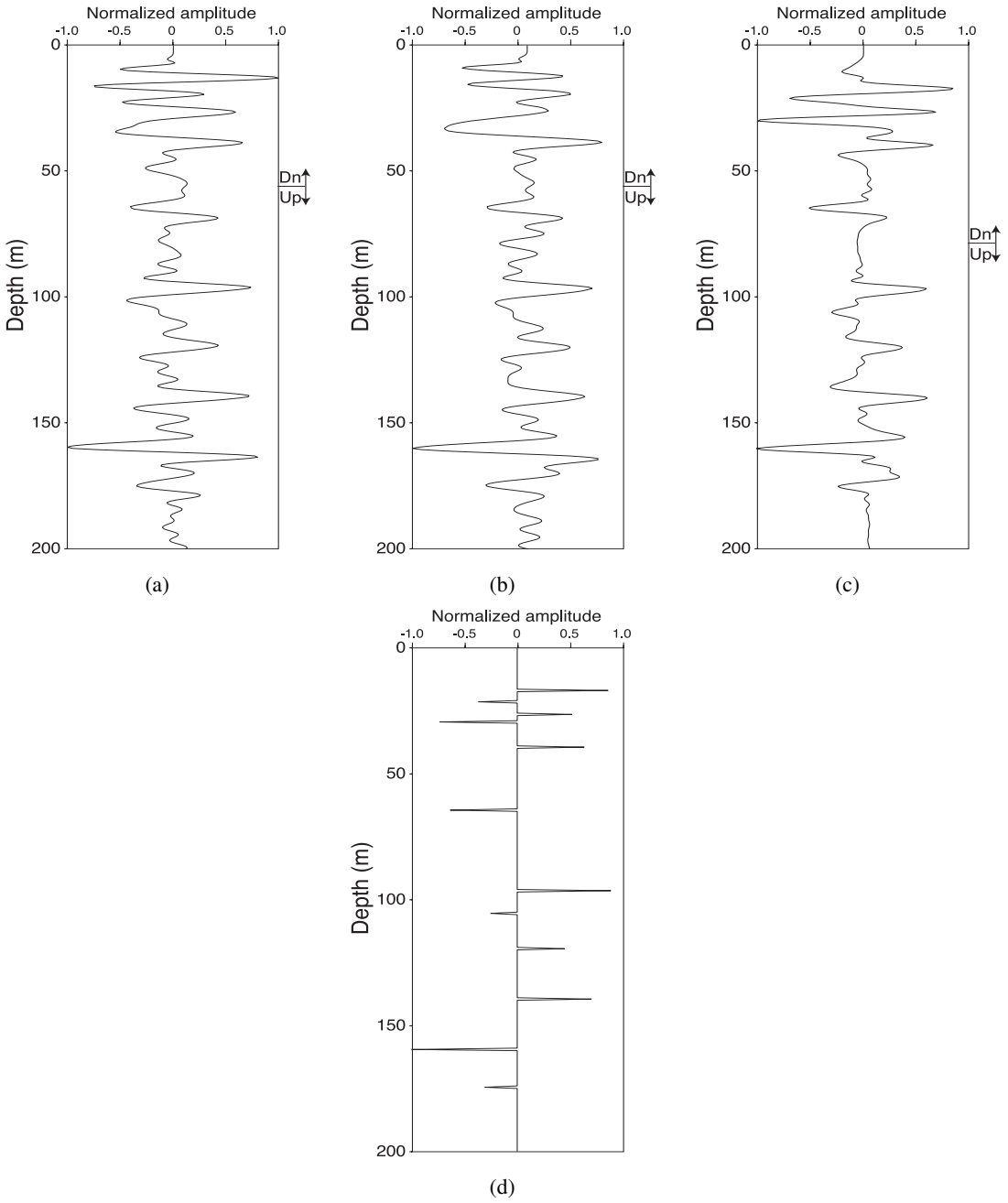

Figure. 6.8: Migrated signals (after amplitude normalization) for the trace at the middle of the boreholes in Figure 6.7 from (a) multidimensional deconvolution, (b) wavelet-deconvolved crosscorrelation and (c) wavelet-deconvolved direct modeling. (d) The refection coefficients calculated from Figure 6.7(d).

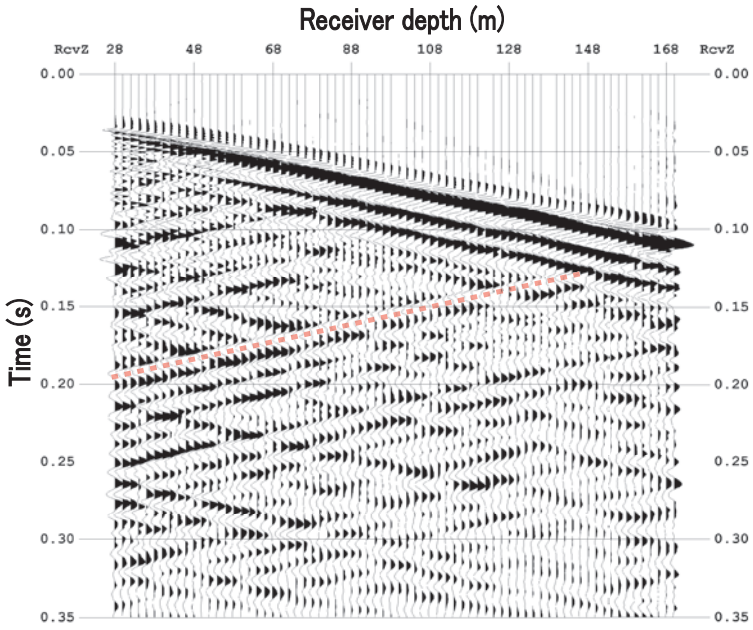

Figure. 6.9: Example of the recorded field data after preprocessing: a shot record in well-1 from the surface source at 5m distance from well-2. The pink dotted line indicates a reflection signal from a subsurface boundary.

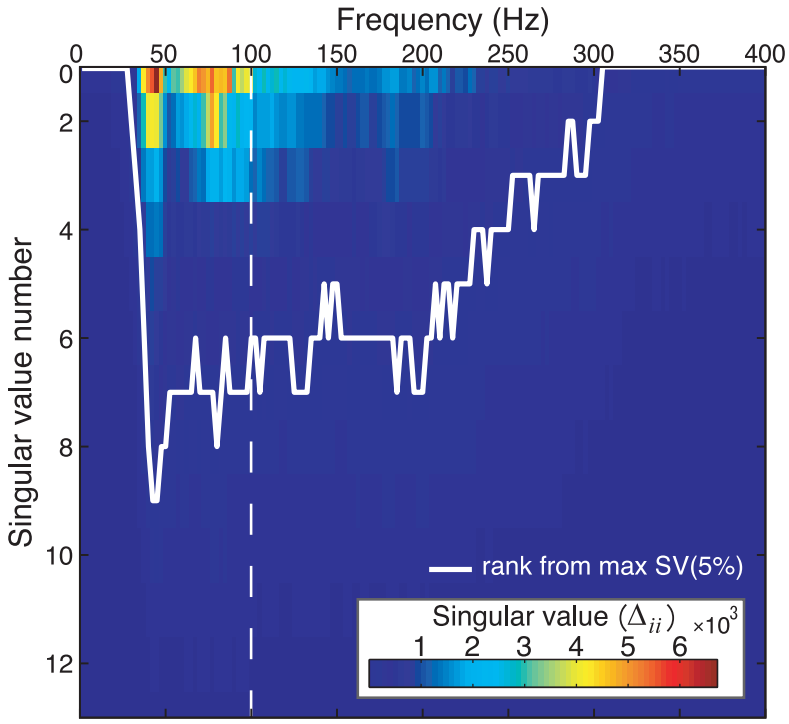

(a)

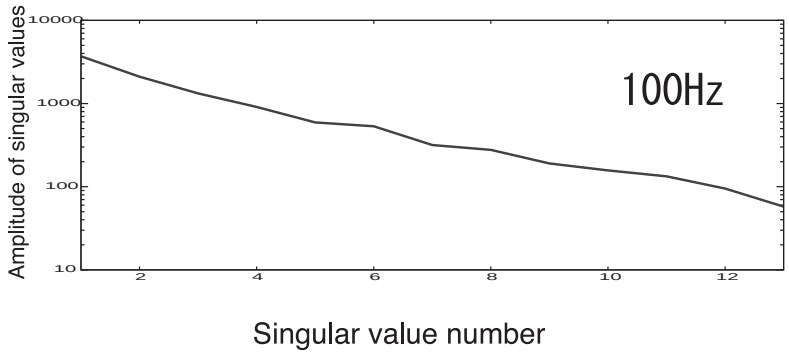

(b)

Figure. 6.10: Singular values of the incident field matrix $\hat{\mathbf{P}}_B^L$ for the field data. Because $r = rank(\hat{\mathbf{P}}_B^L) \leq min(N, M)$, where N and M are the number of sources and receivers, there are 13 singular values for each frequency. (a) Singular values of $\hat{\mathbf{P}}_B^L$ at each frequency. The solid white line shows the rank determined from the 5% criteria. (b) Singular values of $\hat{\mathbf{P}}_B^L$ at 100 Hz as indicated by the dashed line in (a).

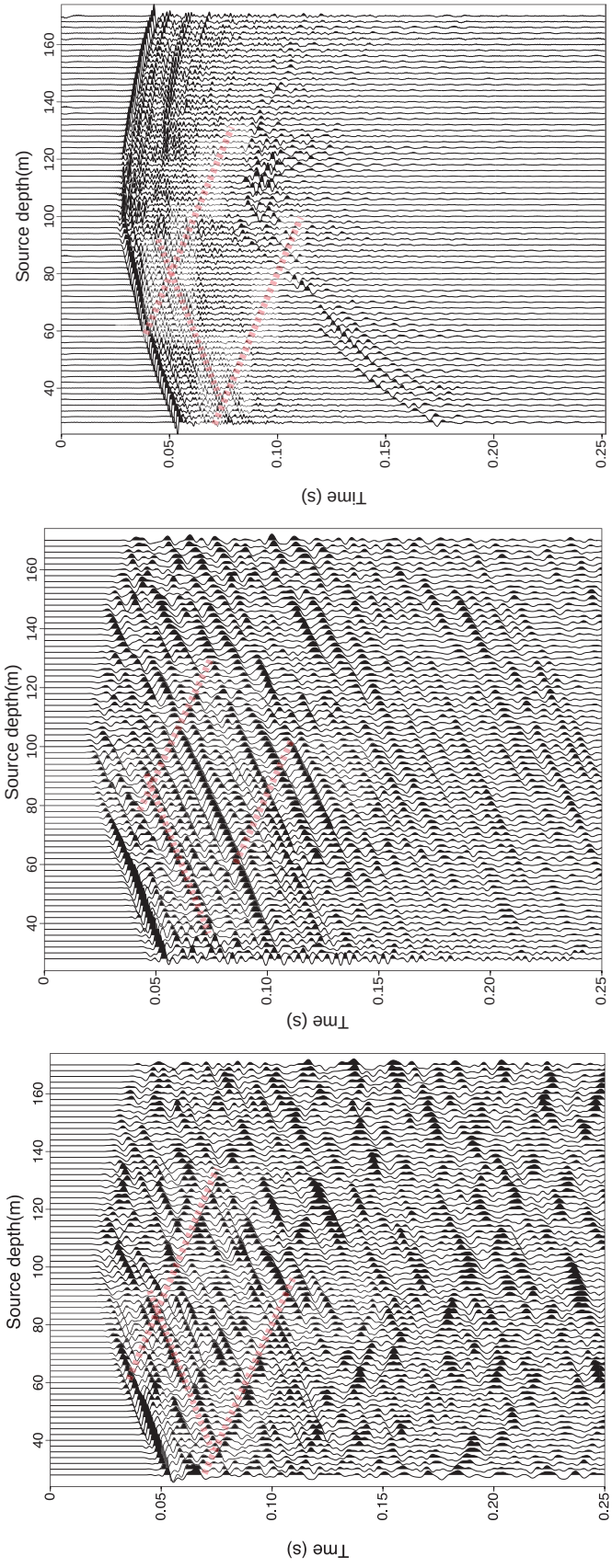

Figure. 6.11: Crosswell receiver gather (P-waves) shown in the time domain as retrieved from surface sources for the receiver at 106 m depth in well-1 from (a) multidimensional deconvolution (MDD) and (b) wavelet-deconvolved crosscorrelation (CC). (c) The wavelet-deconvolved same receiver gather from a downhole source in which we observe S-waves. The pink dotted lines indicate reflection events retrieved by MDD and CC that correspond to the downhole source. Events at times earlier than the direct arrival have been muted in panels (a) and (b).

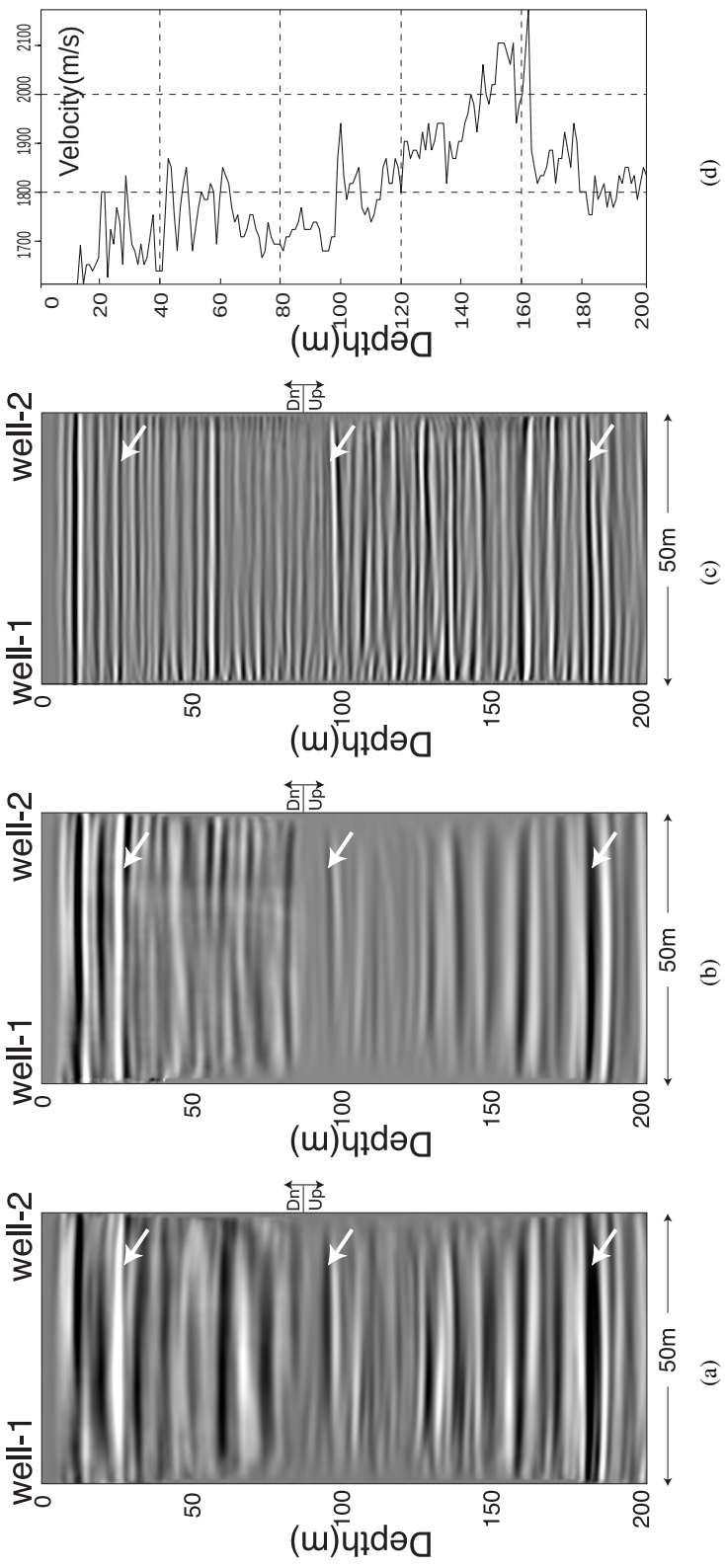

Figure. 6.12: Results of Kirchhoff prestack migration obtained from (a) multidimensional deconvolution and (b) wavelet-deconvolved crosscorrelation. (c) Migrated output from downhole sources and (d) P-wave velocity logged at well-2. Arrows show example reflection boundaries.

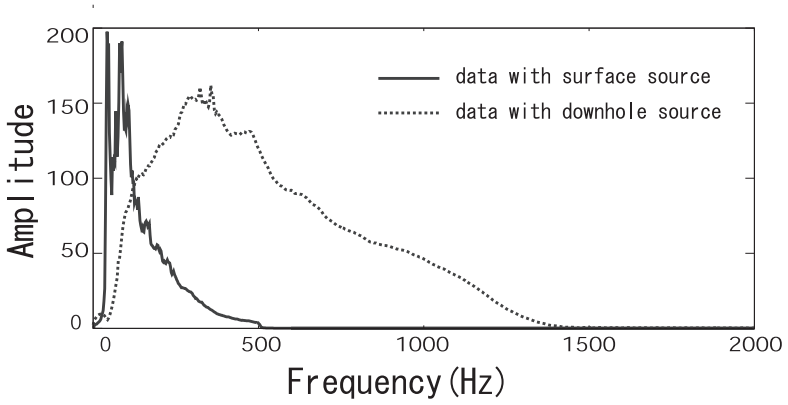

Figure. 6.13: Average frequency spectra from input data for seismic interferometry using explosive surface sources (solid line) and crosswell data using downhole sources (dashed line).

7 Conclusions

7.1 Summary of study

In this thesis it is shown that the Seismic Interferometry (SI) retrieves Green's function based on the reciprocity theorem. We showed that the SI has a potential to be applied to a wide range of the field data in order to monitor the dynamic change of the properties or to reduce the survey cost.

We applied SI to Ocean Bottom Seismogram (OBS) records observing local earthquakes. We used the stationary-phase interpretation to obtain the high-quality reflection imaging results under the localized source distribution. We estimated the raypath of two reflection events which are sea-surface P-wave reflection and sea-surface multiple P-wave reflection. We show that choosing CC traces by stationary-phase evaluation improves the quality of the reflection from the upper oceanic crust boundary. This processing can be used to obtain higher-resolution reflection images under the insufficient source illumination.

We applied SI to ambient noise records. We estimated the velocity change during six months at South Tohoku region in the duration of the 2011 off the Pacific coast of Tohoku Earthquake in Japan using scattered wave from autocorrelation analysis. The estimated velocity drop was around 2% in Fukushima prefecture. The spatial distribution of velocity change shows the correlation for both static strain change derived from GPS and the peak particle velocity during earthquake. Therefore, the velocity change may be associated with (1) the enormous stress change due to the earthquake and (2) near-surface damaging due to the strong motion of seismic wave.

In order to enhance the quality of the retrieval of the wavefield, we implemented singular-value decomposition for Multidimensional deconvolution (MDD) interferometry. We investigated the source illumination for SI by MDD using the quantities derived from SVD representing the characteristics of the inverse problems. We found that the MDD is ill-posed problem and showed that the rank of the Incident field matrix (IFM) which is the kernel matrix of MDD, reflects the amount of the source illumination. This observation is crucial when we design the seismic experiments for MDD-based approach.

We applied SI by CC and MDD to the borehole data. We retrieved a crosswell wavefield from a conventional VSP data, which has a potential to remove the effect of near-surface, to expand survey area using higher-energy sources and to reduce the survey cost significantly. The retrieved images agree well with migrated data from a conventional crosswell seismic reflection survey and with P-wave velocities from well logs. The comparison of the retrieved reflected wavefields from the two methods with the reflected wavefields observed using borehole vibrators shows that

both the MDD and CC methods retrieve up-going reflections very well, and the MDD method retrieves down-going reflections with better amplitude preservation than the CC method.

7.2 Future prospects

A principle of Seismic Interferometry has already been used for many studies. Now, SI is at the stage of practical use. One of the important feature of SI is to reduce the survey cost. It is suitable for a survey in the urban area or disaster area where it is difficult to install a controlled source. Furthermore, the SI is expected to be developed into the application of monitoring technique. For example, it was shown that the crosswell reflection imaging can be achieved without borehole sources. This shows a feasibility of monitoring of e.g. carbon sequestration using high-resolution wavefield by installing permanent receivers into the downhole. On the other hand, it has been pointed out that the conventional CC method has a limitation when the assumption of a homogeneous source distribution is violated. Since the MDD method has a potential to overcome this problem, future applications are expected. In the stage of experimental design, an appropriate source-receiver configuration must be required. Furthermore, evaluation for a reliability of retrieved wavefield also must be required. A stationary-phase approximation for the CC method and the quantities derived from SVD for the MDD method is expected to contribute to those purposes.

AppendixA

A.1 Source-reciever reciprocity

We derive the source-receiver reciprocity. We start from convolution-type reciprocity.

$$\oint_{\mathbb{S}} \{\hat{p}_A \hat{v}_{i,B} - \hat{v}_{i,A} \hat{p}_B\} n_i d^2\mathbf{x} = \int_{\mathbb{D}} \{\hat{p}_A \hat{q}_B - \hat{q}_A \hat{p}_B\} d^3\mathbf{x}. \tag{A.1}$$

We introduce two impulse source at $\mathbf{x}_A$ and $\mathbf{x}_B$ inside the volume $\mathbb{V}$. We define the medium parameter for state A and B is identical. Then we obtain following wavefields,

$$\hat{p}_A(\mathbf{x}, \omega) = \hat{G}(\mathbf{x}, \mathbf{x}_A, \omega), \tag{A.2}$$

$$\hat{v}_{i,A}(\mathbf{x}, \omega) = -\frac{1}{j\omega\rho_A(\mathbf{x})} \partial_i \hat{G}(\mathbf{x}, \mathbf{x}_A, \omega), \tag{A.3}$$

$$\hat{p}_B(\mathbf{x}, \omega) = \hat{G}(\mathbf{x}, \mathbf{x}_B, \omega), \tag{A.4}$$

$$\hat{v}_{i,B}(\mathbf{x}, \omega) = -\frac{1}{j\omega\rho_B(\mathbf{x})} \partial_i \hat{G}(\mathbf{x}, \mathbf{x}_B, \omega), \tag{A.5}$$

where $\hat{G}(\mathbf{x}, \mathbf{x}_{A(B)}, \omega)$ indicates the Green's function observed at $\mathbf{x}$ from the source at $\mathbf{x}_{A(B)}$. Substituting these equations into A.1 yields,

$$\begin{aligned} \hat{G}(\mathbf{x}_B, \mathbf{x}_A, \omega) - \hat{G}(\mathbf{x}_A, \mathbf{x}_B, \omega) &= \oint_{\mathbb{S}} \frac{-1}{j\omega\rho_A(\mathbf{x})} \Big[\hat{G}(\mathbf{x}, \mathbf{x}_A, \omega) \partial_i \hat{G}(\mathbf{x}, \mathbf{x}_B, \omega) \\ &\qquad - \hat{G}(\mathbf{x}, \mathbf{x}_B, \omega) \partial_i \hat{G}(\mathbf{x}, \mathbf{x}_A, \omega) \Big]. \end{aligned} \tag{A.6}$$

The right-hand side of equation A.6 vanishes when the radius of the integral surface $\mathbb{S}$ is choosen as infinite. Since $\mathbb{S}$ is arbitral as long as the points $\mathbf{x}_A$ and $\mathbf{x}_B$ are inside of $\mathbb{V}$, the right-hand side of equatoin A.6 can be always zero. Therefore, we obtain source-receiver reciprocity as,

$$\hat{G}(\mathbf{x}_B, \mathbf{x}_A, \omega) = \hat{G}(\mathbf{x}_A, \mathbf{x}_B, \omega). \tag{A.7}$$

Note that the source-receiver reciprocity holds in the dissipative media since the lossless assumption is not introduced in the convolution-type reciprocity.

A.2 Derivation of the MDD relationship for crosswell geometry

We derive the MDD convolution relationship for crosswell geometry (equation 6.7) from one-way wavefield reciprocity. Our derivation of equation 6.7 is almost identical to that of Wapenaar et al. (2008a) except that we consider the transmission response instead of the reflection response.

In an arbitrarily heterogeneous 3D acoustic medium, one-way wavefield reciprocity is written as

$$\int_{\partial\mathbb{D}_2} \{\hat{p}_A^+ \hat{p}_B^- - \hat{p}_A^- \hat{p}_B^+\} d^2\mathbf{x} = \int_{\partial\mathbb{D}_1} \{\hat{p}_A^+ \hat{p}_B^- - \hat{p}_A^- \hat{p}_B^+\} d^2\mathbf{x}, \tag{A.8}$$

where $\mathbf{x} = (x_1, x_2, x_3)$ is a position vector in Cartesian coordinates, $\hat{p}$ denotes acoustic wavefield in the space-frequency domain, and the superscripts + and − denote the down-going and up-going acoustic waves, respectively. $\partial\mathbb{D}_1$ and $\partial\mathbb{D}_2$ denote horizontal boundaries of infinite extent above and below the domain $\mathbb{D}$ (Figure A.1). The subscripts A and B denote two states that have identical medium parameters inside the 3D domain $\mathbb{D}$ (this is the domain enclosed by the boundaries $\partial\mathbb{D}_1$ and $\partial\mathbb{D}_2$). Equation A.8 shows the relationship between the surface integrals of the convolution products of the decomposed wavefields for the two states A and B. As we are interested in a crosswell geometry, we can rotate the geometry from Figure A.1 90° clockwise (Figure A.2). Here, note that we redefine the x_3-axis as the vertical coordinate in Figure A.2. Consequently, equation A.8 can be rewritten as

$$\int_{\partial\mathbb{D}_2} \{\hat{p}_A^L \hat{p}_B^R - \hat{p}_A^R \hat{p}_B^L\} d^2\mathbf{x} = \int_{\partial\mathbb{D}_1} \{\hat{p}_A^L \hat{p}_B^R - \hat{p}_A^R \hat{p}_B^L\} d^2\mathbf{x}, \tag{A.9}$$

where the superscripts L and R denote the left-propagating and right-propagating waves, respectively. The boundaries $\partial\mathbb{D}_1$ and $\partial\mathbb{D}_2$ are then vertical boundaries of infinite extent. In the following derivation, these two boundaries correspond to the borehole positions.

Let us consider two independent states A and B of the domain $\mathbb{D}$ that have identical medium parameters in $\mathbb{D}$. State A represents the desired crosswell wavefields (Figure A.2(a)). For this state, we assume homogeneity for the space outside domain $\mathbb{D}$. A point source is placed at $\mathbf{x}_A$, which is immediately left of $\partial\mathbb{D}_1$. To evaluate equation A.9, we need the acoustic wavefields along $\partial\mathbb{D}_2$ and $\partial\mathbb{D}_1$. The wavefields observed at $\partial\mathbb{D}_2$ are right-propagating because of the homogeneity of the right half-space. Therefore, the wavefields along $\partial\mathbb{D}_2$ can be written to be

$$\mathbf{x} \in \partial\mathbb{D}_2, \begin{cases} \hat{p}_A^L = 0 \\ \hat{p}_A^R = \hat{G}^R(\mathbf{x}, \mathbf{x}_A, \omega)\hat{S}_A(\omega) \end{cases}, \tag{A.10}$$

where $\hat{G}^R$ denotes the transmission response (or Green's function) from $\mathbf{x}_A$ to $\mathbf{x}$, and $\hat{S}_A$ denotes the source spectrum of the point source at $\mathbf{x}_A$. On the other hand, the wavefields along $\partial\mathbb{D}_1$ are both right-propagating, caused by the point source, and left-propagating, caused by scattering inside $\mathbb{D}$. These wavefields are written

$$\mathbf{x} \in \partial\mathbb{D}_1, \begin{cases} \hat{p}_A^L = \hat{G}^L(\mathbf{x}, \mathbf{x}_A, \omega)\hat{S}_A(\omega) \\ \hat{p}_A^R = \delta(\mathbf{x}_\mathbf{V} - \mathbf{x}_{\mathbf{V},A})\hat{S}_A(\omega) \end{cases}, \tag{A.11}$$

where the subscript **V** denotes the vertical coordinate; hence, $\mathbf{x_V} = (x_2, x_3)$ and $\mathbf{x_{V,A}} = (x_{2,A}, x_{3,A})$. The latter denotes the vertical coordinate of $\mathbf{x}_A$.

For state B, we consider an actual measurement condition. The right half-space from $\partial\mathbb{D}_2$ can be arbitrarily inhomogeneous (Figure A.2(b)). A point source (a physical source) is placed at $\mathbf{x}_S$, which is to the right of $\partial\mathbb{D}_2$. The receiver arrays that are placed at $\partial\mathbb{D}_2$ and $\partial\mathbb{D}_1$ observe wavefields from this point source. In a way similar to that for state A, the wavefields observed at $\partial\mathbb{D}_2$ can be represented as

$$\mathbf{x} \in \partial\mathbb{D}_2, \begin{cases} \hat{p}_B^L = \hat{p}^L(\mathbf{x}, \mathbf{x}_S, \omega) \\ \hat{p}_B^R = \hat{p}^R(\mathbf{x}, \mathbf{x}_S, \omega) \end{cases} . \tag{A.12}$$

Accordingly, the wavefields at $\partial\mathbb{D}_1$ are represented as

$$\mathbf{x} \in \partial\mathbb{D}_1, \begin{cases} \hat{p}_B^L = \hat{p}^L(\mathbf{x}, \mathbf{x}_S, \omega) \\ \hat{p}_B^R = 0 \end{cases} , \tag{A.13}$$

where $\hat{p}_B^R = 0$ because we assume that the half-space left of $\partial\mathbb{D}_1$ is homogeneous. This condition seems to be unpractical for crosswell surveys in the field, but in reality it can be relaxed to a layered (horizontal or inclined) half-space, in which there are no reflected waves that propagate back to $\partial\mathbb{D}_1$ from the half-space left of $\partial\mathbb{D}_1$.

Substituting equations A.10 to A.13 into equation A.9 yields the convolution relationship

$$\hat{p}^L(\mathbf{x}_A, \mathbf{x}_S, \omega) = \int_{\partial\mathbb{D}_2} \hat{G}^L(\mathbf{x}_A, \mathbf{x}, \omega)\hat{p}^L(\mathbf{x}, \mathbf{x}_S, \omega)d^2\mathbf{x}, \tag{A.14}$$

where we applied source-receiver reciprocity ($\hat{G}^R(\mathbf{x}, \mathbf{x}_A, \omega) = \hat{G}^L(\mathbf{x}_A, \mathbf{x}, \omega)$). Note that this one-way source-receiver reciprocity relation is valid only if one used flux-normalized decomposition of the two-way wavefields into one-way wavefields (Wapenaar, 1998). Equation A.14 shows the relationship between the crosswell wavefield $\hat{G}^L(\mathbf{x}_A, \mathbf{x}, \omega)$ and the actual measurements of the responses at the borehole receiver arrays from the surface source at $\mathbf{x}_S$. This equation can be solved when the left-going waves $\hat{p}^L(\mathbf{x}_A, \mathbf{x}_S, \omega)$ and $\hat{p}^L(\mathbf{x}, \mathbf{x}_S, \omega)$ are available for a sufficient range of the source position $\mathbf{x}_S$. The integration of equation A.14 should be taken for the 2D surface of $\partial\mathbb{D}_2$. However, our borehole is 1D along the x_3-direction. Therefore in practice the integration is taken only along the vertical direction of $\partial\mathbb{D}_2$ with fixed borehole position x_2.

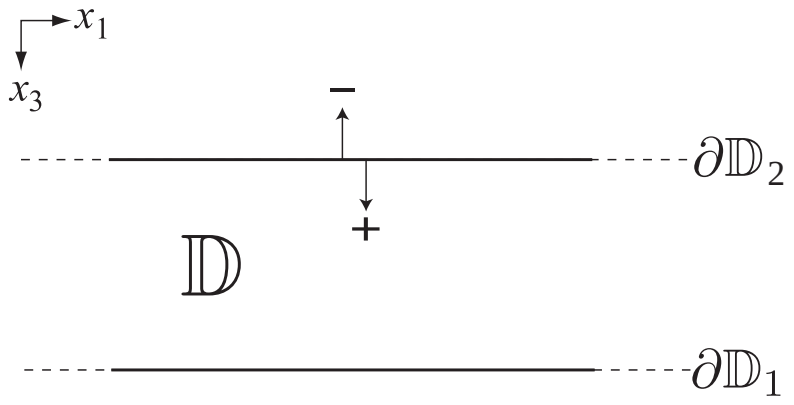

Figure. A.1: Domain $\mathbb{D}$ between horizontal boundaries $\partial\mathbb{D}_2$ and $\partial\mathbb{D}_1$.

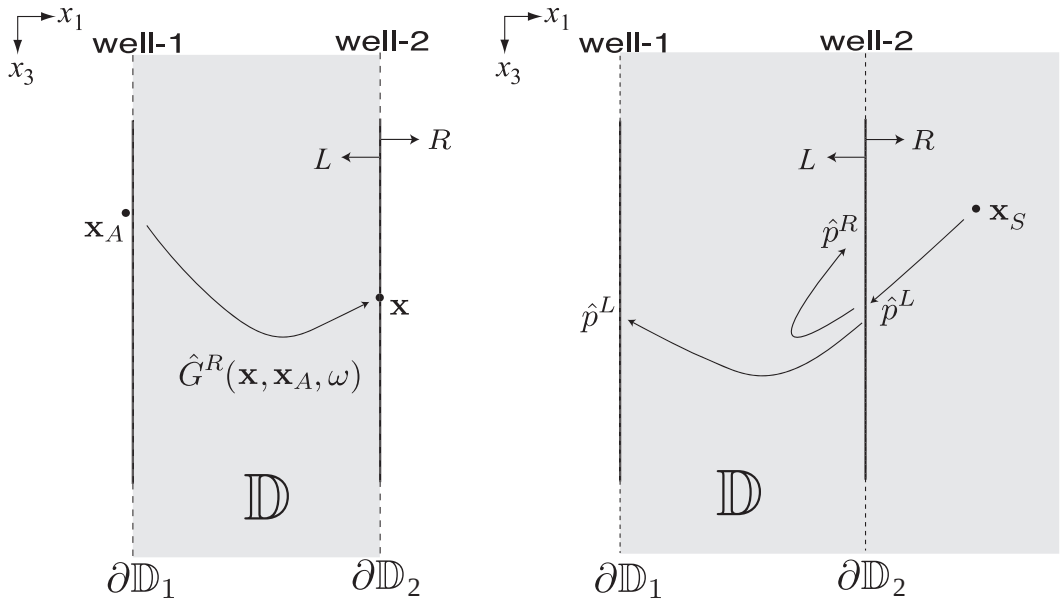

Figure. A.2: (a) Desired crosswell wavefield for state A. $\mathbb{D}$ is a volume enclosed by the two boreholes (vertical boundaries $\partial\mathbb{D}_1$ and $\partial\mathbb{D}_2$) of infinite extent. $\hat{G}^R(\mathbf{x}, \mathbf{x}_A, \omega)$ denotes the transmission response (or Green's function) from $\mathbf{x}_A$ to $\mathbf{x}$. (b) Actual wavefield for state B. $\hat{p}^L$ and $\hat{p}^R$ represent left- and right-propagating wavefields from the source at $\mathbf{x}_S$. The areas shaded in gray represent heterogeneous space.

References

Bakulin, A., and R. Calvert, 2006, The virtual source method: Theory and case study: Geophysics, **71**, SI139–SI150.

Bensen, G. D., M. H. Ritzwoller, M. P. Barmin, A. L. Levshin, F. Lin, M. P. Moschetti, N. M. Shapiro, and Y. Yang, 2007, Processing seismic ambient noise data to obtain reliable broad-band surface wave dispersion measurements: Geophysical Journal International, **169**, 1239–1260.

Beresnev, I., and K. Wen, 1996, Nonlinear soil response-a reality?: Bulletin of the Seismological Society of America, **86**, 1964–1978.

Berkhout, A., 1982, Seismic migration-Imaging of acoustic energy by wave field extrapolation: Elsevier.

Brenguier, F., M. Campillo, C. Hadziioannou, N. M. Shapiro, R. M. Nadeau, and E. Larose, 2008, Postseismic relaxation along the san andreas fault at parkfield from continuous seismological observations: Science, **321**, 1478–1481.

Christensen, N. I., and H. F. Wang, 1985, The influence of pore pressure and confining pressure on dynamic elastic properties of berea sandstone: Geophysics, **50**, 207–213.

Claerbout, J. F., 1968, Synthesis of a layered medium from its acoustic transmission response: Geophysics, **33**, 264–269.

Curtis, A., P. Gerstoft, H. Sato, R. Snieder, and K. Wapenaar, 2006, Seismic interferometry—turning noise into signal: The Leading Edge, **25**, 1082–1092.

Derode, A., E. Larose, M. Campillo, and M. Fink, 2003, How to estimate the green's function of a heterogeneous medium between two passive sensors? application to acoustic waves: Applied Physics Letters, **83**, 3054–3056.

Dong, S., R. He, and G. T. Schuster, 2006, Interferometric predcition and least squares subtraction of surface waves: SEG Technical Program Expanded Abstracts, **25**, 2783–2786.

Draganov, D., X. Campman, J. Thorbecke, A. Verdel, and K. Wapenaar, 2009, Reflection images from ambient seismic noise: Geophysics, **74**, A63–A67.

Fréchet, J., L. Martel, L. Nikolla, and G. Poupinet, 1989, Application of the cross-spectral moving-window technique (csmwt) to the seismic monitoring of forced fluid migration in a rock mass: International Journal of Rock Mechanics and Mining Sciences and Geomechanics Abstracts, **26**, 221 – 233.

Freire, S., and T. Ulrych, 1988, Application of singular value decomposition to vertical seismic profiling: Geophysics, **53**, 778–785.

Golub, G. H., and C. F. van Loan, 1983, Matrix computations: The Johns Hopkins University Press.

Hadziioannou, C., E. Larose, O. Coutant, P. Roux, and M. Campillo, 2009, Stability of monitoring weak changes in multiply scattering media with ambient noise correlation: Laboratory experiments: The Journal of the Acoustical Society of America, **125**, 3688–3695.

Halliday, D., and A. Curtis, 2009, Seismic interferometry of scattered surface waves in attenuative media: Geophysical Journal International, **178**, 419–446.

Halliday, D. F., A. Curtis, J. O. A. Robertsson, and D.-J. van Manen, 2007, Interferometric surface-wave isolation and removal: Geophysics, **72**, A69–A73.

Halliday, D. F., A. Curtis, P. Vermeer, C. Strobbia, A. Glushchenko, D.-J. van Manen, and J. O. A. Robertsson, 2010, Interferometric ground-roll removal: Attenuation of scattered surface waves in single-sensor data: Geophysics, **75**, SA15–SA25.

Harris, J., R. Nolen-Hoeksema, R. Langan, M. Van Schaack, S. Lazaratos, and J. Rector III, 1995, High-resolution crosswell imaging of a west Texas carbonate reservoir: Part 1-Project summary and interpretation: Geophysics, **60**, 667–681.

Hornby, B. E., and J. Yu, 2007, Interferometric imaging of a salt flank using walkaway vsp data: The Leading Edge, **26**, 760–763.

Jiang, Z., 2006, Migration of interbed multiple reflections: SEG Technical Program Expanded Abstracts, **25**, 3501–3505.

Johnson, P., and A. Sutin, 2005, Slow dynamics and anomalous nonlinear fast dynamics in diverse solids: The Journal of the Acoustical Society of America, **117**, 124–130.

Klema, V., and A. Laub, 1980, The singular value decomposition: Its computation and some applications: IEEE Transactions on Automatic Control, **25**, 164–176.

Larose, E., L. Margerin, A. Derode, B. van Tiggelen, M. Campillo, N. Shapiro, A. Paul, L. Stehly, and M. Tanter, 2006, Correlation of random wavefields: An interdisciplinary review: Geophysics, **71**, SI11–SI21.

Lazaratos, S. K., J. W. Rector, J. M. Harris, and M. V. Schaack, 1993, High-resolution, crosswell reflection imaging: Potential and technical difficulties: Geophysics, **58**, 1270–1280.

Lyakhovsky, V., Y. Ben-Zion, and A. Agnon, 1997, Distributed damage, faulting, and friction: JOURNAL OF GEOPHYSICAL RESEARCH-ALL SERIES-, **102**, 27–27.

Mehta, K., A. Bakulin, D. Kiyashchenko, and J. Lopez, 2008a, Comparing virtual versus real crosswell surveys: SEG Technical Program Expanded Abstracts, **27**, 1372–1376.

Mehta, K., A. Bakulin, J. Sheiman, R. Calvert, and R. Snieder, 2007, Improving the virtual source method by wavefield separation: Geophysics, **72**, V79.

Mehta, K., D. Kiyashchenko, P. Jorgensen, J. Lopez, J. Ferrandis, and M. Costello, 2010, Virtual source method applied to crosswell and horizontal well geometries: The Leading Edge, **29**, 712–723.

Mehta, K., R. Snieder, R. Calvert, and J. Sheiman, 2008b, Acquisition geometry requirements for generating virtual-source data: The Leading Edge, **27**, 620–629.

Meier, U., N. Shapiro, and F. Brenguier, 2010, Detecting seasonal variations in seismic velocities within los angeles basin from correlations of ambient seismic noise: Geophys. J. Int, **181**, 985–996.

Menke, W., 1989, Geophysical data analysis: discrete inverse theory: Academic Press.

Minato, S., T. Matsuoka, T. Tsuji, D. Draganov, J. Hunziker, and K. Wapenaar, 2011, Seismic interferometry using multidimensional deconvolution and crosscorrelation for crosswell seismic reflection data without borehole sources: Geophysics, **76**, SA19–SA34.

Minato, S., K. Onishi, T. Matsuoka, Y. Okajima, J. Tsuchiyama, D. Nobuoka, H. Azuma, and T. Iwamoto, 2007, Crosswell seismic survey without borehole source: SEG Technical Program Expanded Abstracts, **26**, 1357–1361.

Moore, G., J. Park, N. Bangs, S. Gulick, H. Tobin, Y. Nakamura, S. Sato, T. Tsuji, T. Yoro, H. Tanaka, S. Uraki, Y. Kido, Y. Sanada, S. Kuramoto, and A. Taira, 2009, Structural and seismic stratigraphic framework of the nantroseize stage 1 transect: IODP.

Morozov, V., Z. Nashed, and A. Aries, 1984, Methods for solving incorrectly posed problems: Springer New York.

Nakanishi, A., N. Takahashi, J. Park, S. Miura, S. Kodaira, Y. Kaneda, N. Hirata, T. Iwasaki, and M. Nakamura, 2002, Crustal structure across the coseismic rupture zone of the 1944 Tonankai earthquake, the central Nankai Trough seismogenic zone: Journal of Geophysical Research-Solid Earth, **107**, 2007.

Nakata, N., and R. Snieder, 2011, Near-surface weakening in japan after the 2011 tohoku-oki earthquake: Geophys. Res. Lett., **38**, L17302.

Nishimura, T., N. Uchida, H. Sato, M. Ohtake, S. Tanaka, and H. Hamaguchi, 2000, Temporal changes of the crustal structure associated with the m6. 1 earthquake on september 3, 1998, and the volcanic activity of mount iwate, japan: Geophys. Res. Lett, **27**, 269–272.

Niu, F., P. Silver, T. Daley, X. Cheng, and E. Majer, 2008, Preseismic velocity changes observed from active source monitoring at the parkfield safod drill site: Nature, **454**, 204–208.

Obana, K., S. Kodaira, and Y. Kaneda, 2004, Microseismicity around rupture area of the 1944 Tonankai earthquake from ocean bottom seismograph observations: Earth and Planetary Science Letters, **222**, 561–572.

———, 2005, Seismicity in the incoming/subducting Philippine Sea plate off the Kii Peninsula, central Nankai trough: Journal of Geophysical Research, **110**, B11311.

Ogura, K., T. Ohhashi, M. Osada, and M. Yoshimura, 1992, Design of a multidisk type downhole seismic source: SEG Technical Program Expanded Abstracts, **11**, 702–705.

Ohmi, S., K. Hirahara, H. Wada, and K. Ito, 2008, Temporal variations of crustal structure in the source region of the 2007 noto hanto earthquake, central japan, with passive image interferometry: Earth, Planets and Space, **60**, 1069–1074.

Oristaglio, M. L., 1985, A guide to current uses of vertical seismic profiles: Geophysics, **50**, 2473–2479.

Ozawa, S., T. Nishimura, T. Suito, H.a nd Kobayashi, M. Tobita, and T. Imakiire, 2011, Coseismic and postseismic slip of the 2011 magnitude-9 tohoku-oki earthquake: Nature, **475**, 373–377.

Park, J.-O., G. F. Moore, T. Tsuru, S. Kodaira, and Y. Kaneda, 2004, A subducted oceanic ridge influencing the nankai megathrust earthquake rupture: Earth and Planetary Science Letters, **217**, 77 – 84.

Peng, Z., and Y. Ben-Zion, 2006, Temporal changes of shallow seismic velocity around the

karadere-düzce branch of the north anatolian fault and strong ground motion: Pure and Applied Geophysics, **163**, no. 2, 567–600.

Poupinet, G., W. Ellsworth, and J. Frechet, 1984, Monitoring velocity variations in the crust using earthquake doublets: an application to the calaveras fault, california: Journal of Geophysical Research, **89**, 5719–5731.

Roux, P., K. G. Sabra, W. A. Kuperman, and A. Roux, 2005, Ambient noise cross correlation in free space: Theoretical approach: The Journal of the Acoustical Society of America, **117**, 79–84.

Rubinstein, J., and G. Beroza, 2004, Nonlinear strong ground motion in the ml 5.4 chittenden earthquake: Evidence that preexisting damage increases susceptibility to further damage: Geophys. Res. Lett, **31**.

Schaff, D., and G. Beroza, 2004, Coseismic and postseismic velocity changes measured by repeating earthquakes: Journal of geophysical research, **109**, B10302.

Schuster, G., 2001, Theory of daylight/interferometric imaging: tutorial: EAGE Conference and Technical Exhibition, **63**, A032.

———, 2009, Seismic interferometry: Cambridge Univ Pr.

Schuster, G., J. Yu, J. Sheng, and J. Rickett, 2004, Interferometric/daylight seismic imaging: Geophysical Journal International, **157**, 838–852.

Sens-Schönfelder, C., and U. Wegler, 2006, Passive image interferometry and seasonal variations of seismic velocities at merapi volcano, indonesia: Geophys. Res. Lett, **33**, 1–5.

Shapiro, N. M., M. Campillo, L. Stehly, and M. H. Ritzwoller, 2005, High-Resolution Surface-Wave Tomography from Ambient Seismic Noise: Science, **307**, 1615–1618.

Shiraishi, K., 2007, Study on simulation of elastic waves by method of characteristics, and subsurface exploration by seismic interferometry: PhD thesis, Kyoto University.

Shiraishi, K., and T. Matsuoka, 2005, Application of seismic interferometry to cross-well seismic reflection: Proceedings of the 114th Conference, SEGJ, 65–68.

Shiraishi, K., T. Matsuoka, T. Matsuoka, M. Tanoue, and S. Yamagushi, 2008, Application of seismic interferometry to inverse vsp data: BUTSURI-TANSA, **61**, 111–120.

Slob, E., D. Draganov, and K. Wapenaar, 2007, Interferometric electromagnetic Green's functions representations using propagation invariants: Geophysical Journal International, **169**, 60–80.

Snieder, R., 2004, Extracting the Green's function from the correlation of coda waves: A derivation based on stationary phase: Physical Review E, **69**, 46610.

Snieder, R., A. Grêt, H. Douma, and J. Scales, 2002, Coda wave interferometry for estimating nonlinear behavior in seismic velocity: Science, **295**, 2253–2255.

Snieder, R., K. Wapenaar, and K. Larner, 2006, Spurious multiples in seismic interferometry of primaries: Geophysics, **71**, SI111–SI124.

Takahashi, H., 2011, Static strain and stress changes in eastern japan due to the 2011 off the pacific coast of tohoku earthquake, as derived from gps data: Earth Planets Space, **63**, 741–744.

Takahashi, T., T. Imayoshi, H. Ishikawa, and T. Takeda, 2001, Borehole seismic characterization

of a heterogeneous rock: International Journal of Rock Mechanics and Mining Sciences, **38**, 851–857.

Tamagawa, T., T. Matsuoka, and A. Sakai, 1997, Multiple reflections and ghost for tilted sea bottom: BUTSURI-TANSA, **50**, 477–485.

TenCate, J. A., E. Smith, and R. A. Guyer, 2000, Universal slow dynamics in granular solids: Phys. Rev. Lett., **85**, no. 5, 1020–1023.

Terada, A., and N. Miyabe, 1929, Deformation of the earth crust in kwansai district and its relation to orographic features: Bull. Earthq. Res. Inst., **7**, 233–239.

Toksöz, M. N., C. H. Cheng, and A. Timur, 1976, Velocities of seismic waves in porous rocks: Geophysics, **41**, 621–645.

Tonegawa, T., K. Nishida, T. Watanabe, and K. Shiomi, 2009, Seismic interferometry of teleseicmic S-wave coda for retrieval of body waves: an application to the Philippine Sea slab underneath the Japanese Islands: Geophysical Journal International, **178**, 1574–1586.

Torii, K., K. Shiraishi, K. Onishi, T. Kimura, S. Ito, T. Aizawa, K. Tsukada, and T. Matsuoka, 2006, Cross-Hole Tomography Using Seismic Interferometry: EAGE Conference and Technical Exhibition, **68**, A044.

Tsuji, T., H. Tokuyama, P. Pisani, and G. Moore, 2008, Effective stress and pore pressure in the nankai accretionary prism off the muroto peninsula, southwestern japan: J. geophys. Res, **113**.

Ursin, B., and Y. Zheng, 1985, Identification of seismic reflections using singular value decomposition: Geophysical Prospecting, **33**, 773–799.

van der Neut, J., K. Mehta, J. Thorbecke, and K. Wapenaar, 2010, Controlled-source elastic interferometric imaging by multi-dimensional deconvolution with downhole receivers below a complex overburden: SEG Technical Program Expanded Abstracts, **29**, 3979–3985.

Vasconcelos, I., and R. Snieder, 2008a, Interferometry by deconvolution, part 1— theory for acoustic waves and numerical examples: Geophysics, **73**, S115–S128.

———, 2008b, Interferometry by deconvolution: Part 2 — theory for elastic waves and application to drill-bit seismic imaging: Geophysics, **73**, S129–S141.

Vidale, J., and Y. Li, 2003, Damage to the shallow landers fault from the nearby hector mine earthquake: Nature, **421**, 524–526.

Virieux, J., 1986, P-sv wave propagation in heterogeneous media: Velocity-stress finite-difference method: Geophysics, **51**, 889–901.

Wapenaar, K., 1998, Reciprocity properties of one-way propagators: Geophysics, **63**, 1795–1798.

———, 2004, Retrieving the elastodynamic green's function of an arbitrary inhomogeneous medium by cross correlation: Phys. Rev. Lett., **93**, 254301.

Wapenaar, K., D. Draganov, J. Thorbecke, and J. Fokkema, 2002, Theory of acoustic daylight imaging revisited: SEG Technical Program Expanded Abstracts, **21**, 2269–2272.

Wapenaar, K., and J. Fokkema, 2006, Green's function representations for seismic interferometry: Geophysics, **71**, SI33–SI46.

Wapenaar, K., E. Ruigrok, J. van der Neut, and D. Draganov, 2010, Improved surface-wave

retrieval from ambient seismic noise by multi-dimensional deconvolution: Geophys. Res. Lett., **38**.

Wapenaar, K., E. Slob, and R. Snieder, 2008a, Seismic and electromagnetic controlled-source interferometry in dissipative media: Geophysical Prospecting, **56**, 419–434.

Wapenaar, K., and J. van der Neut, 2010, A representation for green's function retrieval by multidimensional deconvolution: The Journal of the Acoustical Society of America, **128**, EL366–EL371.

Wapenaar, K., J. van der Neut, and E. Ruigrok, 2008b, Passive seismic interferometry by multi-dimensional deconvolution: Geophysics, **73**, A51–A56.

Wapenaar, K., J. van der Neut, E. Ruigrok, D. Draganov, J. Hunziker, E. Slob, J. Thorbecke, and R. Snieder, 2011, Seismic interferometry by crosscorrelation and by multidimensional deconvolution: a systematic comparison: Geophysical Journal International, no–no.

Wegler, U., and C. Sens-Schönfelder, 2007, Fault zone monitoring with passive image interferometry: Geophysical Journal International, **168**, 1029–1033.

Willis, M. E., R. Lu, X. Campman, M. N. Toksöz, Y. Zhang, and M. V. de Hoop, 2006, A novel application of time-reversed acoustics: Salt-dome flank imaging using walkaway vsp surveys: Geophysics, **71**, A7–A11.

Xiao, X., M. Zhou, and G. T. Schuster, 2006, Salt-flank delineation by interferometric imaging of transmitted P- to S-waves: Geophysics, **71**, SI197–SI207.

Yu, J., and G. T. Schuster, 2006, Crosscorrelogram migration of inverse vertical seismic profile data: Geophysics, **71**, S1–S11.

Acknowledgement

I would like to express my gratitude to all persons who helped me to complete this thesis. I want to sincerely thank to Prof. Toshifumi Matsuoka, Prof. Junji Kiyono and Prof. Hitoshi Mikada for reviewing this thesis and for providing me the invaluable comments and suggestions.

I owe particularly thanks to Prof. Toshifumi Matsuoka and Dr. Takeshi Tsuji for their daily help and warm encouragement for many years.

I would like to thank to Dr. Yasuhiro Yamada, Dr. Shiro Ohmi of Disaster Prevention Research Institute and Dr. Koichiro Obana of Japan Agency for Marine-Earth Science and Technology (JAMSTEC) for their support, constructive comments and suggestions.

I owe Chapter 6 to Prof. Kees Wapenaar, Dr. Deyan Draganov and Jürg Hunziker of Delft University of Technology. I would like to thank them for helping me to understand multidimensional deconvolution and discussion about synthetic data.

I would like to express my gratitude to JAMSTEC for providing OBS data, National Research Institute for Earth Science and Disaster Prevention (NIED) for providing Hi-net and Kik-net data. I also thank to Recyclable-Fuel Storage Company and OYO Corporation for providing VSP data and crosswell data.

I gratefully appreciate the financial support of Japan Society for the Promotion of Science (JSPS) Fellowship that made it possible to complete this thesis.

I wish to express my gratitude to all of my colleagues and friends in Kyoto for their support, discussions, warm friendship and encouragements, which made my stay in Kyoto truly fruitful and unforgetable.

Finally, I would like to thank to my father and mother for their moral support and warm encouragements.

謝辞

本学位論文をまとめるにあたり査読をして頂いた，京都大学大学院工学研究科　松岡俊文教授，清野純史教授，三ヶ田均教授に感謝します．

本研究を遂行するにあたり，長きに渡って指導して頂いた工学研究科　松岡俊文教授，辻健助教に心より感謝します．また工学研究科　山田泰広准教授，理学研究科　大見士朗准教授，(独) 海洋研究開発機構　尾鼻浩一郎氏には，これまでの研究において多くのご指導，ご助言，ご協力を頂きました．

Chapter 6 では，デルフト工科大学の Kees Wapenaar 教授，Deyan Draganov 氏，Jürg Hunziker 氏にモデリングや多次元デコンボリューションに関する様々な助言を頂きました．ここに記して感謝します．

研究に際し，OBS データを提供して下さった (独) 海洋研究開発機構，Hi-net および Kik-net データを提供して下さった (独) 防災科学技術研究所，VSP データおよび坑井間弾性波データを提供して下さったリサイクル燃料貯蔵株式会社，応用地質株式会社に深く感謝します．

研究活動費においては，(独) 日本学術振興会特別研究員科研費のご支援を頂きました．ここに記して感謝します．

これまで研究室内外で苦楽を共にし，有意義な議論で刺激しあってきた地質工学研究室 (現・環境資源システム工学研究室) とジオフィジクス研究室 (現・応用地球物理学研究室) の先輩・後輩・仲間たちに感謝します．また，学生生活で出会った全ての友人たちに感謝します．

最後に，博士課程に進学する機会を与えてくれ，私を常に温かく見守り，支え続けてくれた両親に最大の謝意を表します．

Ph.D. Thesis

Applications and Development of Seismic Interferometry by Crosscorrelation and Multidimensional Deconvolution

Shohei Minato

Laboratory of Engineering Geology,
Department of Civil and Earth Resources Engineering,
Kyoto University

Kyoto University, Room C1-1-118
Kyotodaigaku-Katsura, Nishikyo-ku, Kyoto, 615-8540, Japan

s_minato@earth.kumst.kyoto-u.ac.jp

Version: February 21, 2012